

Impact of pinhole collimation on SPECT image quality metrics, and methods for patient-specific assessment of noise and standardization of imaging protocols

by

Sarah G. Cuddy-Walsh

A thesis submitted to the Faculty of Graduate and Postdoctoral Affairs in partial fulfillment of the requirements for the degree of

Doctor of Philosophy

in

Physics

Ottawa-Carleton Institute for Physics  
Department of Physics  
Carleton University  
Ottawa, Ontario

© 2018, Sarah G. Cuddy-Walsh

## **Abstract**

Dedicated cardiac pinhole SPECT camera designs offer improvements in overall sensitivity, thereby enabling the use of lower injected radiotracer activity and shorter imaging times than parallel-hole designs. The effect of these novel camera designs on image noise on a voxel-by-voxel level has not previously been investigated. This work identifies position and orientation-dependent variability of spatial resolution in the field-of-view (FOV) of pinhole cameras. It also identifies a 1.7-fold gradient in the magnitude of image noise across the length of the heart which leads to a 1.3-fold gradient in standard deviation values for a normal database for attenuation corrected images acquired with a commercially available cardiac pinhole camera. This pattern of noise varies with different patients and with different positioning of the heart within the FOV. Thus, to assist with clinical interpretation, a new 1-minute post-processing technique is developed to provide a patient-specific image of the noise distribution which may augment normal database information. Changes in attenuation result in varying levels of noise between patients of different body habitus administered the same radiotracer activity. A method for creating weight-based protocols is developed that standardizes the average noise in cardiac perfusion images by tailoring the radiotracer activity and acquisition time to the body mass of each patient. Methods developed in this thesis allow for more patient-specific imaging protocols, thereby standardizing the image noise level and providing physicians with more information about the noise and spatial-resolution distribution to aid in image interpretation.

## Statement of Originality

This thesis is a review of the author's core research during her Ph.D. studies at Carleton University. Portions of this work have been previously published in journals or presented as conference abstracts listed below in reverse chronological order.

All work was supervised by Dr. R. Glenn Wells at the University of Ottawa Heart Institute. Dr. Wells provided guidance in development of methodology, analysis, interpretation, and publication. The author used pre-compiled C-code provided by Dr. Wells to iteratively reconstruct images for parallel-hole camera data in Chapter 5 and Chapter 6, and to forward project and iteratively reconstruct pinhole camera images in Chapter 3. The author herself altered Dr. Wells' pinhole forward projection code and recompiled it to implement the rapid noise estimation technique developed in Chapter 4.

Work in Chapter 3 was co-supervised by Dr. Rolf Clackdoyle who provided guidance in the development of methodology and for publication.

To reorient cardiac images and convert to polar map representation, the author used FlowQuant software developed and maintained by Dr. Ran Klein, Dr. Robert deKemp, and Jennifer Renaud (M.Sc.). Ms. Renaud provided guidance regarding the inner workings of FlowQuant enabling the author to alter it to support research reported in Chapter 4 and Chapter 6.

To write emission (projection) data to a Dicom file format after manipulating it in some way in Matlab, the author used "gendicom.exe" software developed by Dr. Amir Pourmoghaddas.

All patient images used in Chapter 4 – Chapter 6 were drawn from the University of Ottawa Heart Institute Nuclear Cardiology Registry managed by Dr. Terrence D. Ruddy.

A subset of patient images that were pre-manipulated and post-processed by the author for Chapter 6 were reconstructed by Duncan Clackdoyle during a summer research assistantship.

All other work was performed by Sarah Cuddy-Walsh under the supervision of Dr. R. Glenn Wells. Specifically, my contributions to the research presented in this thesis are:

- I wrote Matlab code to compute relative resolutions
- I made digital disk phantoms and used my own parameters in Dr. Wells' pinhole image reconstruction software to evaluate spatially dependent resolution of different camera geometries with simulations
- I prepared phantoms (purchased spherical phantom, filled with water-<sup>99m</sup>Tc mixture)
- I acquired all images for physical phantom experiments using one SPECT camera and one SPECT/CT camera
- I invented and developed the PV algorithm, implemented the PV method by writing C and Matlab code, and designed experiments to calibrate and validate the PV algorithm by comparing it with noise determined using a bootstrapping technique [1], [2] which I implemented in Matlab
- I conceived the idea to standardize the level of noise in clinical images using a weight-based activity-time protocol, designed simulations experiments, and developed the relationships between image noise, radiotracer activity, acquisition duration, and patient habitus
- I prepared ethics applications for clinical studies
- I anonymized and exported clinical image datasets from the hospital servers

- I bootstrapped (all) and reconstructed (most, see above) images
- I performed all calculations, evaluation, and statistical analysis using Matlab
- I wrote articles and abstracts, and I presented oral and poster presentations meetings or conferences (oral or poster).

### Peer-reviewed papers

**Cuddy-Walsh, SG**, Wells, RG, “Patient specific estimation of spatially-variant image noise for a pinhole cardiac SPECT camera,” *Medical Physics* 2018; (45)5: 2033-2047.

**Cuddy-Walsh, SG**, Clackdoyle, DC, Renaud, JM, Wells, RG, “Weight-based radiotracer activity dosing to standardize image noise in CZT and conventional cardiac SPECT,” *Journal of Nuclear Cardiology* (submitted).

### Conference Proceedings

**Cuddy-Walsh, SG**, Clackdoyle, R, Wells, RG. “Directional resolution of limited-angle multi-pinhole SPECT cameras,” 2014 IEEE Nuclear Science Symposium and Medical Imaging Conference Record, Seattle, WA, November 2014, pp. 1-4.

### Conference abstracts

1. **Cuddy-Walsh, SG**, Massalha, S, Marvin, BF, Carey, C, Ruddy, TD, Wells, RG, “Evaluating patient-specific z-score images for lesion detection in low count studies,” IEEE Nuclear Science Symposium and Medical Imaging Conference, Sydney, AU, November 2018.
2. **Cuddy-Walsh, SG**, Wells, RG, “Base-to-apex noise gradient with dedicated cardiac and standard SPECT camera designs,” Society of Nuclear Medicine and Molecular Imaging Annual Meeting (SNMMI), Philadelphia, PA, June 2018.  
*Finalist for Best Poster in Instrumentation and Data Analysis.*  
*Published in J. Nuc. Med. 59 (Supplement 1), 1708 (2018).*
3. **Cuddy-Walsh, SG**, Wells, RG, “Differences in cardiac image noise for two SPECT camera designs” University of Ottawa Heart Institute’s Annual Research Day, Ottawa, ON, April 2018.
4. **Cuddy-Walsh, SG**, Wells, RG, “A quick and easy method for patient-specific quantification of spatially varying noise in dedicated-cardiac SPECT images” IEEE Nuclear Science Symposium and Medical Imaging (NSS/MIC), Atlanta, GA, October 2017.

5. **Cuddy-Walsh, SG, Wells, RG,**  
 “Is it noise or abnormality? A method for estimating local noise in a CZT SPECT camera,” Canadian Organization of Medical Physics Annual Scientific Meeting, Ottawa, ON, July 2017.  
*Finalist in the Johns and Cunningham Young Investigators Symposium*
6. **Cuddy-Walsh, SG, Wells, RG,**  
 “Weight-based dosing for consistent image noise in dedicated cardiac SPECT,” Society of Nuclear Medicine and Molecular Imaging Annual Meeting, Denver, CO, June 2017.  
*Published in J. Nuc. Med. 58 (Supplement 1), 28 (2017).*
7. **Cuddy-Walsh, SG, Wells, RG,**  
 “Getting the best image with the lowest dose: weight-based dosing in cardiac nuclear imaging” University of Ottawa Heart Institute’s Annual Research Day, Ottawa, ON, May 2017.
8. **Cuddy-Walsh, SG, Wells, RG,**  
 “Is it noise or defect? A method for estimating local noise in CZT SPECT cameras” University of Ottawa Heart Institute’s Annual Research Day, Ottawa, ON, May 2017.
9. **Cuddy-Walsh, SG, Wells, RG,**  
 “Is it noise or defect? A method for estimating local noise in CZT SPECT cameras” Carleton University’s Life Science Day, Ottawa, ON, May 2017.  
*3<sup>rd</sup> place poster*
10. **Cuddy-Walsh, SG, Wells, RG,**  
 “Designing a better camera: limited-angle nuclear cardiac imaging” University of Ottawa Heart Institute’s Annual Research Day, Ottawa, ON, May 2015.
11. **Cuddy-Walsh, SG, Wells, RG,**  
 “Position-sensitive noise characteristics in multi-pinhole cardiac SPECT imaging,” Canadian Organization of Medical Physicists Annual Scientific Meeting, Banff, AB, June 2014.  
*Published in Med. Phys. 41:8, 3-4 (2014).*
12. **Cuddy-Walsh, SG, Wells, RG.**  
 “Position-dependent noise in multi-pinhole SPECT,” Society of Nuclear Medicine and Molecular Imaging Conference, June 2014.  
*Published in J. Nuc. Med. 55 (Supplement 1), 490 (2014).*
13. **Cuddy-Walsh, SG, Wells, RG,**  
 “Effects of position-dependent count sensitivity on the accuracy of MPI with multi-pinhole cardiac SPECT imaging” The 7<sup>th</sup> Annual Molecular Function and Imaging (MFI) Symposium, Ottawa, ON, June 2014.

## **Acknowledgements**

I would like to acknowledge the following sources of funding, without which this work might not have been possible: the Queen Elizabeth II – Ontario Graduate Scholarship in Science and Technology supported in part by the Ottawa Heart Institute Research Corporation (OHIRC), the Kiwanis Club of Ottawa Medical Foundation & Dr. Kanta Scholarship in Medical Physics, the Carleton Domestic Graduate Student Scholarship, and the American Physics Society (APS) M. Hildred Blewett Fellowship grant which supported my return to my studies following maternity leave (enabling me to upgrade computer equipment, attend conferences, and reduce child care costs). Additionally, I would like to thank the IEEE, the Society of Nuclear Medicine and Molecular Imaging, the Canadian Organization of Medical Physicists, the Carleton University Physics Department, the Canadian Institute for Health Research, APS, and the OHIRC for providing travel support to the numerous conferences that I was privileged to be a part of.

I am grateful to the Carleton University Physics Department. I appreciate the support that I have received in the form of funding application review, nominations for internal funding, incredible courses offered by the department, and accommodating my early departure from TA duties for maternity leave. I'd also like to thank Research Services at the University of Ottawa Heart Institute for their research and funding support as well as for organizing so many internal opportunities to present research to a multi-disciplinary audience within our own institution.

I am infinitely thankful to Dr. Glenn Wells for his steadfast support throughout this six-year journey. His patience, wit, and positivity helped me through both academic and

personal challenges. I am grateful to have had the pleasure of working with Glenn and for his support of my activity in the physics community through participation at conferences and volunteering with physics associations. The example he has set for mentorship, leadership, and friendship is one that I hope to one day emulate.

I also extend my thanks to Dr. Rolf Clackdoyle. Rolf's cheerful nature in the face of jet-lag is a mystery that I've yet to unravel. I have thoroughly enjoyed working with him. His passion for puzzles is contagious and has helped to encourage me to dig deeper into my work. I thank Rolf for useful discussions and lessons in French colloquialisms. a+!

Eva Lacelle has been my hero in the Carleton Physics Department. She regularly wrestled my tangled funding issues into order and made sure everything ran smoothly. Having a cup of tea or a phone chat with Eva was always a joy.

Without a doubt, I must thank my fellow students and colleagues at UOHI. In no particular order, Jennifer Renaud, Paul Prior, Elizabeth Orton, Amir Pourmoghaddas, Spencer Manwell, and Samia Massalha, thank you thank you thank you! These wonderful people have helped me through this degree with friendly hellos in the hall, laughter in the office, lunch outings, workouts at the hospital gym, and rooftop tea breaks. Our chats about physics, heart health, life, and Doctor Who have kept me going. I thank them for sharing their time, challenges, and successes with me.

Finally, I thank my friends and family. To my friends, neighbours, aunts, uncles, and cousins, thank you for your patience, kindness, smiles, cookies, and support. To my parents, I love you as much and more than you always knew. I know that your love and memories will give me strength throughout each step in my life and career. To my husband, thank you for the endless laundry and dishes you have coped with these past

few years. Your strength of your love has helped me through this journey. You are my champion, my person, my love. To my son, thank you for your understanding even when you didn't fully understand why mummy needed to go to work. Thank you to you and daddy for reminding me of the world outside the computer lab. I love exploring that world with you and getting to know my brilliant, funny, and loving boys.

# Table of Contents

<b>Abstract</b> .....	<b>i</b>
<b>Statement of Originality</b> .....	<b>ii</b>
<b>Acknowledgements</b> .....	<b>vi</b>
<b>Table of Contents</b> .....	<b>ix</b>
<b>List of Tables</b> .....	<b>xiv</b>
<b>List of Figures</b> .....	<b>xv</b>
<b>List of Appendices</b> .....	<b>xxi</b>
<b>Abbreviations and Notation</b> .....	<b>xxii</b>
<b>Symbols</b> .....	<b>xxiv</b>
<b>Chapter 1 : Introduction</b> .....	<b>1</b>
1.1    Cardiac Nuclear Medicine.....	2
1.2    Radioactive Decay .....	3
1.3    Justification of Medical Radiation Exposure .....	4
1.4    Projection Data Acquisition .....	5
1.5    Photon Interactions and Energy Discrimination .....	5
1.6    SPECT Imaging Instrumentation .....	7
1.6.1 Collimators .....	10
1.6.2 Photon Detectors and Energy Resolution.....	13
1.6.3 Detector configuration.....	15
1.7    Image Reconstruction.....	16
1.8    Cardiac Image Evaluation .....	20
1.8.1 Image Display.....	20
1.8.2 Normal Database .....	24
1.8.3 Detection and Quantification of Cardiac Hypoperfusion .....	24

1.9	Overview of the Thesis .....	25
<b>Chapter 2 : Review of Spatial Resolution and Image Noise.....</b>		<b>28</b>
2.1	Overview .....	29
2.2	Spatial Resolution .....	29
2.2.1	Measures of Resolution .....	29
2.2.2	Partial Volume Effect.....	31
2.2.3	Parallel-hole and Pinhole Data Sufficiency Requirements.....	32
2.3	Image Noise .....	34
2.3.1	Contributing Factors.....	36
2.3.2	Influence of Body Habitus and Camera Design .....	37
2.3.3	Patient-Specific Imaging Protocols .....	38
2.3.4	Noise Estimation Methods .....	40
<b>Chapter 3 : Directional resolution of limited-angle multi-pinhole SPECT cameras</b>		<b>43</b>
3.1	Introduction.....	44
3.2	Methods.....	45
3.2.1	Camera Configurations.....	45
3.2.2	Mapping Pinhole Visibility .....	46
3.2.3	Theoretical Calculation of Resolution in the FOV.....	46
3.2.4	Resolution from Simulated Disk Phantom.....	48
3.3	Results.....	49
3.3.1	Mapping Pinhole Visibility .....	49
3.3.2	Theoretical Calculation of Resolution in the FOV.....	49
3.3.3	Resolution from Simulated Disk Phantom.....	51
3.4	Discussion .....	52
3.5	Conclusions.....	53

<b>Chapter 4 : Patient-specific estimation of spatially-variant image noise for a pinhole cardiac SPECT camera .....</b>	<b>54</b>
4.1 Introduction.....	55
4.2 Methods.....	56
4.2.1 Camera .....	56
4.2.2 Projected Voxel Noise Estimation ( $\sigma_{PV}$ ) – A new method for estimating local noise in a SPECT image .....	57
4.2.3 Measured Noise ( $\sigma_{BSV}$ ) – Non-parametric bootstrapping.....	61
4.2.4 Application to clinical cases.....	63
4.3 Results.....	65
4.3.1 Sensitivity variability in the field-of-view .....	65
4.3.2 Speed of measurement and calculation .....	67
4.3.3 Noise in Images of a Spherical Phantom.....	68
4.3.4 Validation Evaluating Noise in Clinical Cardiac Images.....	75
4.4 Discussion .....	81
4.4.1 Sensitivity variability in the field-of-view .....	81
4.4.2 Rapid Noise Estimation with the Projected Voxel (PV) Method.....	81
4.4.3 Effect of Reconstruction Algorithm and Prior Strength on Image Noise.....	82
4.4.4 Applications.....	85
4.4.5 Variable noise in the myocardium and its potential impact .....	86
4.5 Conclusions.....	88
<b>Chapter 5 : Patient-specific protocols to standardize image noise.....</b>	<b>89</b>
5.1 Introduction.....	90
5.2 Materials and Methods.....	91
5.2.1 Study Design .....	91
5.2.2 Image Acquisition .....	93

5.2.3	Image Reconstruction.....	94
5.2.4	Camera-dependent Photon Sensitivity .....	95
5.2.5	Noise Calculation .....	95
5.2.6	Developing a Patient-Specific Tracer Activity and Scan Duration Formula .....	96
5.2.7	Validating a Patient-Specific Tracer Activity and Scan Duration Formula .....	99
5.2.8	Statistical Analysis .....	100
5.3	Results.....	100
5.3.1	Camera-dependent Photon Sensitivity .....	100
5.3.2	Developing a Patient-Specific Tracer Activity and Scan Duration Formula .....	101
5.3.3	Validating a Patient-Specific Tracer Activity and Scan Duration Formula .....	102
5.4	Discussion .....	107
5.4.1	Clinical Implications .....	109
5.4.2	Limitations .....	110
5.4.3	New Knowledge Gained .....	111
5.5	Conclusions.....	111
<b>Chapter 6 : Intra-cardiac noise gradient in pinhole SPECT images .....</b>		<b>112</b>
6.1	Introduction.....	113
6.2	Methods.....	113
6.2.1	Study Design .....	113
6.2.2	Image Acquisition and Reconstruction .....	114
6.2.3	Noise and Normal Database Variability Calculation .....	117
6.2.4	Statistical Analysis .....	118
6.3	Results.....	118
6.3.1	Perfusion.....	118
6.3.2	Image Noise.....	120
6.3.3	Normal Database Variability.....	125

6.3.4	Noise and Normal Databases.....	125
6.4	Discussion .....	125
6.5	Conclusions .....	128
<b>Chapter 7 : Summary and Future Directions .....</b>		<b>129</b>
7.1	Summary of Knowledge Gained.....	130
7.2	Future Directions.....	131
7.2.1	Spatially dependent image resolution.....	131
7.2.2	Patient-specific noise image display .....	132
7.2.3	Patient-specific SPECT acquisition protocols.....	132
7.2.4	Identifying statistically significant lesions outside of the LV .....	133
7.2.5	Noise-based camera quality control .....	134
7.3	Final Thoughts .....	134
<b>Appendices.....</b>		<b>136</b>
<b>References .....</b>		<b>164</b>

## List of Tables

Table 1.1 Common Isotopes used for Cardiac SPECT Imaging [6], [7] .....	4
Table 4.1 Calibration coefficients to be used with Equation 16 for the PV method of image noise estimation (Equations 12-13). Determined by fitting linear fit coefficients $MF$ and $BF$ from Equation 14 for 7 different count levels as shown in Figure 4.2(B) - Figure 4.2(C). The coefficient value and 95% confidence interval (CI) is provided for each. Calibration coefficients are specific to 60 iterations of MAP-EM with one-step-late Green's prior ( $\alpha = 0.7$ , $\beta = 0.5$ ) reconstructions.....	68
Table 4.2 Average image noise correlation lengths (CL) for Phantom and Cardiac Patient Studies. Correlation length is defined as the distance in voxel units at which the correlation value in a neighbouring voxel reaches 50% of the variance for a given voxel. The average CL and its uncertainty for the phantom are the mean and standard deviation of CL values measured within the sphere; for the patient studies they are the average over 27 patients of the mean and standard deviation in the CL values within the myocardium.....	73
Table 5.1 Patient Characteristics and Medical History for training and testing of an image noise standardization method. ....	92
Table 5.2 Weight-based administered activity and acquisition scan time formula coefficients, confidence intervals, and Pearson's r-squared values. ....	104
Table 6.1 Characteristics of 93 patients imaged with both SPECT cameras who had normal myocardial perfusion imaging results* .....	115

## List of Figures

- Figure 1.1 (A) Infinia Hawkeye4 and (B) Discovery NM530c cameras by GE Healthcare. (A) Two rotating detector heads with parallel-hole collimators. (B) The central 9 of 19 pinhole-detector pairs in fixed positions in an arc focused on the heart. Waveforms behind each detector schematically approximate signal from counted photons originating from the heart. Typical imaging protocols for both cameras position detectors over an arc spanning from the right anterior oblique to the left posterior oblique of the patient. One transaxial slice of images acquired from the respective cameras and reconstructed with attenuation correction is displayed to demonstrate the approximate position of the horse-shoe-shaped left ventricle (LV) of the heart relative to each camera. The apex (narrow-closed end of the LV) is closer to the top-right while the base (open-end) of the LV is closer to the bottom-left of each image. .... 9
- Figure 1.2 (A)-(C) Parallel-hole and (D)-(E) pinhole collimators used in SPECT cameras. For short septa in (A) & (B) and for pinhole collimators in (D) & (E), resolution varies with object-to-detector distance. Lengthening the septa in (C) improves the resolution but reduces the collimator sensitivity. Objects seen with a pinhole are flipped as images in (D) & (E). The sensitivity of a pinhole collimator depends on its opening angle  $\alpha$  and the distance  $b$  and angle  $\theta$  of the object from the pinhole. The pinhole resolution is dependent upon the  $\alpha$ ,  $b$ , and the distance between the pinhole and detector plane  $a$ . .... 11
- Figure 1.3 General iterative reconstruction algorithm. The cycle is repeated for the desired number of iterations. Comparisons in projection space can be done for all projections as in standard iterative algorithms or for subsets of projections as in OSEM. The last updated image estimate is output as the reconstructed image. .... 17
- Figure 1.4 Standard orientation for interpretation of myocardial perfusion of the left ventricle (LV) in the cardiac reference frame. The right ventricle (RV) is oriented to the left of the LV in the SA and HLA views. .... 22
- Figure 1.5 Left ventricular 17-segment polar map delineation. Segment colours indicate the major arteries responsible for their perfusion: left anterior descending (yellow), right coronary artery (blue), or left circumflex (green). .... 23
- Figure 2.1 (A) Image of a 2D object and (B) horizontal profile through the object. (C) Point spread function (PSF) and (D) line spread function (LSF) of imaging system where \*\* indicates the full-width at half-maximum resolution. (E) Image of the object in (A) blurred by convolution with (C). The profile of (B) convolved with (D) is given in (F). Adding Poisson noise results in the image in (G) and profile in (H). .... 30
- Figure 3.1 Example of the effects of orientation in a pinhole- based SPECT camera with a limited number of angles. Three disks oriented parallel with the x-axis are reconstructed well since the “best” pinhole projection can see the spaces between the disks. When oriented perpendicular to this, the slight shift to the left causes the “best”

pinhole to be unable to see the gaps and thus the reconstructed images are much more blurred. .... 45

Figure 3.2 Pinhole positions are plotted for a SPECT camera with circular sampling over 360° and rectangular arc sampling over 150°. Both designs contain 36 pinholes. The total number of pinholes for which the detector behind the pinhole can see each position (x,y) on the Z = 0 mm plane are displayed using a colour scale with pinhole positions overlaid with white circles. Positions visible through all pinholes (dark red) define the FOV. .... 46

Figure 3.3 Schematic depicting the coordinate and vector system used in Equation 9 to calculate the relative resolution  $R(x, \theta)$  for an object such as a disk at a position,  $x$ , relative to another position,  $x_j$ . The angle between the line drawn between the plane orthogonal to the direction of resolution measurement ( $\theta$ ) and the line drawn from the object to the position of the  $i$ th pinhole is  $\psi_i$ . .... 47

Figure 3.4 Values of theoretical relative resolution,  $R(x, \theta)$ , calculated using Equation 9 are display for the Z=0 plane for pinhole cameras with circular (left) and arc (right) configurations. The scaling factor was  $k = 1$  for all images. The value  $R_x, \theta$  was calculated for four different directions  $\theta$  indicated at the left of each row. The images are comprised of resolution values calculated for each position  $xx, y$  in the FOV (Figure 3.2). The colour scale for the resolution values has a range of 0 to 0.2 for all images except the inset image; the scale of this image has an extended range of 0 to 1 to show the large values outside of the arc. .... 50

Figure 3.5 Disk phantoms were projected and reconstructed with idealized pinholes (0.75 mm thick, 1.5 mm center-to-center, 5.75 mm radius) at various positions along the x-axis (L-R) and downwards from  $x = 23$  mm in the Y-direction. The histograms are plotted from a central profile parallel to the normal vector to each set of reconstructed disks. The predicted relative resolution,  $R(x, \theta)$ , with  $k = 10$  for each is indicated above the histograms. .... 51

Figure 4.1 A central slice through a spherical <sup>99m</sup>Tc-water phantom relative to the positions of the 19 pinholes and detectors (represented by white stars and lines) composing the DNM530c SPECT camera (GE Healthcare). Three views are displayed: (A)-(C) the transverse plane, (D)-(F) the sagittal plane, and (G)-(I) the coronal plane. Each image demonstrates the variation of the relative fraction of detected photons from one region of the quality FOV (represented by a white circle) to another. The variation is calculated using the effects of geometric sensitivity [(A), (D), (G)], attenuation [(B), (E), (H)], and both [(C), (F), (I)]. The 12-cm diameter phantom is centered inside the supported field-of-view of the camera. .... 66

Figure 4.2 Empirical calibration curves and results. (A)The uncalibrated PV noise estimate ( $\sigma_{PV}$ ) is plotted as a function of the noise determined by bootstrapping ( $\sigma_{BSV}$ ) for 7 different image count levels. The (B) slope and (C) intercept of linear fits of each of the data sets in (A) are plotted as a function of the mean number of counts per image voxel ( $F_{object}$ ) and fit with empirical functions (black dots and lines). The

fit functions are used to correct the data in (A) and this is plotted in (D). The slope and intercepts for the calibrated PV noise ( $\sigma_{PV}$ ) are plotted in (B) and (C) with blue squares and dotted lines. All noise values  $\sigma$  and the intercepts are expressed as the percentage of the ‘maximum’ (mean of highest 0.1%) value in the reconstructed sphere. The slope is unitless and the mean counts per voxel is self-explanatory. .... 67

Figure 4.3 Boxplots summarizing the image noise in all voxels of (A) the spherical phantom at 7 different count levels and (B) 31 different cardiac patients. Noise calculated with bootstrapping ( $\sigma_{BSV}$ ) and the projected voxel method ( $\sigma_{PV}$ ) for different count levels by the mean number of counts per voxel inside the phantom ( $F_{object}$ ). The uncalibrated raw PV noise estimate ( $\sigma_{rPV}$ ) is plotted in (A) only. The mean number of counts in the patient myocardium was  $(2.2 \pm 0.4) \times 10^5$ . The circles mark the mean noise value, boxes depict the range from the 1st to 3rd quantiles, and the error bars represent the total range of the variable noise excluding statistical outliers (represented by dots). ..... 70

Figure 4.4 (A) Measured image of spherical phantom at second count level (mean counts  $\sim 2.3 \times 10^5$ ). Noise for this image is determined by (B) bootstrapping ( $\sigma_{BSV}$ ) and (C) the calibrated projected voxel ( $\sigma_{PV}$ ) method. A transverse central slice for each is displayed and units are expressed as the percent of the mean of the maximum 0.1% of voxel values in the sphere. The relationship between the bootstrapping and calibrated PV methods is shown in a (D) voxel-by-voxel scatterplot and (E) a Bland-Altman plot. .... 71

Figure 4.5 Position and directional dependence of the (A) image noise [%] and (B) correlation length [voxels] determined via bootstrapping projection data and reconstructing using 4 different parameterizations: (i) 60 iterations of maximum likelihood estimation maximization (MLEM); (ii) 40 iterations of maximum a posteriori expectation maximum (MAP-EM) with one-step-late Green prior (OSLG) parameters  $\alpha=0.51$  and  $\beta=0.3$ ; (iii) 60 iterations MAP-EM with OSLG prior ( $\alpha=0.7$  and  $\beta=0.5$ ); and (iv) the same as (iii) with dual-energy window (DEW) scatter correction. Central transaxial slices are shown. Each slice has been cropped from  $70 \times 70$  to  $35 \times 35$  voxels. The detector arc (not shown) is positioned to the top and right of the phantom in these images. .... 73

Figure 4.6 Images determined for reconstruction with 60 iterations of MLEM of noisy projections of a uniform digital sphere (15-cm radius) and corresponding attenuation map (15-cm radius). The (A) mean  $\mu_{BSV}$  and (C) standard deviation  $\sigma_{BSV}$  of 400 bootstrapped images is shown. The  $\sigma_{BSV}$  is smoothed using a 1.6 voxel Gaussian kernel. A single image (B) is displayed along with (D) the noise image  $\sigma_{PV}$  estimated with the PV method. Image (E) shows the PV noise estimated with the mean image (A). In (F),  $\sigma_{BSV}$  values are plotted as a function of  $\sigma_{PV}$  values for all points inside the sphere (eroded by 3 voxels). Noise and image values are expressed as a percentage of the maximum voxel value in the true object. .... 74

Figure 4.7 The same images as in Figure 4.6 are shown for reconstruction with 60 MLEM iterations of noisy projections from a uniform digital sphere (15-cm radius)

blurred with a 1.6 voxel Gaussian kernel and enlarged corresponding attenuation map (22-cm radius). All values are expressed as a percentage of the maximum value in the true object. The mean counts per voxel in the simulated sphere is equivalent to the 10 second sphere case ( $F_{\text{object}} = 1.2 \times 10^5$  cnts). ..... 74

Figure 4.8 Measured images and noise images estimated with bootstrapping ( $\sigma_{\text{BSV}}$ ) and the calibrated projected voxel method ( $\sigma_{\text{PV}}$ ) are presented for a  $^{99\text{mTc}}$ -tetrofosmin rest cardiac study of a single patient [#27 from Figure 4.3(B)]. Images are displayed as (A)-(C) transverse and (D)-(F) sagittal slices through the center of the left ventricle in the camera's reference frame. For full visual assessment,  $18 \times 36$  segment cardiac polar maps are also shown of the image (G),  $\sigma_{\text{BSV}}$  (H) and  $\sigma_{\text{PV}}$  (I). Image and noise image values are expressed as a percentage of the maximum voxel values in the myocardium. A (J) scatterplot and (K) Bland-Altman plot show the relationship noise estimate methods. Results from this assessment for all patients are summarized in Figure 4.9. 76

Figure 4.9 Assessment of the variation in the relationship between bootstrapped noise and noise determined by the PV estimation method. A total of 7 phantom cases and 31 patient cases are shown. The comparison for each image is performed in two ways: (1) comparing voxel-by-voxel (VbV) for all voxels in the phantom or myocardium, and segment-by-segment of each  $18 \times 36$  segment cardiac polar map (PM). Markers represent the values for individual cases and lines represent the mean value. Four comparative metrics obtained from Bland Altman analysis (Figure 4.4(D) - Figure 4.4(E) and Figure 4.8(J) - Figure 4.8(K)) are shown as a function of the mean number of counts per phantom or myocardial voxel: (A) slope, (B) intercept, (C)  $R^2$  value, and the (D) coefficient of variation (CV) between noise estimation techniques. .... 79

Figure 4.10 Summary cardiac polar map data for 15 visually normal patient images ( $18 \times 36$  segments displayed). All expressed in units of % of maximum activity. The (A) bootstrapped and (B) estimated local noise images averaged over all 15 patient studies. (C) The standard deviation of the mean images from a bootstrapped distribution for each patient representative of population and physiological cardiac variability. (D) One standard deviation representing the variability between the 15-different patient polar map images. (A)-(D) are on the same color scale with a maximum of 18.9%. (E) A mean polar map image with homogenous activity distribution. .... 80

Figure 5.1 Impact of patient weight due to attenuation on photon sensitivity (Equation 18) for two SPECT cameras. Counts were reported as the sum of all counts in regions of interest around the LV in projection space. The radiotracer activity [MBq] was decay corrected to the start of the image. .... 101

Figure 5.2 Plots to determine the relationship between average image noise and activity  $\times$  scan time (AST) per weight for two cameras (GE Discovery NM530c and GE Infinia Hawkeye4) for images with (AC) and without (NC) attenuation correction. Values are plotted for 43 patients (20 female). Noise values are plotted for the DNM530c images for 2, 1, and 1/4 AST, and for the Infinia images for 1, 1/2, and 1/4 AST. Plots are fit with Equation 21 and results are reported in Table 5.2. .... 103

Figure 5.3 Average image noise [%] plotted as a function of patient weight [kg] without (red-diamond) and with (black-circle or green-square) weight-based patient-specific activity-scan time for the DNM530c and Infinia SPECT cameras: (red-diamond) constant activity-scan time ( $A \cdot T$ ) product for all patients, (black-circle) patient-specific  $A \cdot T$  determined using gender neutral NC coefficients in Equation 22 for a fixed image noise of  $\sigma = 6.1\%$  for the DNM530c and  $16.3\%$  for the Infinia, (green-square) patient-specific  $A \cdot T$  using male- or female-specific NC coefficients to achieve constant image noise of  $16.3\%$  for the Infinia camera. Open and filled markers represent female and male patients respectively. Linear fits of all points for each case are provided in the figure legends. .... 105

Figure 5.4 For the DNM530c camera, (a) one transaxial slice (cropped to  $50 \times 50$  voxels from  $70 \times 70$ ) through the left ventricle of two uptake images reconstructed without attenuation correction. The corresponding noise images are also shown in (b). Images are shown for two patients (52 and 85kg) reprocessed retrospectively to simulate (i) a fixed AST protocol, or (ii) a weight-based AST protocol designed to achieve an average cardiac image noise of  $6.1\%$ . Both colour bars are scaled as a percentage of the maximum voxel value for each image in (a). Note: the heart of the 85 kg patient extends farther to the bottom-left of the field-of-view in a region of reduced photon sensitivity. .... 106

Figure 6.1 Flow chart for calculating intra- and intra- patient image variability. Intra-patient image variability (top row): On the left side, the noise image is computed for each patient as one standard deviation of the 392 statistical replicate images. These are converted to polar map representation (right-circles) and a mean of all noise polar maps is taken to obtain the average image noise. This is an indicator of the average statistical variability if each patient study were repeated (intra-patient). Inter-patient image variability (bottom row): A single image (left-rectangle) for each patient is converted into polar map representation (right-circles). The average of these polar maps for all patients, the normal database (NDB) mean is an indicator of the average relative myocardial perfusion distribution for a given population, camera, and reconstruction method. The standard deviation over single image polar maps for all patients provides the uncertainty in the NDB. The NDB uncertainty is an indicator of the variability of perfusion due to physiological and camera positioning differences in the population in addition to statistical variability. .... 116

Figure 6.2 Mean perfusion images for normal databases for specific camera, reconstruction, and gender-cohorts. Values are calculated from the average normalized perfusion for all polar map segments. Normalization is to the maximum perfusion in each patient image. .... 119

Figure 6.3 Example noise distributions for images of one male patient acquired with the (A & B) DNM530c and (C & D) Infinia cameras and reconstructed (B & D) with and (A & C) without attenuation correction. The average noise is  $7.5\%$  in basal segments and  $4.1\%$  in apical segments in (B); it is  $13.4\%$  and  $11.3\%$  respectively in (D). ..... 121

Figure 6.4 Stochastic image noise due to camera design and attenuation dependent differences in photon counting. This contribution is calculated as the average of all individual intra-patient noise polar map segments. NC and AC perfusion images are averaged over all male and female patients imaged with the DNM530c and Infinia cameras. .... 122

Figure 6.5 The same camera and attenuation dependent noise images as in Figure 6.4 with the scales unified to a maximum value of 17.3 for direct comparison with the uncertainty in the normal database in Figure 6.6. .... 123

Figure 6.6 Camera, reconstruction, and gender-specific normal database uncertainty images calculated as one standard deviation of normalized perfusion for all polar map segment values corresponding to normal MPI results. The maximum value of the scale is 17.3% of the maximum perfusion. .... 124

Figure A.1 Example of alignment of non-attenuation corrected SPECT image from the DNM530c camera with CT anatomy image from the Infinia Hawkeye4 camera for the same patient. Image is a screen capture from the Myovation application with the GE Healthcare Xeleris software package used for alignment and generation of attenuation maps. The three columns correspond to from left to right, the short axis (SA), vertical long axis (VLA), and horizontal long axis (HLA) views of the left ventricle of the heart. The three rows correspond from top to bottom to the CT image, the SPECT reconstructed image, and the CT image overlaid with a contour of the left ventricle from the SPECT image. CT data is translated and rotated (if necessary) to contain the SPECT contours within the volume of the heart approximately in the location of the LV. Care is taken to ensure that LV activity does not overlap with lung or ribs on the CT image. .... 137

Figure B.1 Noise for all voxels in a spherical phantom as calculated with 15 repeat acquisitions or M bootstrapped replicates. (A)-(H): Bland Altman plots displaying the difference between the two methods. The mean is shown as a solid line and on standard deviation is shown by the dashed lines. (I): One standard deviation of the difference between methods is expressed as a percentage of the average noise for 15 repeat acquisitions and related with a power function to the number of bootstrapped replicates. .... 140

Figure B.2 Noise for all voxels in a spherical phantom as calculated with different numbers M of bootstrapped replicates. (A)-(H): Bland Altman plots displaying the difference between the M replicates and M = 1000 replicates. The mean is shown as a solid line and on standard deviation is shown by the dashed lines. (I): One standard deviation of the difference between methods is expressed as a percentage of the average noise for M = 1000 and related with a power function to the number of bootstrapped replicates. .... 141

## List of Appendices

<b>Appendix A - Emission and CT registration for attenuation correction.....</b>	<b>137</b>
<b>Appendix B - Required number of bootstrapping replicates for noise calculation</b>	<b>138</b>
<b>Appendix C - BMI-based patient-specific imaging protocol for Chapter 5 .....</b>	<b>142</b>
<b>Appendix D - Permission to reproduce published material.....</b>	<b>143</b>
D.1    Chapter 3 .....	144
D.2    Chapter 4 and Part of Section 2.3.....	145
<b>Appendix E - Research Ethics .....</b>	<b>146</b>
E.1    REB approval for research contributing to Chapter 4 and Chapter 6 .....	147
OHSN-REB Letter of Approval .....	147
OHSN-REB Renewal Report .....	148
CUREB-B Letter of Approval .....	149
Ethics protocol.....	151
E.2    REB approval for research contributing to Chapter 5 .....	156
OHSN-REB Letter of Approval .....	156
CUREB-B Letter of Approval .....	157
Ethics protocol.....	159

## Abbreviations and Notation

1D, 2D, 3D	1, 2, or 3-Dimensional
AC	Attenuation Correction or Attenuation Corrected Image
ACSC	Attenuation and Scatter Corrected Image
ALARA	As Low As Reasonably Achievable
ASNC	American Society of Nuclear Cardiology
AST	Activity-scan time [MBq · min]
BMI	Body Mass Index [kg/m <sup>2</sup> ]
BSV	Bootstrap determined voxel-by-voxel noise
CL	Correlation Length
CM	Collimator modelling
CT	Computed Tomography
CUREB-B	Carleton University Research Ethics Board – B
CV	Coefficient of Variation
CZT	Cadmium Zinc Telluride
DEW	Dual Energy Window scatter correction
DNM530c	Discovery NM530c SPECT camera (GE Healthcare)
EC	Electron Capture
ECG	Electrocardiography
FOV	Field-of-view
FWHM	Full-Width at Half-Maximum
HLA	Horizontal Long Axis
IT	Isomeric Transition
Infinia	Infinia Hawkeye4 SPECT/CT camera (GE Healthcare)
keV	Kiloelectron volts (units of photon energy)
kg	Kilograms
LEHR	Low-Energy High-Resolution collimator
LSF	Line Spread Function
LV	Left Ventricle
MAP-EM	Maximum a Posteriori Expectation Maximization
MBF	Myocardial Blood Flow
MBq	Mega Becquerel
mCi	Millicurie
MeV	Megaelectron Volt
MLEM	Maximum-Likelihood Expectation Maximization
MPI	Myocardial Perfusion Imaging
mSv	Millisievert

MTF	Modulation Transfer Function
NaI	Sodium Iodide
NC	Non-attenuation Corrected images
NDB	Normal Database
OHSN-REB	Ottawa Health Science Network Research Ethics Board
OSEM	Ordered-Subset Expectation Maximization
OSLG	One-Step Late Green's prior
PET	Positron Emission Tomography
PM	Polar Map
PMT	Photomultiplier tube
PSF	Point Spread Function
PV	Projected Voxel noise estimation method
PVE	Partial Volume Effect
QFOV	Quality Field-of-View
$R^2$	Pearson's correlation coefficient
REB	Research Ethics Board
ROI	Region of Interest
rPV	Raw (uncalibrated) PV method
RR	Resolution recovery
RV	Right Ventricle
SA	Short Axis
SC	Scatter Correction
SD	Standard Deviation
SDS	Summed Difference Score
SiPM	Silicon Photomultiplier
SPECT	Single Photon Emission Computed Tomography
SPS	Summed Perfusion Score
SRS	Summed Rest Score
SSS	Summed Stress Score
UOHI	University of Ottawa Heart Institute
VbV	Voxel-by-Voxel
VLA	Vertical Long Axis
Weight	Body mass [kg]

## Symbols

$A$	Decay corrected activity
$A_0$	Initial activity
$a$	Pinhole-to-detector distance
$a_{pd,v}$	Voxel and pinhole-detector dependent attenuation contribution to camera sensitivity calculation
$\bar{a}$	Average attenuation contribution to camera sensitivity calculation
$\vec{a}_i$	$i^{\text{th}}$ pinhole position
$\alpha$	Pinhole aperture acceptance angle
$b$	Pinhole-to-object radial distance
$C_{meas}$	Number of photon counts measured
$C_{norm}$	Number of photon counts measured per megabequerel minutes
$COV$	Covariance between voxel values at two positions
$d$	Pinhole aperture diameter
$d_e$	Effective pinhole aperture diameter
$\xi$	Specifier of geometric sensitivity, attenuation, or both factor inclusion
$F_v$	Image voxel value
$\bar{F}_v$	Average voxel values over $N$ image replicates
$\bar{F}_{Object}$	Average voxel value in an object (sphere phantom or myocardium)
$g$	Geometric sensitivity
$\bar{g}$	Geometric sensitivity average for camera
$g_{pd,v}$	Geometric sensitivity for a pinhole-detector pixel and voxel position
$i$	Pinhole index
$k$	Scaling factor to approximately convert unitless relative resolution into physics resolution units
$k_1, k_2$	Coefficients for patient-specific activity-scan time imaging protocols
$\lambda$	Activity decay constant
$m_1, m_2, b_1, b_2$	Calibration coefficients for $M_{\bar{F}}$ and $B_{\bar{F}}$
$M_{\bar{F}}, B_{\bar{F}}$	Calibration functions for PV method dependent on $\bar{F}_{Object}$
$\mu$	Mean image
$N$	Number of image realizations or bootstrapped replicates
$p$	Statistical P-value
$pd$	Pinhole-detector pixel index
$R$	Resolution (mm)
$R(\vec{x}, \hat{\theta})$	Relative resolution (unitless)
$\sigma$	Image Noise
$\sigma_v^2$	Ensemble voxel variance for one voxel position
$\sigma_{rPV}$	Uncalibrated PV noise
$\sigma_{PV}$	Calibrated PV noise
$\sigma_{BSV}$	Bootstrapped noise
$\psi_i$	Angle between the $i^{\text{th}}$ pinhole and the plane perpendicular to the direction of resolution measurement
$T$	Duration of image acquisition

$t$	Time since initial activity measurement
$\theta$	Angle between photon path and collimator plane
$\hat{\theta}$	Unit vector indicating the direction of resolution measurement or normal to a disk surface to orient a disk phantom
$v$	Voxel position index
$W$	Body mass [kg]
$\vec{x}$	Position of resolution measurement

## **Chapter 1: Introduction**

*An overview of cardiac SPECT imaging and SPECT camera design.*

## 1.1 Cardiac Nuclear Medicine

With approximately 1 in 12 adults aged 20 years old and over living with heart disease and 12 Canadians dying from it every hour, heart disease continues to be the second leading cause of death and disability in Canada [3]. Healthcare costs currently make up approximately 11.5 percent of Canada's gross domestic product [4]. As obesity, diabetes, and age are three risk-factors for heart disease, the increasing prevalence of obesity and diabetes, and the increasing age of the population may all lead to further increases in healthcare costs and requirements. Myocardial perfusion imaging (MPI) is a powerful radioisotope-based non-invasive tool used to detect, monitor, and manage heart disease. The most commonly used technique for MPI is single photon emission computed tomography (SPECT). In SPECT MPI, a radioisotope labelled tracer that accumulates in the perfused cardiac muscle tissue (myocardium) is injected into the bloodstream. Decay of the radioisotope results in the emission of energetic photons. The number and energy of the photons that escape the body are measured by detectors on a SPECT camera outside of the patient, recorded, and used to create a three-dimensional (3D) image of the tracer distribution in the myocardium and surrounding tissues/cavities.

The left ventricle (LV) is the workhorse of the heart. SPECT MPI detects heart disease in the LV based on differences in the signal from accumulated radiotracer (*uptake*) between different regions of the heart wall (*myocardium*). Narrowed or blocked coronary arteries and capillaries, associated with cardiovascular atherosclerosis, restrict blood flow to downstream myocardial tissues. In a healthy heart, a cardiac SPECT study will show relatively uniform image signal intensity. Impaired myocardial perfusion appears as a relative reduction in image signal intensity in the region of the heart supplied by diseased

blood vessels due to a restriction in blood flow. To identify ischemic heart disease, for which blood flow is restricted under stress conditions but otherwise normal, MPI is typically performed at both rest and stress.

## 1.2 Radioactive Decay

Nuclear imaging is based on the detection of photons resulting from the decay of a radioisotope. Decay occurs when an unstable atom releases energy in the form of a particle or photon [5]. The rate of decay or *activity* decreases exponentially with time  $t$  and characterized by a decay constant  $\lambda$  that depends on the isotope. The activity is defined as the number of atoms decaying per second. The instantaneous activity  $A$  at time  $t$  is given by Equation 1 with respect to  $A_0$  the activity at  $t = 0$ .

$$A = A_0 e^{-\lambda t} \quad (1)$$

The half-life  $t_{1/2}$  is equal to  $\ln(2)/\lambda$  and refers to the time it takes for the activity of an isotope sample to be halved. Half-lives for common cardiac SPECT radioisotopes are listed in Table 1.1. Activity is commonly expressed in units of megabecquerels (MBq) where 1 MBq corresponds to  $10^6$  counts per second (cps), or in units of millicuries (mCi) where 1 mCi corresponds to 37 MBq.

The primary mode of decay for isotopes used in cardiac SPECT is either electron capture (EC) or isomeric transition (IT) [5]. In electron capture, an orbital electron is captured by the nucleus of an atom and a proton transforms into a neutron. The resulting orbital hole is filled by an electron from a higher orbital shell which loses energy in the form of characteristic x-rays (photons). For  $^{201}\text{Tl}$  these characteristic x-rays have energy sufficient to escape the body, allowing it to be used for SPECT imaging. EC can leave atoms (such as Iodine-123) in an excited metastable state. An atom in an excited

**Table 1.1 Common Isotopes used for Cardiac SPECT Imaging [6], [7]**

Isotope	Half-life	Photon Energy	Source	Tracer	Indications
<sup>99m</sup> Tc	6.02 hours	140.5 keV	<sup>99</sup> Mo Generator	Sestimibi	MPI
			Linear Accelerator	Tetrofosmin	MPI
			Cyclotron	Red Blood Cells	Cardiac ejection fraction
<sup>123</sup> I	13.2 hours	159 keV	Cyclotron	BMIPP*	Fatty-acid metabolism
				MIBG†	Sympathetic innervation
<sup>201</sup> Tl	73.1 hours	70-80 keV‡	Cyclotron	TlCl or Tl+	MPI

\* <sup>123</sup>I-BMIPP – beta-methyl-p-<sup>123</sup>I-iodophenyl-pentadecanoic acid

† <sup>123</sup>I-MIBG – <sup>123</sup>I-metaiodobenzylguanidine

‡ Characteristic x-rays over a range of 70-80 keV

metastable state is called an isomer. Isomers can also be formed via beta decay of a parent particle such as the decay of Molybdenum-99 to Technetium-99m (<sup>99m</sup>Tc). <sup>99m</sup>Tc and Iodine-123 are two isomers commonly used in cardiac SPECT imaging. An isomer will eventually lose its energy by emitting a photon via an isomeric transition. For this dissertation, all imaging was performed using <sup>99m</sup>Tc-labelled Tetrofosmin which emits 140.5 keV photons and has a high affinity for uptake in the myocardium.

### 1.3 Justification of Medical Radiation Exposure

When discussing nuclear medicine, the public is often concerned with risk associated with radiation exposure. Imaging protocols for same-day stress-rest or rest-stress MPI with standard SPECT cameras call for radiotracer activities of 296–444 MBq (8–12 mCi) and 888–1332 MBq (24–36 mCi) for the first and second studies [8]. These correspond to an effective dose to the patient of approximately 9.3 mSv for a complete study with Tetrofosmin, assuming activities of 370 and 1110 MBq. In comparison, the annual background dose is 1.8 mSv in Ottawa, Canada [9]. While the risk of stochastic effects (cancer, hereditary disorders, etc.) due to non-lethal cell damage from a single study is low, the probability associated with this risk increases with multiple exposures for

patients and staff. As such it is important to balance the clinical need for tests against their radiation risk. To maximize the risk-benefit ratio, the radiotracer activity is kept as low as reasonably achievable (ALARA) [7], [10]. The benefit of a nuclear test is dependent on obtaining high-quality images. Thus, in practice, the ALARA principle translates to ensuring that the activity should be kept as low as possible without sacrificing diagnostic quality of the images.

#### **1.4 Projection Data Acquisition**

The raw data for SPECT images are created by counting photons that have exited the body, measuring their energy, and inferring their direction of origin. SPECT cameras have detectors that can be positioned at various locations and angles relative to the patient. Each detected photon is counted and recorded along with information about the time of detection, location of the detector, and energy of the detected photon. A file containing all this information is termed a *list-file* (acquired in list-mode). Since list-files are large, an alternative approach is to only record the number of photons detected at each location in the detector within a pre-chosen range of photon energies. Data acquired at each detector head position form a two-dimensional image termed a *projection*.

Projections are acquired from a variety of different positions around the patient. The full set of 2D projections is called a *projection set*. (The projection set is used to reconstruct a three-dimensional tomographic image of the distribution of radiotracer in the patient.)

#### **1.5 Photon Interactions and Energy Discrimination**

Not all photons emitted from radioisotopes escape the body and travel through the collimator unaltered to be detected. Photons emitted from isotopes used in cardiac imaging have the potential to interact with body tissues one or more times or to be fully

absorbed via three forms of interaction: Compton scattering, photoelectric absorption, or coherent scattering [11]. In body tissues, photons primarily interact by Compton scatter which changes their direction of travel and reduces their energy. Photons that undergo photoelectric absorption in body tissue or camera collimators will not be detected. At energies on the order of 0.1 MeV, a small fraction of photons may experience small direction changes and without energy loss due to coherent scattering [5], [7], [11].

Since it is difficult to determine the origin of scattered photons detected by a SPECT camera it is undesirable to include them in the projection data from which an image is reconstructed. They increase the apparent background signal and thus reduce the signal-to-background ratio. The energy of most scattered photons is lower than the energy of primary (unscattered) photons. This fact can be used to exclude scattered photons (*scatter*) that are detected outside of a chosen primary energy window (typically  $140.5 \text{ keV} \pm 10\%$  for  $^{99\text{m}}\text{Tc}$ ) thus increasing the fraction of primary photons in the projection data. However, due to the finite energy resolution (see Section 1.6.2) of the SPECT detectors some scattered photons will be recorded in the primary energy window and some primary photons rejected by energy discrimination [11]. Scatter correction techniques can be used to recover image contrast and quantitative accuracy that is degraded by misidentification of photon energies. A detailed discussion of scatter correction methods is outside of the scope of this thesis but the interested reader is referred to reviews on current scatter compensation strategies in the literature [12]–[18].

The probability of photon interaction in an object increases with thickness and density of the tissue/material between the photon origin and the detector. Due to this photon *attenuation*, the fraction of photons detected in the primary energy window is generally

lower from positions deep (thicker tissue) in a patient compared with those close to the surface. This means that in a three-dimensional image, regions in the patient that are deepest in the tissue relative to the camera detectors will have reduced apparent signal. It also means that the apparent signal will be lower for patients with large body habitus than for petite patients. Since patient tissue is heterogenous, the attenuation along the path from source to detector depends on the various tissue densities in addition to their thickness (path length). Determining the attenuation of signals from within a patient thus requires a map of the distributions of the different patient tissues. Maps of tissue-specific attenuation are most often generated by acquiring a computed tomography (CT) image and converting it into a map of the mass attenuation coefficients associated with the energy of the primary SPECT photons [19]–[21]. The *attenuation map* can be incorporated into the image reconstruction process (Section 1.7) to correct attenuation-based reductions in signal in a tomographic image.

## **1.6 SPECT Imaging Instrumentation**

The performance of a SPECT camera is highly dependent upon its components and their arrangement. Collimators are necessary to provide information about the direction of a photon's origin and photodetectors are essential for counting the photons that pass through the collimator. The overall efficiency of a SPECT camera is dependent on the geometric sensitivity of the collimator, the detection efficiency of the photon detectors, and the number and position of the collimator-detector heads. A discussion of these can be found in Sections 1.6.1, 1.6.2, and 1.6.3.

Standard SPECT cameras rotate one or more detector heads with parallel-hole collimators about an object to obtain the projection set. Due to the importance of cardiac

imaging, dedicated cardiac SPECT systems have been developed that employ novel collimation with multiple detector heads at fixed positions. Specifications of one standard SPECT camera design and one dedicated-cardiac design with pinhole collimation are provided in this section and illustrated with the schematic in Figure 1.1.

### **Infinia Hawkeye-4 SPECT/CT**

The Infinia Hawkeye-4 (GE Healthcare, Haifa, Israel) is a standard SPECT camera design with two rotating camera heads (Figure 1.1A) [22]. Each of the 540 mm × 400 mm heads is composed of a parallel-hole collimator and a 9.5 mm thick monolithic NaI scintillation crystal coupled to 59 circular PMTs [22]. Detector heads can be positioned perpendicularly in L-mode and then rotated step-wise over 90° for a total of 180° angular sampling (Figure 1.1A). The matrix size for a projection from a typical Infinia cardiac acquisition is 64 × 64 pixels with a side length of 6.797 mm. The reconstructed image is typically 64 × 64 × z voxels with side length of 6.797 mm where the number of slices z depends on the extent of axial sampling. In our clinic, we use low-energy high-resolution (LEHR) collimators containing 86300 hexagonal holes 1.5 mm in diameter, 35 mm long, and with 0.2 mm septal thickness [22]. The clinical protocol used throughout this dissertation acquired data for 25.6 seconds at each detector head position in steps of 3° over 180° for a total image acquisition duration of 12.8 min. (Note: the clinical acquisition duration was ~13.8 min due to a 2 second delay for camera rotation between projection acquisitions.)

The Hawkeye-4 computed tomography (CT) scanner attached to the Infinia camera uses x-rays to provide anatomical information which can also be used for attenuation correction of SPECT images. For this dissertation all CT imaging was performed with

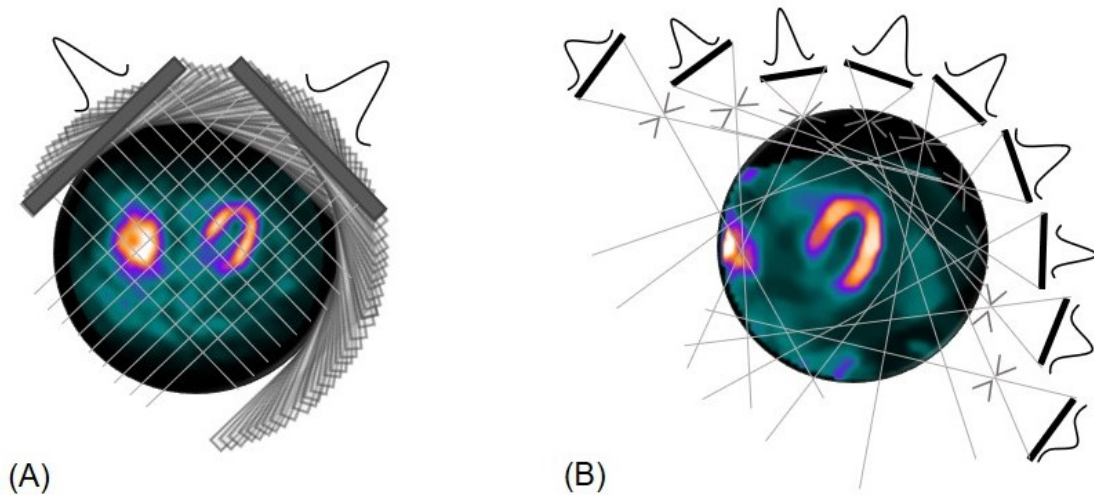


**Figure 1.1 (A) Infinia Hawkeye4 and (B) Discovery NM530c cameras by GE Healthcare. (A) Two rotating detector heads with parallel-hole collimators. (B) The central 9 of 19 pinhole-detector pairs in fixed positions in an arc focused on the heart. Waveforms behind each detector schematically approximate signal from counted photons originating from the heart. Typical imaging protocols for both cameras position detectors over an arc spanning from the right anterior oblique to the left posterior oblique of the patient. One transaxial slice of images acquired from the respective cameras and reconstructed with attenuation correction is displayed to demonstrate the approximate position of the horse-shoe-shaped left ventricle (LV) of the heart relative to each camera. The apex (narrow-closed end of the LV) is closer to the top-right while the base (open-end) of the LV is closer to the bottom-left of each image.**

helical acquisitions using a gantry rotation speed of 2.0 rpm, x-ray tube voltage of 120 kVp, and tube current of 1.0 mA. While evaluation of the CT is not in the scope of this thesis it should be noted that the additional acquisition of a CT image for attenuation correction increases the total study dose by approximately 0.4 mSv. [23]

### **Discovery NM530c SPECT**

The Discovery NM530c (DNM530c; GE Healthcare, Haifa, Israel) has 19 pinhole-detector pairs positioned along three parallel L-shaped arcs. Two arcs of 5 detectors each are positioned axially above and below the central arc of 9 detectors (Figure 1.1B). The detectors are positioned and angled to focus on the heart. Individual detector panels are comprised of an array of  $32 \times 32$  pixels of cadmium zinc telluride (CZT) with a side length of 2.46 mm. Each collimator has a single pinhole aperture with a 5-mm diameter

[24]. Owing to the stationary detector heads, data are acquired for all 19 views simultaneously and with optional list-mode data storage. Acquisitions are reconstructed in an object array of  $70 \times 70 \times 50$  voxels with voxel size of  $4 \text{ mm} \times 4 \text{ mm} \times 4 \text{ mm}$  using Xeleris software (GE Healthcare, Haifa, Israel). While the DNM530c does not have an onboard CT, anatomical images can be imported from another camera and manually co-registered in Xeleris for reconstructions with attenuation correction. The volume in the field-of-view (FOV) of the reconstructed image that is fully viewed by all 19 detectors, the *quality FOV* (QFOV), is roughly an ellipsoid with the both axes being slightly under 19-cm [25]. The DNM530c protocol used throughout this dissertation acquired data for 8 minutes, the first 5 minutes of which were reconstructed for clinical evaluation.

### **1.6.1 Collimators**

To form an image of the source of single photons as in SPECT, a physical collimator is required to provide directional information. A collimator is a thick sheet of material with a high attenuation coefficient, such as lead or tungsten, that has one or more perforations to preferentially select photons from specific directions [11]. The most common is the parallel-hole collimator traditionally used by gamma cameras such as the Infinia. More recently, other dedicated cardiac designs have been proposed such as the DNM530c that employs pinhole collimators. Schematics of parallel-hole and pinhole collimator designs are provided in Figure 1.2.

#### **Parallel-hole Collimators**

Parallel-hole collimators are comprised of an array of tightly configured holes perpendicular to the face of a sheet of collimating material. Such collimators ideally allow for detection of only photons travelling parallel to the normal of the detector plane.

The collimator walls between the parallel holes are called *septa*. The septa prevent penetration of photons from one hole into another. A trade-off exists between resolution and sensitivity when selecting the size and length of collimator holes. High resolution collimators with reduced sensitivity have small-diameter long holes to limit the acceptance angle of incoming photons (Figure 1.2C). Lower resolution but higher sensitivity collimators have shorter, larger-diameter holes which improve photon collection efficiency by allowing photon acceptance from broader angles but in doing so lose directional precision (Figure 1.2B).

Triangular, square, or hexagonal shaped holes are most commonly used in SPECT collimators to ensure equal septa thickness within a periodic lattice structure of the holes. The sensitivity or fraction of emitted photons that reach the detector through the

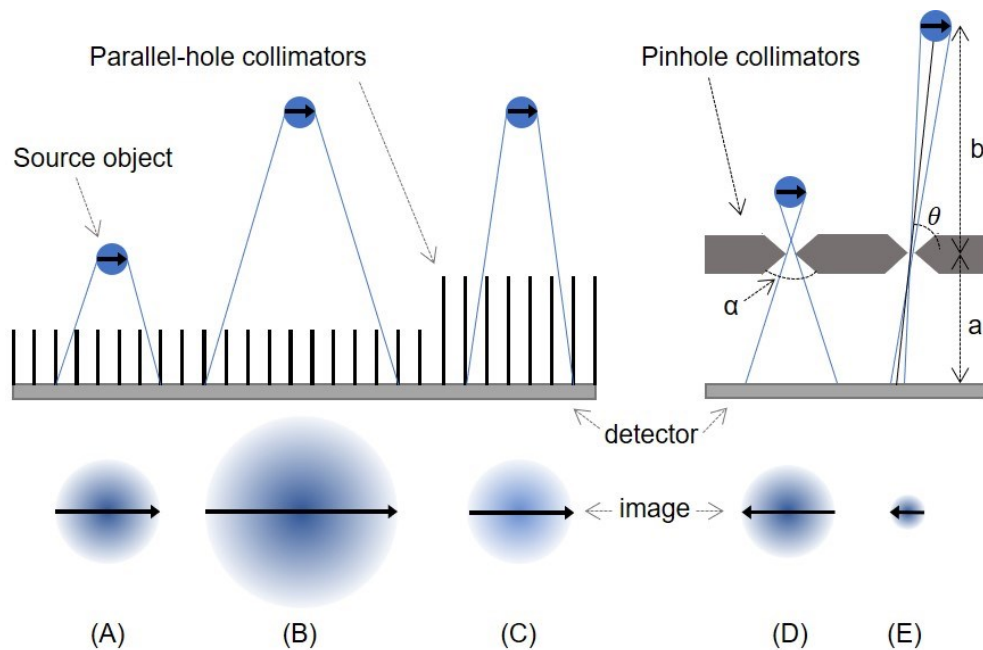


**Figure 1.2 (A)-(C) Parallel-hole and (D)-(E) pinhole collimators used in SPECT cameras. For short septa in (A) & (B) and for pinhole collimators in (D) & (E), resolution varies with object-to-detector distance. Lengthening the septa in (C) improves the resolution but reduces the collimator sensitivity. Objects seen with a pinhole are flipped as images in (D) & (E). The sensitivity of a pinhole collimator depends on its opening angle  $\alpha$  and the distance  $b$  and angle  $\theta$  of the object from the pinhole. The pinhole resolution is dependent upon the  $\alpha$ ,  $b$ , and the distance between the pinhole and detector plane  $a$ .**

collimator is approximately uniform within the FOV of the collimator. The full-width at half-maximum (FWHM) resolution of a parallel-hole collimator increases linearly with distance from the detector plane (Figure 1.2A- Figure 1.2B). Thus, two sources close to the collimator will be better resolved than two sources farther away.

The geometric sensitivity of the Infinia camera is approximately 72 cps/MBq (or a fraction of  $7.2 \times 10^{-5}$ ) per detector head or 144 cps/MBq ( $1.44 \times 10^{-4}$  fractionally) for both heads and the resolution is 7.4 mm at 100 mm from the detector head [22].

### **Pinhole Collimators**

A pinhole collimator has single circular aperture in dense collimator material. The aperture is conical in shape through the thickness of the material with an opening angle  $\alpha$  which limits the acceptance angle for detecting photons (Figure 1.2D-Figure 1.2E). Photons passing through the aperture form an inverted image of their source on the detector as shown in Figure 1.2D-Figure 1.2E. Pinhole collimators produce a minifying effect if the distance from the source to the pinhole is greater than the distance from the pinhole aperture to its corresponding detector. An image is magnified if the source-to-pinhole distance is less than the pinhole-to-detector distance.

The photon detection efficiency (sensitivity) and geometric resolution both vary with distance of the source from the pinhole. The geometric sensitivity  $g$  is defined as the fraction of photons emitted from the source that pass through the pinhole aperture. This is independent of whether or not photons are recorded by a detector. Shown mathematically in Equation 2 and 3,  $g$  decreases with increasing radial distance  $b$  from the pinhole and with decreasing angle  $\theta$  between the path of the photon and the pinhole collimator plane [26], [27].

$$g = \frac{d_e^2 \sin \theta}{16b^2} \quad (2)$$

The geometric sensitivity at the centre of the quality field of view of the DNM530c camera is approximately 656.8 cps/MBq [24], about 4.5-fold better than the Infinia. Due to photon penetration at the thin edges of the aperture, the effective aperture diameter  $d_e$  (Equation 3) is larger than the physical aperture diameter  $d$ . The size of the aperture blurring effect is dependent on the linear attenuation coefficient  $\mu$  of the collimator material (3.6 mm<sup>-1</sup> for tungsten and 140.5 keV photons) and the full acceptance angle  $\alpha$  of the aperture [28], [29].

$$d_e = \sqrt{d \left( d + \frac{2}{\mu} \tan \frac{\alpha}{2} \right)} \quad (3)$$

For fixed intrinsic detector resolution and pinhole-to-detector distance  $a$ , higher image resolution (smaller  $R$ ) is obtained for objects close to the aperture than for objects far from it.

$$R = \frac{(a + b)d_e}{a} \quad (4)$$

This means that when imaging extended objects from one direction, the image resolution may be better for the close side than for the far side.

## 1.6.2 Photon Detectors and Energy Resolution

Behind the physical collimator, a detector is the instrumentation that absorbs the inbound photon energy via photoelectric absorption (and Compton scattering) and outputs an electronic signal for analysis. The detector type is named for its method of conversion from gamma photon to electric signal: indirect or direct conversion [30]. To avoid confusion in this section, inbound photons are termed *gamma photons* to differentiate them from photons with energies in the visible spectrum (*visible photons*).

Detection of photons requires the energy from each gamma photon to be converted to charges that can be counted by readout electronics. The number of charge carriers generated in the detector is proportional on average to the energy of the detected photon but the exact number of carriers, and the corresponding detected signal, varies randomly about the mean value [7]. The mean and width (full-width half-maximum, FWHM) of the spread of detected signals provide the energy of the photopeak and *energy resolution* of the photon detector.

### **Indirect conversion detectors**

Indirect conversion or “scintillation” detectors use a two-step process to detect gamma photons. They employ a scintillation material that is very transparent to visible light, but which has a high stopping power for the incident gamma photons. The most common SPECT scintillation material is a sodium-iodide (NaI) crystal, which is coupled with a photodetector such as a photomultiplier tube (PMT) or silicon photomultiplier (SiPM) [27], [30]. Inbound gamma photons are converted by the scintillator to visible photons. Scintillation materials such as NaI produce 1 optical photon per 24.4 eV (41000 photons/MeV) to produce ~5760 photons for a 140.5 keV gamma photon [7]. These are subsequently detected by a photodetector which converts them into an electric signal proportional to the number of photons detected.

The resulting signal amplitude is proportional to the energy of the inbound gamma photon. The energy resolution of the scintillation detector is dependent on the stopping power of the scintillator (ideally all of the gamma photon energy is converted to visible light), the light yield of the scintillator (number of visible photons generated per keV), the transparency of the scintillator (all photons should ideally reach the photodetector), the

efficiency of the photodetector for detecting the photon wavelength, and the amplification of electrons inside the photodetector (needed to provide a signal exceeding electronic noise in readout circuitry).

### **Direct conversion detectors**

Direct conversion detectors are made of high stopping power materials such as cadmium zinc telluride (CZT). They absorb inbound gamma photons which induce charge proportional to the gamma energy [24], [30]. The energy resolution of direct conversion detectors depends on the stopping power of the material, the number of charges liberated, and mobility of the charge (ability to reach readout electronics). CZT detectors liberate 1 electron-hole pair per 5 eV to produce 28100 charge for a 140.5 keV gamma photon. As such, direct conversion detectors such as CZT-based technology typically have improved energy resolution (6%) compared with NaI-PMT detectors (10%) [7], [8]. This allows the DNM530c camera potentially to have a higher primary-to-scatter photon ratio than the Infinia.

#### **1.6.3 Detector configuration**

The number, position, and angle of detector heads in a fixed detector SPECT system impacts its overall sensitivity and resolution performance. Due to the isotropic emission of gamma photons from a source, a patient would need to be positioned inside of a sphere of detectors to sample all angles and maximize photon sensitivity. While complete spherical coverage may not be practical, the DNM530c captures a larger solid angle around the patient and so has greater detection efficiency with 19 stationary pinhole-detectors than the Infinia does with 2 detector heads. The schematic of the detector configuration for these cameras is provided in Figure 1.1. Even though the detection

efficiency of an individual pinhole-detector head is less than that of a parallel-hole detector head, the total geometric efficiency of 19 detectors on the DNM530c is approximately 4-fold greater [24] than for 2 detectors on the Infinia (for a source near the center of the DNM530c FOV). Provided the same activity is present in the object or patient, this allows for lower total imaging times with the DNM530c; lower injected radiotracers activities may also be used. It also enables dynamic imaging such as with studies of myocardial blood flow [31], [32].

With both cameras, emission data for cardiac studies are acquired over approximately 180°. Effects of tissue attenuation (Section 1.5) will lead to subtle differences in photon detectability in the FOV for both parallel hole and pinhole collimated systems. Additionally, the source position-dependent sensitivity of pinhole-detectors (Equation 2) further complicates the pattern of photon detectability inside the QFOV of the DNM530c [33]. GE Healthcare emphasizes the need to position the heart inside the QFOV to avoid truncating it in any projections and their software corrects for positionally dependent sensitivity changes. Chapter 4 and Chapter 6 discuss the not previously known effect of position-dependent sensitivity on image noise inside the QFOV. Even the spatial resolution of a reconstructed image also depends in part on the number of viewing angles acquired as part of the projection data set and is discussed further in Section 2.2.3.

## **1.7 Image Reconstruction**

Image reconstruction refers to the process of inferring a three-dimensional image of an object volume from 2D projection data sets. A *pixel* is a sub-unit of the 2D projection data, and a *voxel* is its 3D equivalent in image space. The number of pixels in a projection set can affect the system resolution and the projection data file size. If data are acquired

using pixels larger in size than the inherent spatial resolution of the collimator, the image resolution is degraded. However, the memory storage and the time required for image reconstruction is lower for projection sets with fewer pixels. Similarly, the matrix size (number of voxels) for a reconstructed image should be chosen to complement the inherent resolution of the camera (a function of the collimator, the source-to-detector distance, the projection pixel size, and the intrinsic resolution of the detector) and the question to be answered by imaging.

To form a 3D SPECT image, modern reconstruction methods use iterative algorithms. These assume an initial estimate of the 3D activity distribution in an object and iteratively update this estimate based on relative differences between mathematically synthesized projections (*forward-projections*) of the current image estimate and the measured projection set (Figure 1.3). The projection errors are translated back into image space (back-projection) and this error image is used to update to current image estimate [34]. The forward- and back-projections are facilitated by the use of a camera-specific *system matrix* which contains information required to translate between image and projection

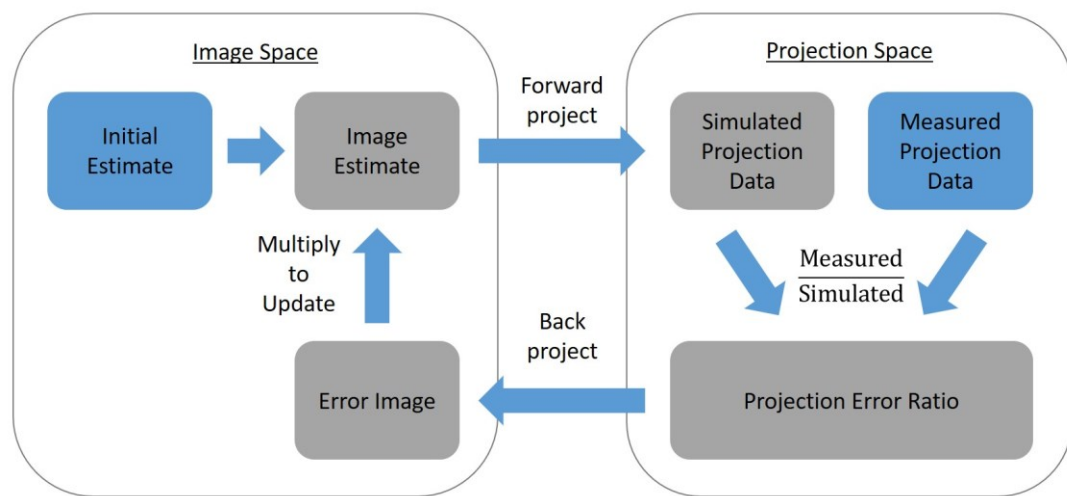


**Figure 1.3** General iterative reconstruction algorithm. The cycle is repeated for the desired number of iterations. Comparisons in projection space can be done for all projections as in standard iterative algorithms or for subsets of projections as in OSEM. The last updated image estimate is output as the reconstructed image.

space. With every iteration the estimated image converges slowly towards an image consistent with the true underlying activity distribution. However, since the algorithm also matches the noise in the calculated forward projection to the noise in the acquired projection, the noise in the reconstructed image increases the noise with an increasing number of iterations.

Ordered-subset expectation maximization (OSEM) is an iterative algorithm that divides all available projections into subsets to improve the speed of reconstruction by a factor approximately equal to the number of subsets. For example, 60 projections can be divided into 10 subsets each containing 6 projections. For each iteration, one subset of projections of the estimated image is compared with the corresponding subset of measured projections [11], [35].

Reconstructions of parallel-hole collimated SPECT projection data can be improved using *resolution recovery* (RR). RR includes a priori information about the collimator design and depth dependence of spatial resolution at each iteration of an OSEM algorithm to improve the spatial resolution and reduce the noise in a reconstructed image. Reconstructions including RR require additional memory and computing time since they include more information in the reconstruction and are slower to converge [35].

For pinhole cameras, all OSEM reconstructions include *collimator modelling* (CM) to account for depth-dependent spatial resolution, variable pinhole sensitivity, image magnification, and aperture penetration [7]. However, the additional mathematical terms included in OSEM with collimator modelling further amplifies noise which produces greater uncertainty and can produce hot spots in the reconstructed image [34].

Priors can be incorporated into the OSEM algorithm to suppress the image noise.

Maximum a posteriori (MAP) algorithms include a noise-suppressing regularization term at each iterative update. In the class of Gibbs priors, one regularization technique used by the Xeleris Myovation software (GE Healthcare, Haifa, Israel) employs a modified one-step late (OSL) Green prior [34], [36]. Within the MAP algorithm, the prior enforces an assumption of local smoothness in an image by penalizing voxel values that are dissimilar from their neighbours [7]. The algorithm has two competing objectives: (1) to converge to an image with simulated projection data that matches measured data, and (2) to have local smoothness. The prioritization of these objectives is controlled by parameters  $\beta$  and  $\delta$ . Ranging from 0 to 1,  $\beta$  is the weight assigned to enforce local smoothness in the image more than matching the projection data. The parameter  $\delta$  (or  $\alpha$  in Myovation ranging from 0 to 10) dictates the strength of the penalty for differences between the value of a given voxel and its neighbour [35].

Projection data may be reconstructed with or without information about photon attenuation in tissue. Non-corrected (NC) images will contain attenuation artifacts presenting as reduced apparent activity deeper inside of an object. CT-derived attenuation maps can be used to calculate the cumulative attenuation along each position-to-detector path in the SPECT image. This attenuation correction (AC) factor is then incorporated into the system matrix to increase the apparent signal in the estimated image. It should be noted that while attenuation correction returns uniformity to the image of an object with a homogeneous activity distribution, the underlying counts (number of detected photons) contributing to the image remain the same. As a result, the noise (see Section 2.3) in regions of the image with low photon sensitivity will be amplified by AC reconstruction.

Similarly, scatter correction (SC) methods may be used prior to reconstruction or

introduced into the reconstruction algorithm to further improve contrast and quantification accuracy of the reconstructed image [12]–[18]. Scatter correction also amplifies noise in the reconstructed image.

Low-pass post-reconstruction filtering such as with a three-dimensional Butterworth filter is commonly used to suppress high frequency noise in images [7]. High spatial frequencies correspond to detail in an image, so suppressing high frequencies and allowing low spatial frequencies to remain both suppresses noise and smooths the image. The Butterworth filter has two parameters; the cut-off frequency and the order. Reducing the cut-off frequency suppresses noise at lower spatial frequencies but also degrades spatial resolution due to blurring. Low-order filtering provides gradual smoothing over a range of spatial frequencies while high order filters approach a step function which includes all spatial frequencies below the cut-off frequency and none of those above [7]. To provide physicians with similar levels of smoothing for all patient MPI images, filter parameters are generally standardized within a clinic. For the purposes of this thesis, image filtering is not applied unless otherwise specified to avoid confounding the interpretations of spatial resolution and image noise measurements in Chapter 3 to Chapter 6.

## **1.8 Cardiac Image Evaluation**

### **1.8.1 Image Display**

In cardiac SPECT imaging, a clinician evaluates myocardial perfusion studies based on relative and/or quantitative changes in myocardial perfusion image intensity, and on changes in the shape and size of the left (LV) and right (RV) ventricles. Perfusion images are subjectively inspected, based on a physician's experience, for differences from a

normal perfusion pattern (similar activity concentration throughout the LV) and can also be quantitatively assessed based on relative differences within an image (percent of maximum myocardial uptake) or based on difference with respect to a normal database (Section 1.8.2). For the best results with any method of comparison, it is important that images are evaluated in a consistent orientation and that images are of similar quality.

Images are reconstructed in the reference frame of the SPECT camera. The axial z-direction normally coincides with the axis of rotation of a rotating camera. Prone and supine patient orientation has the head-to-toe length of the patient parallel with the axial direction in the camera reference frame. Two-dimensional slices of the image volume in the plane perpendicular to this axis are called *transaxial* or *transverse slices*. Example transaxial slices of reconstructed images are displayed in the camera reference frame in Figure 1.1.

For consistency, MPI images are reoriented [37] into the cardiac reference frame such that short axis (*SA*) slices correspond to planes stacked from apex to base of the left ventricle of the heart (Figure 1.4). The horizontal (*HLA*) and vertical (*VLA*) long axis views are perpendicular to the SA and correspond to planes displaying the septal/lateral walls and the anterior/inferior walls respectively. Images are displayed on a relative colour or gray scale which is normalized to the maximum perfusion in the myocardium. The shape and relative magnitude of the activity distribution is evaluated in these orientations to identify images artifacts and subtle changes in tracer uptake. Image *artifacts* are misrepresentations of the true tracer distribution in the reconstructed image. These errors can be introduced by patient motion (gross, respiratory, or cardiac), count starvation due to severe attenuation, misregistration of attenuation maps, camera design,

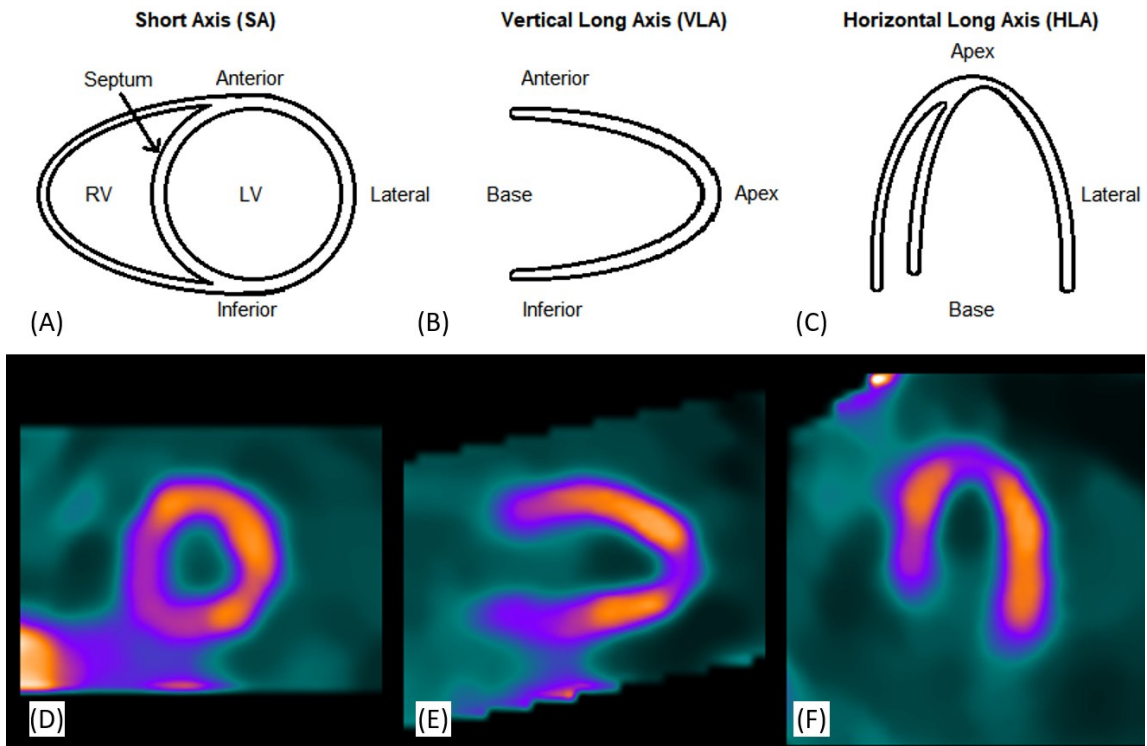
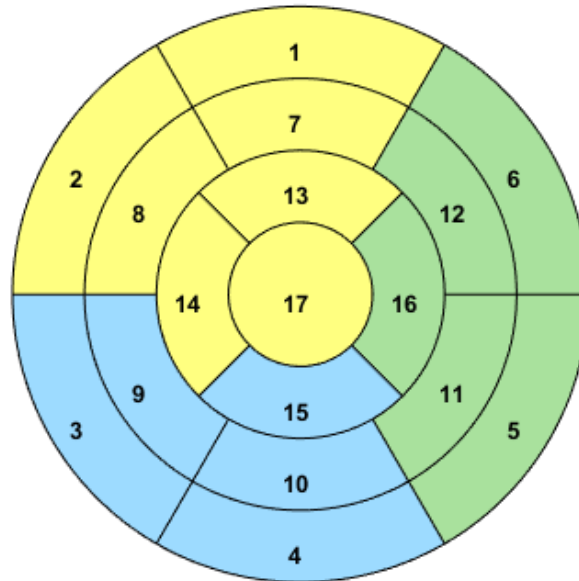


**Figure 1.4** Standard orientation for interpretation of myocardial perfusion of the left ventricle (LV) in the cardiac reference frame. The right ventricle (RV) is oriented to the left of the LV in the SA and HLA views.

the reconstruction algorithm, or other factors associated with the patient, the camera, or the image processing.

One strategy used by clinicians to differentiate between true hypoperfusion of myocardium and artifact is to evaluate the motion of the heart wall using *cardiac gated images* (as opposed to static images) [38]. To obtain cardiac gated images, the SPECT acquisition is synchronized to the cardiac cycle of a patient using electrocardiography (ECG). The period of one cardiac cycle is typically divided into 8 frames (*gates*) and SPECT data are binned into 8 projection sets according to the cardiac phase and summed over many cardiac cycles [11], [39]. All 8 projection sets are reconstructed and displayed cinematically in the order of the cardiac cycle in the SA, HLA, and VLA views (Figure 1.4). This gated image sequence provides physicians with information about LV wall



- |                       |                      |                    |
|-----------------------|----------------------|--------------------|
| 1 Basal anterior      | 7 Mid anterior       | 13 Apical anterior |
| 2 Basal anteroseptal  | 8 Mid anteroseptal   | 14 Apical septal   |
| 3 Basal inferoseptal  | 9 Mid inferoseptal   | 15 Apical inferior |
| 4 Basal inferior      | 10 Mid inferior      | 16 Apical lateral  |
| 5 Basal inferolateral | 11 Mid inferolateral | 17 Apex            |
| 6 Basal anterolateral | 12 Mid anterolateral |                    |

**Figure 1.5 Left ventricular 17-segment polar map delineation. Segment colours indicate the major arteries responsible for their perfusion: left anterior descending (yellow), right coronary artery (blue), or left circumflex (green).**

motion, wall thickness at different phases of the cardiac cycle, and estimates of cardiac ejection fraction [40]. If there is a perfusion defect in the static image but the wall motion is normal, the perceived defect may, for example, be attributed to an attenuation artifact [38].

Heart size and shape varies for different patients. To provide a global overview of LV tracer uptake and facilitate comparison of different patient static images on a pixel-by-pixel basis, a 3D static image is converted to a 2D cardiac *polar map* representation [41]–[43]. A polar map is displayed as a solid circle made up of concentric rings of values corresponding to the maximum uptake in the myocardium at each region in the LV; the outer ring and center correspond to the base and apex of the heart respectively. Values correspond at the top to the anterior, the bottom to the inferior, the left to the septum, and

right to the lateral wall of the heart. Polar maps allow physicians to quickly evaluate the distribution of myocardial perfusion in a single image. All polar maps used in this thesis were generated using subroutines from the FlowQuant v2.5 software package; pixelated polar maps are comprised of 24 rings each with 36 perfusion values and only the first 18-rings are displayed and evaluated (excluding the membranous septum and some of the lateral wall) [44], [45]. The polar maps can also be further divided into regions according to a 17-segment model polar map (Figure 1.5) [8]. With either polar map, interpatient comparison of absolute perfusion values is not helpful since even for normal patients there may be variability in the injected tracer activity, physiological differences between patients, and differences in attenuation. Thus, polar map values are normalized to maximum number of counts in an LV segment (or another metric) prior to comparison.

### **1.8.2 Normal Database**

Semi-quantitative analysis of MPI studies requires a normal comparator. Normalized polar map images from 20 to 40 patients at low-risk for cardiovascular disease and who have visually normal images are typically used to build a normal database specific to the imaging camera type, acquisition protocol, and patient gender [41]. The average and standard deviation [46] of the polar maps of all patients in the database are calculated to use as a normal reference for evaluating future patient images.

### **1.8.3 Detection and Quantification of Cardiac Hypoperfusion**

To quantitatively detect hypoperfusion in SPECT MPI, a patient's 17-segment polar map image is compared to the normal database specific to the study parameters. A z-score is calculated on a segment-by-segment basis as the difference between image segment value and the normal database mean segment value all divided by the normal

database segment standard deviation. The z-score map is translated using z-score thresholds onto a 5-point scale to evaluate the severity of hypoperfusion. Typical threshold values [47] assign a score of 0 (normal) to all segments less than 1.5 standard deviations from the normal database mean. A value of 1 (equivocal) when  $1.5 \leq z < 2.1$ , 2 (abnormal) for  $2.1 \leq z < 4$ , 3 (severe) for  $4 \leq z < 7$ , and 4 (absent uptake) for  $z \geq 7$ . Scores are summed to obtain a summed stress score (SSS) for a stress study and a summed rest score (SRS) for a rest study [42]. The difference SSS-SRS is called a summed difference score (SDS) and is used to estimate the amount of ischemia in rest/stress or stress/rest studies. An imaging study is concluded to be abnormal if the summed perfusion score is 4 or greater [48]. Highly abnormal studies are straightforward to detect, however studies of patients with mild disease are highly sensitive to the variability in the normal database. If the standard deviation of the normal data base is large, the sensitivity for detecting mild disease will be low. It is important that a normal database is specific to the testing conditions (camera, detectors, acquisition protocol, tracer, gender, etc.) [41].

## **1.9 Overview of the Thesis**

The success of myocardial perfusion imaging relies heavily on a physician's ability to clearly visualize regions of hypoperfusion in the myocardium. The spatial resolution of the SPECT camera and statistical noise in the MPI images impacts this ability. The positional variability of both photon sensitivity and resolution inherent to pinhole collimators employed by dedicated-cardiac cameras have the potential to alter the spatial resolution and noise in MPI images in ways that are not yet well understood. The goal of this thesis is to develop a better understanding of the impact of multi-pinhole designs on

the spatial resolution and noise of SPECT images. Additionally, I aim to use this knowledge to develop tools for standardizing image noise and aiding in image interpretation for these cameras.

Chapter 2 provides a review of existing theoretical and experimental methods for evaluating SPECT spatial resolution and image noise, some of which are recurrently used in the following chapters.

In Chapter 3, I test the hypothesis that spatial resolution changes with object position and orientation in the quality field-of-view of pinhole SPECT cameras. I calculate the relative spatial resolution for two-different multi-pinhole camera configurations to identify conditions that produce differences. I also use mathematical projections and OSEM reconstructions to demonstrate these resolution differences for images of a disk-shaped digital phantom at specific positions and orientations.

In Chapter 4, I develop a new method for estimating image noise for attenuation corrected reconstructed images from a multi-pinhole camera. The method is fast enough to be feasible for clinical use.

For appropriate testing and biological dose justification, SPECT imaging guidelines recommend using patient-specific imaging protocols. These include adjusting the injected radiotracer activity and image acquisition time to ensure detection of enough photons to achieve a diagnostic quality image. The optimization of patient-specific imaging protocols, however, has been previously based on a discrete measure of clinical interpretation or on a continuous measure of the number of photons detected in projection space. As discussed in Section 1.7, image reconstruction greatly influences the noise properties of an image. In Chapter 5, I develop a new model for developing patient-

specific imaging protocols using a continuous measure of image noise in reconstructed images.

In Chapter 6, I use the protocol developed in Chapter 5 to standardize the noise in patient images and I reveal the presence of a large spatial gradient in image noise over the length of the heart. Higher noise at the base of the heart may make it more difficult for physicians to identify true abnormalities. This emphasizes the need for including noise information in clinical protocol design and imaging analysis.

A summary of the thesis along with suggestions for future avenues of investigation and development are presented in Chapter 7.

## **Chapter 2: Review of Spatial Resolution and Image Noise**

*A review of measures of and methods for evaluating spatial resolution and image noise in SPECT cameras employing pinhole and parallel-hole collimators.*

*A portion of Section 2.3 has been previously published in a modified format. © 2018 Wiley. Reprinted, with permission, from Cuddy-Walsh, S. G. and Wells, R. G. “Patient-specific estimation of spatially-variant image noise for a pinhole cardiac SPECT camera” *Medical Physics*, 2018;45(5):2033-2047.*

## 2.1 Overview

To provide a foundation for the work reported in this thesis, this chapter serves to define spatial resolution and image noise in the context of SPECT imaging. It also reviews common approaches for their measurement in parallel-hole and pinhole cameras.

## 2.2 Spatial Resolution

*Spatial resolution* refers to the ability of an imaging system to resolve two individual objects. It is an important feature of image quality particularly for tasks which need to identify small features in an image. In SPECT imaging, partial volume effects (Section 2.2.2) resulting from limited spatial resolution can also reduce the accuracy of quantitative measurements of radiotracer perfusion which may have an impact on clinical decisions. While all discussion of spatial resolution in this thesis assumes the objects being imaged are static, it should be noted that patient motion due to respiration, cardiac motion, or body movement also cause image blurring [49]–[53].

### 2.2.1 Measures of Resolution

Spatial resolution is often described as a measure of the smallest separation for which two objects can be resolved or as the diameter of the smallest resolvable object. It is commonly characterized using profiles of image intensity (counts) as functions of position in the spatial domain. A line spread function (LSF) and point spread function (PSF) are profiles across an image of a line and a point source respectively [7]. A measure of spatial resolution is given by the full-width at the half-maximum (FWHM) of the LSF or PSF [54]. To obtain the spatial resolution in multiple dimensions, the PSF can be measured using the FWHM of profiles in each spatial dimension  $x$ ,  $y$ , and  $z$  for a point source of known size [54]. The 3D image ( $I$ ) of an object imaged with a SPECT

camera is mathematically related to the object by a convolution (\*) of the voxelized object with the PSF:  $I(x, y, z) = O(x, y, z) * PSF(x, y, z)$ . A drawback to both the PSF and LSF however is that they measure spatial resolution without information about image contrast conditions. As a result, two camera designs could have the same resolution but drastically difference performance at a task like lesion detection [35].

The modulation transfer function (MTF) includes spatial frequency information to allow more complete characterization of the camera. Given mathematically by the Fourier transform of the PSF, the MTF describes the spatial frequencies  $k_x$ ,  $k_y$ , and  $k_z$  measured in lines/mm which correspond to image spatial dimensions  $x$ ,  $y$ , and  $z$  [54]. Fine detail and sharp edges in an image in the spatial domain require good system performance at high frequencies in the frequency domain. Coarse detail in an image corresponds to low spatial frequencies [7]. Constant MTF for all spatial frequencies or delta function PSF means that the system can best reproduce the object in an image.

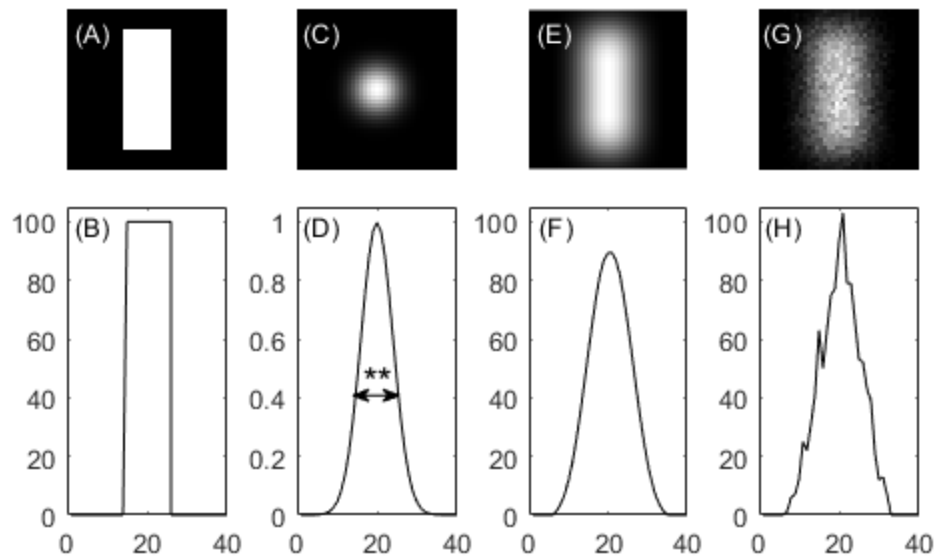


**Figure 2.1** (A) Image of a 2D object and (B) horizontal profile through the object. (C) Point spread function (PSF) and (D) line spread function (LSF) of imaging system where \*\* indicates the full-width at half-maximum resolution. (E) Image of the object in (A) blurred by convolution with (C). The profile of (B) convolved with (D) is given in (F). Adding Poisson noise results in the image in (G) and profile in (H).

Increasing a camera's performance at high spatial frequencies will increase its ability to resolve small objects [54]. Since the abstract nature of MTF makes it difficult for comparing the performance of different imaging systems, FWHM of the PSF or LSF is typically used to describe spatial resolution.

Measurements of spatial resolution are often accomplished in SPECT using a point source in air or a Jaszczak phantom [29], [35], [55]. The Jaszczak phantom consists of a cylinder filled with isotope-water mixture with cold spheres and rods at different positions. The spheres all differ in size and the diameter of the smallest sphere that is resolvable by an imaging system is indicative of the system's spatial resolution. If one wishes to evaluate spatial resolution in a specific direction in the FOV, a Defrise disk phantom [55] may be imaged. It consists of a cylindrical phantom with several cold disks interspaced with liquid radiotracer activity. The disk thickness is equal to the space between disks. The disk phantom can be used to evaluate spatial resolution in the direction perpendicular to the plane of the disks due to axial sampling completeness of camera designs [29]. As an example, if the disks are aligned parallel to the transverse plane, an image intensity profile along the normal to the disks can be used to evaluate the uniformity of the axial spatial resolution. It is recommended to select the disk spacing/thickness to be on the same order as the expected spatial resolution of the camera.

### **2.2.2 Partial Volume Effect**

Partial volume effects (PVE) can significantly impact the ability of an imaging system to identify small structures and to obtain accurate quantitative information [7]. Two different mechanisms influence PVE. First, blurring due to finite spatial resolution may

result in the activity from an object at one voxel position mixing into neighbouring voxels in an image. PVE can cause the image of the liver to appear larger and less intense with counts from the liver spilling over into the heart [7], [56]. Secondly, PVE is caused by the fractional tissue contributions such that the activity detected from objects smaller than 2-3 times the image voxel size (or spatial resolution if voxels are small) contribute counts to only part of a voxel [7], [35]. The apparent concentration of the activity is reduced due to dilution throughout the voxel volume. The thickness of the myocardial wall is 7-12 mm [57] and the voxel sizes of the DNM530c and Infinia cameras are typically 4 mm and 6.797 mm. Thus, the intensity of the myocardium can depend on its size, shape, and activity concentration. Overall, PVE leads to reduced image contrast and limits the detectability of disease [58]. This emphasizes the need for a system resolution and voxel size of the same order or better than the size of the objects of interest.

### **2.2.3 Parallel-hole and Pinhole Data Sufficiency Requirements**

As described in Sections 1.6.1 and 1.6.3, collimator type and positioning of collimator-detector heads have a large impact on the performance of SPECT imaging. With parallel-hole collimators, the hole diameter and length are the primary parameters affecting the spatial resolution of a standard gamma camera. Another key factor for parallel-hole SPECT imaging resolution is the radius of rotation (the distance of the detector to the center of the gantry rotation). For cameras employing pinhole collimation, image resolution depends primarily on the size of the detector elements (or resolution of the detector) behind the pinhole, the distance of the object from the pinhole, and pinhole aperture blurring. Object-to-pinhole distance-dependent magnification or minification means that the resolution of an imaging system is variable within the FOV [29].

To resolve objects in three dimensions, multiple views of the object are required. An imaging system is considered *shift-invariant* if projection data of a shifted object are equal to the shifted projection data of an unshifted object. If shifting the object produces other changes in the result, the system is considered *shift-variant* [11].

Rotating parallel-hole cameras are designed to be shift-invariant as long as distance-dependent resolution changes are ignored or corrected. The sensitivity and resolution for an object is the same for two different parallel hole views and remains so if the object is shifted. Sampling requirements for reconstructing a 3D image from parallel-hole projection data are described by Orlov's completeness model. This requires that the path of sampling locations and angles of detectors must "have points in common with any arc of a great circle [59]."

For pinhole collimators, photon sensitivity inherently varies with the position (angle, distance) of the object relative to the pinhole and 2D spatial resolution varies with the distance between the pinhole and object. Additionally, the limited number of pinholes typically comprising pinhole cameras such as the DNM530c means that obtaining a 2D view of every angle of an object is not possible. As such, pinhole cameras are always shift-variant systems and evaluating resolution in a pinhole SPECT system is much more complex than for a parallel-hole camera. In order to successfully reconstruct a three-dimensional object, Tuy's principles for cone-beam or pinhole collimation require all reconstructed planes that intersect an object to have at least one pinhole (focal) point [60]. Additionally, the path of pinhole-detectors must be outside of the region of interest and be bounded and continuous [61]. The underlying idea for both sets of conditions being that, unless at least one view of the objects was acquired at a position and angle

allowing them to be resolved in that 2D view, the system will not be able to resolve two objects in 3D even with perfect intrinsic resolution of the collimator-detector.

In practice, sampling with SPECT systems is not continuous along the path or curve of detectors. Rotating systems commonly acquire data using a step-and-shoot technique with an angular step size of  $2^{\circ}$ – $6^{\circ}$  and stationary multiple pinhole systems have even larger angular spacing between pinhole-detectors [29]. To satisfy the Nyquist-Shannon sampling theorem, a sampling period of half or less of the target spatial resolution for the SPECT system is needed. Since individual pinhole-detectors each sample a range of angles, the requirement for the number of pinhole-detector angles is relaxed compared to for parallel-hole systems. It does however remain difficult to achieve angular sampling sufficient to avoid non-uniformities in the FOV of pinhole SPECT cameras. If a plane exists through an object that cannot be seen by a pinhole detector, the resolution is degraded for that object in that direction. This concept is investigated in Chapter 3.

### **2.3 Image Noise**

Both the magnitude and the texture of noise are known to influence the detectability of disease in images [62]. In cardiac imaging, physicians employ strategies such as evaluating wall motion with electrocardiogram-gated image sequences to try to determine if an apparent defect is real, artifact, or noise. Current clinical SPECT imaging software does not provide any information about the level or distribution of noise in an image. Instead, noise is inferred by comparing mean values of pixels in assumed homogeneous regions (spatial variance). For example, noise is estimated by comparing pixel values within the normal myocardium. However, as it is variations in pixel values within the myocardium which are of interest, this approach can be problematic.

The magnitude of image noise is typically defined by one of three metrics [63]:

1. Spatial variance: variance of voxel values within a homogeneous region of interest (ROI) of a single reconstructed image.
2. Ensemble variance: variance of the mean signal values within in an ROI, measured over  $N$  image noise realizations.
3. Ensemble voxel variance ( $\sigma_v^2$ ): variance of the signal values  $F_v^n$  for each voxel  $v$  and noise realization  $n$  over  $N$  image noise realizations (Equation 5).

$$\sigma_v^2 = \frac{1}{N-1} \sum_{n=1}^N (F_v^n - \bar{F}_v)^2 \quad (5)$$

$$\bar{F}_v = \frac{1}{N} \sum_{n=1}^N F_v^n \quad (6)$$

Throughout this thesis, all references to noise, image noise, or noise magnitude are defined as the uncertainty  $\sigma_v$  as given by the square root of the ensemble voxel variance of an individual reconstructed voxel value (Equation 5).

The texture of image noise also influences the detectability of disease, it is however much more difficult to measure and quantify than the magnitude. One metric for quantifying noise texture is known as the noise correlation length. This is a measure of the distance at which the value of one voxel is no longer related to the value of its neighbours. For one voxel at position  $v_i$  the covariance is calculated relative to a neighbouring voxel  $v_j$  using  $N$  statistically different reconstructed images.

$$COV(v_i, v_j) = \frac{1}{N} \sum_{n=1}^N (F_{v_i}^n - \bar{F}_{v_i}) (F_{v_j}^n - \bar{F}_{v_j}) \quad (7)$$

A covariance image can be formed by repeating this for all voxel positions. Assuming an approximately Gaussian distribution of covariance measurements about  $v_i$ , its

correlation length can be defined as the radial distance from the voxel at which the average covariance falls to half of its variance [64]. To provide information about the texture of image noise, a map of correlation lengths is thus generated by calculating the correlation length for all voxels in an image or region of interest. Longer correlation lengths are indicative of greater noise texture in an image which may negatively influence the detectability of disease.

### **2.3.1 Contributing Factors**

The largest contributor to SPECT image noise is the quantity of detected photons used to create an image. Photon emission via radioactive decay is a stochastic process and as such the number of photons counted by a detector follows a Poisson distribution. If the number of photons counted in a detector pixel is  $Q$ , the uncertainty in the number of photons is simply the square root of  $Q$ . The fractional noise is simply  $\frac{1}{\sqrt{Q}}$ . Electronics noise associated with detectors and readout electronics become important at very high-count levels. However, Poisson counting statistics are the dominant contributor to image noise for clinically relevant acquisitions. Under clinical imaging conditions, fractional noise can be reduced by increasing the number of counts acquired in the projection data. This in turn is achieved by acquiring with higher radiotracer activities or for longer acquisition durations [65]. Reconstruction of 2D projection sets into a 3D image propagates and augments the noise in a non-trivial manner. While still linked to the number of contributing photons, the magnitude and texture of the noise in reconstructed images is highly dependent upon the reconstruction algorithm, strength of regularization priors, scatter correction, attenuation correction, and filtering.

## **2.3.2 Influence of Body Habitus and Camera Design**

### **Attenuation and Body Habitus**

As discussed in Section 1.5, photons originating from the myocardial tissue of a patient (cardiac photons) are attenuated by body tissue prior to detection by the camera. Attenuation reduces the number of cardiac photons that are detected in the photopeak energy window. The probability of a photon being attenuated depends on the type and thickness of the tissue that the photon is traversing. Thus, assuming approximately homogenous tissue types (ignoring the lungs) fewer photons originating from the base of the heart (deepest in a supine patient) are detected compared with those originating from the apex of the heart (closest to the surface). This contributes to a gradient in the number of photons detected over the length of the heart. Additionally, large patients with more (thicker) body tissue than small patients, will have less photons detected overall when both patients are administered the same cardiac radiotracer activity.

### **Collimator Sensitivity and Number of Detectors**

In addition to attenuation, the overall sensitivity of a SPECT camera will determine the number of photons detected from a source at a given position. It is influenced by the collimator type, detector size, and number of detectors. For parallel-hole collimated cameras, the sensitivity is almost independent of object-to-detector distance, as long as the image of the object does not extend beyond the edges of the detector, and thus is constant for all positions within the quality FOV. For pinhole camera designs [33] however, the detector-pinhole sensitivity changes with distance from each pinhole aperture (Section 1.6) and the overall camera sensitivity depends on the distance of an

object from all apertures. The system sensitivity is additive, such that it may be lower for positions not seen by all detectors (outside the quality FOV) than for positions inside the QFOV. In the case of the DNM530c, even though the heart is positioned inside the QFOV, the positioning of the pinholes above and to the right of the FOV leads to a gradient in the number of photons contributing to an image across the length of the heart (from bottom-left to top-right in the QFOV) [33], [66].

### **Spatially variable noise**

Since noise is largely governed by Poisson counting statistics, the effects of attenuation and camera sensitivity on the number of detected photons will influence the level of local noise SPECT images. First, cameras with lower geometric sensitivities will have higher noise overall than more efficient cameras. Second, large patients will have more noisy images than small patients given the same radiotracer activity. Third, assuming a homogenous activity distribution, source locations deepest in the patient (for parallel hole and pinhole cameras) and farthest from the detectors (for pinhole cameras only) will contribute fewer photons and thus have higher image noise than those close to the surface of the patient and close to camera detectors. Thus, I expect in Chapter 4 and Chapter 6 to observe a noise gradient in the field of view of both parallel hole and pinhole cameras. The gradient is expected to be larger for the pinhole camera design due to the added variability of collimator geometric sensitivity.

### **2.3.3 Patient-Specific Imaging Protocols**

The widely known impact of body habitus on image noise and image quality previously led clinics to increase tracer activity or imaging times for large patients (greater than 70 kg) to ensure diagnostic quality images were acquired. Recent pushes for

patient-specific medicine and “Image Wisely” dose reduction movements [67], [68] have encouraged the clinicians to further update MPI SPECT guidelines to recommend patient and camera-specific imaging protocols for all patients [8]. This action helps to standardize image quality for all patients by using increased administered activity or longer acquisition time to record more counts in heavy patients. Additionally, it strives to keep biologically effective doses to patients as low as diagnostically achievable. Methods for determining the administered radiotracer activity often referred to as *injected dose*, rely primarily on the quantity of photons (counts) detected in regions of interest about the heart in the projection data [69]–[75]. The detected count level in an image is expressed as a function of a chosen body habitus parameter such as body mass (weight), body mass index (BMI), chest circumference, mass per length, or percentage body fat. The weight and BMI parameters that are commonly used clinically have been shown to correlate with the number of detected counts. For the DNM530c, van Dijk et al recommend administering an activity [MBq] of  $A_{admin} = 19 \cdot W^{1.05} / T_{scan}$  for a specific patient body mass  $W$  [kg] and acquisition duration  $T_{scan}$  [min] to achieve image quality for all patients that is similar to a 80-kg patient with  $A = 380$  MBq and  $T_{scan} = 5$  min [70]. They simplify this to a linear relationship of  $A_{admin} = 23.8 \cdot W / T_{scan}$  for ease of clinical use [70]. For a conventional gamma camera, they similarly recommend administering an activity of  $A_{admin} = 223 \cdot W^{0.65} / T_{scan}$  ( $T_{scan}$  = time per head position). Another group shows an administered dose of 2.5 MBq/kg provides equivalent image quality for patients imaged for 475 seconds with the DNM530c or 25 seconds per head position (60 positions) with a standard gamma camera [73].

In each of these studies, image quality was subjectively evaluated with a 4-point scale

(1-poor, 2-fair, 3-good, and 4-excellent) by nuclear medicine physicians to ensure that developed protocols would produce diagnostic quality images. The average and range of visual scores for groups with and without patient-specific protocols were compared to detect a difference. The same visual grading approach was used with different time-adjusted count levels to determine the minimum-dose protocol for imaging with the DNM530c:  $A_{admin} = 18 \cdot W / T_{scan}$  [69]. While these groups evaluate the correlation between imaging protocol, patient weight, and acquired counts. The evaluation of reconstructed image quality is entirely subjective based upon personal experience. No comparison is made for different reconstruction techniques and how they may influence the noise and quality of the image.

#### **2.3.4 Noise Estimation Methods**

The most straight-forward method for determining an image of the noise magnitude (Equation 5) and texture (Equation 7) for a SPECT study is to obtain a large number ( $N$ ) of repeated acquisitions. However, the time required for acquisition and reconstruction of these images, dose limitations due to decay over long acquisition times, patient comfort, and the increased likelihood of introducing patient motion between trials all detract from the feasibility of this approach.

An alternative approach is to use a bootstrapping technique to determine image noise from few or a single SPECT acquisition [1]. The non-parametric bootstrapping technique sub-divides the list-mode projection data into  $M$  times segments. To create a “bootstrap” or new noise realization data set, the  $M$  projection sub-subsets are each sampled  $M$  times with replacement for each of the projection angles separately for a total of  $(M) \times (\# \text{ of projections})$  random samples. Each bootstrap is reconstructed as the imaging protocol

dictates. The process is repeated to obtain the desired number  $N$  of bootstrap replicates. The uncertainty in the noise estimate is reduced with more replicates, but the number of bootstrap replicates typically used is  $N > 200$  [1]. A comparison of noise values is shown for different  $N$  in Appendix B. The noise magnitude and texture are calculated using Equations 5 and 7.

When list-mode projection data are unavailable, it is possible to use Poisson resampling techniques to create bootstrap-like projection sets [2]. To use this method, the number of counts in each pixel of the original projection data set is assumed to be the mean of a Poisson distribution. To generate a bootstrap, the value in each pixel is replaced by a random number drawn from a Poisson distribution about its mean. These pseudo-bootstraps can be reconstructed, and image noise calculated in the same manner as with non-parametric bootstrapping. This method is similar to Monte Carlo simulation techniques [64] which are generally used to simulate noise from noise-free projection data. The large number  $N$  of reconstructions required to provide an accurate noise estimates using bootstrapping or Monte Carlo methods restricts its use to research applications due to clinical throughput limitations.

Analytical calculation of noise is not applicable for iterative reconstruction techniques such as OSEM and MAP-EM. Instead, some groups have taken the approach of estimating the ensemble voxel variance by propagating noise through the reconstruction algorithm [1], [62], [76], [77]. These methods iteratively reconstruct the ensemble voxel variance in a similar manner to the image itself, effectively doubling the reconstruction time. To do so, the algorithms require knowledge of system specifications, reconstruction parameters including information about the implementation of priors, and information

about the underlying mean image. For noise-free phantom studies, they are reported to produce excellent estimates of noise and its texture [63]. However, there have been no studies to date evaluating their accuracy for noisy clinical data. It also remains necessary to integrate the noise reconstruction within the sometimes-proprietary vendor reconstruction software which may limit implementation. A novel method for rapidly calculating the magnitude in a pinhole SPECT image is developed in Chapter 4 and is validated against noise determined using pseudo-bootstrapping as a gold-standard.

## **Chapter 3: Directional resolution of limited-angle multi-pinhole SPECT cameras**

*This chapter demonstrates the influence of object position and orientation on spatial resolution in pinhole SPECT camera designs.*

*This chapter has been previously published in a conference record. © 2014 IEEE. Reprinted, with permission, from Cuddy-Walsh, S. G., Clackdoyle, R., Wells, R. G., “Directional resolution of limited-angle multi-pinhole SPECT cameras,” 2014 IEEE Nuclear Science Symposium and Medical Imaging Conference Record (NSS/MIC), November 2014. Minor reformatting modifications have been made.*

### 3.1 Introduction

The popularity of small-animal and more recently clinical SPECT cameras like the Discovery NM530c (GE Healthcare) which are based on multi-pinhole detector arrangements have renewed interest in the variability of the local imaging capability within the FOV of these cameras. Shift-invariance, familiar from classical rotating gamma cameras with parallel-hole collimators, is lost for such pinhole cameras and each point in the FOV has a different tomographic response function. Locally, the pattern of tomographic completeness varies. Metzler *et al.* [60], [78] used a local Orlov completeness model to quantify this variability and validated it using ordered subset expectation maximization (OSEM) reconstructions of small disk phantoms. The visual effect of local tomographic incompleteness is increased image blur, suggesting a loss of resolution capability. However, the effect is not isotropic, and they did not evaluate the impact on resolution of the orientation of an object relative to the pinhole(s). In earlier work by Clackdoyle and Noo [79]–[81] the directional behavior of this resolution loss was quantified with a different metric that took into account the direction of tomographic incompleteness, but the model was only tested using a heuristic analytic reconstruction. Here I will adopt the directional resolution model from Noo and Clackdoyle [79] (and I use the word "resolution" in this tomographic sense, assuming ideal physical conditions: perfect detector resolution, ideal point pinhole, noise-free projection data, no attenuation, no scatter, and no pinhole edge penetration) to probe for differences in resolution dependent upon the position of the source and the orientation of the resolution measurement about the source. Our hypothesis is that limited numbers of pinhole views puts restrictions on the best angle at which an object may be viewed and thus introduces a

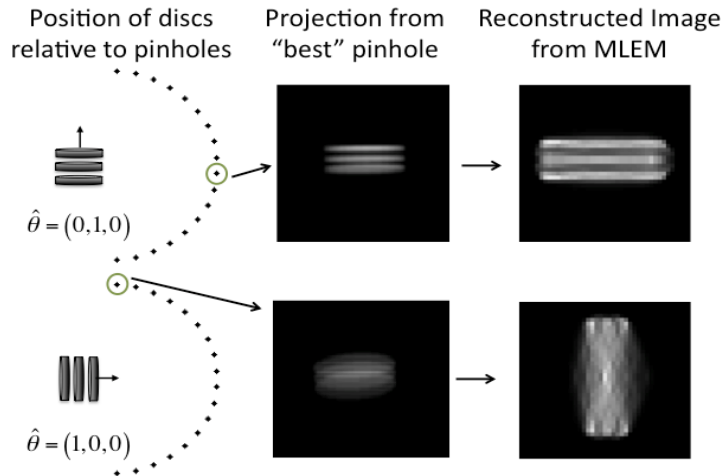


**Figure 3.1** Example of the effects of orientation in a pinhole- based SPECT camera with a limited number of angles. Three disks oriented parallel with the x-axis are reconstructed well since the “best” pinhole projection can see the spaces between the disks. When oriented perpendicular to this, the slight shift to the left causes the “best” pinhole to be unable to see the gaps and thus the reconstructed images are much more blurred.

position and orientation dependence to the resolution of the camera (Figure 3.1) despite nominally having adequate information to do a reconstruction. I validate the model using simulations of disk phantoms with maximum likelihood expectation maximization (MLEM) reconstructions. Iterative methods like MLEM are preferable to an ad hoc analytic method because they tend to converge to a reasonable solution if one exists [82].

## 3.2 Methods

### 3.2.1 Camera Configurations

I modeled two different camera configurations as depicted in the top row of Figure 3.2. The first, the circular configuration, was composed of a complete  $360^\circ$  sampling using 36 pinholes spaced evenly by  $10^\circ$ . The second, the rectangular arc configuration, was composed of two arcs. Each arc had 16 equally spaced pinholes covering  $150^\circ$ . The two arcs were separated by 18 mm and connected by 2 pinholes on each end (6 mm separation) for a total of 36 pinholes. The axes of rotation of the pinhole cones in both configurations were perpendicular to and focused toward the Z-axis. The distance from

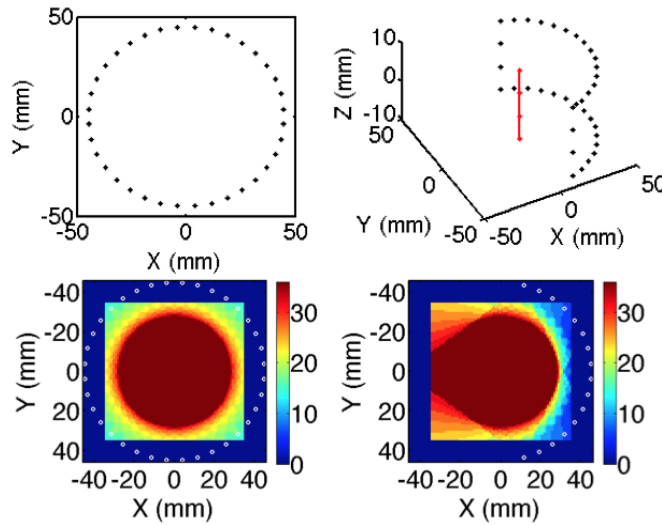


**Figure 3.2** Pinhole positions are plotted for a SPECT camera with circular sampling over  $360^\circ$  and rectangular arc sampling over  $150^\circ$ . Both designs contain 36 pinholes. The total number of pinholes for which the detector behind the pinhole can see each position  $(x,y)$  on the  $Z = 0$  mm plane are displayed using a colour scale with pinhole positions overlaid with white circles. Positions visible through all pinholes (dark red) define the FOV.

the Z-axis to the pinhole was 45 mm and the focal length (the perpendicular distance from the pinhole to the detector plane) was 132mm. The acceptance angle (Figure 1.2D)  $\alpha$  was  $90^\circ$  and the detector dimensions were 215mm $\times$ 215mm.

### 3.2.2 Mapping Pinhole Visibility

Ray tracing was used to create a binary image of positions that could be imaged by the detector behind each pinhole (assumed to be ideal). A value of 1 was assigned to a visible voxel position and 0 to a non-visible voxel position for each pinhole. By summing the binary images of all 36 pinholes, pinhole visibility images were created with color values representative of the number of pinholes that could see a given voxel position.

### 3.2.3 Theoretical Calculation of Resolution in the FOV

The angle  $\psi_i$  between the plane perpendicular to the normal of an object ( $\hat{\theta}$ ) and a vector defining the position of an object  $\vec{x}$  relative to each pinhole position  $\vec{a}_i$  is calculated for all pinholes numbered by  $i$ . (If the object is a point source,  $90^\circ - \psi_i$  is the

angle between the line along which resolution is being estimated and the vector from  $\vec{x}$  to  $\vec{a}_i$ .)

$$\sin \psi_i = \frac{|(\vec{a}_i - \vec{x}) \cdot \hat{\theta}|}{\|\vec{a}_i - \vec{x}\|} \quad (8)$$

The minimum angle for all pinholes  $i$  provides an estimate of the relative resolution  $R(\vec{x}, \hat{\theta})$  using Equation 9 for an idealized pinhole and detector without the effects of pinhole magnification. The best (smallest) resolution will occur when  $\hat{\theta}$  is perpendicular to the object-to-pinhole vector for at least one pinhole such that  $\psi_i = 0$ . The value  $k$  is an arbitrary scaling factor.

$$R(\vec{x}, \hat{\theta}) = k \cdot \min(\tan \psi_i) \quad (9)$$

Given knowledge of the resolution measured along a line through a point source in at least two directions or for at least 2 source positions, I could estimate a value for  $k$ . As previously noted, however the estimation of  $R(\vec{x}, \hat{\theta})$  assumes perfect detector resolution, ideal point pinhole, noise-free projection data, no attenuation, no scatter, and no pinhole edge penetration such that  $R(\vec{x}, \hat{\theta})$  can be equal to zero while this is not possible experimentally. Thus, for a more complete estimate of  $k$ , I might include the resolution contributions calculated using Equation 4 and the intrinsic resolution of the detector as in

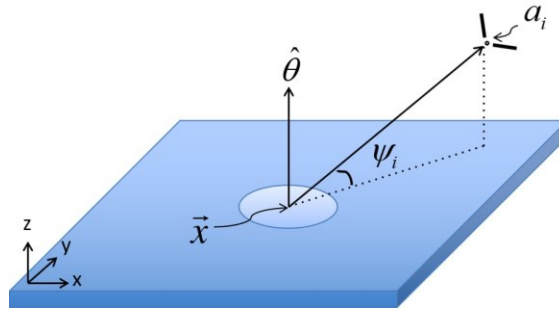


**Figure 3.3** Schematic depicting the coordinate and vector system used in Equation 9 to calculate the relative resolution  $R(\vec{x}, \hat{\theta})$  for an object such as a disk at a position,  $\vec{x}$ , relative to another position,  $\vec{x}_j$ . The angle between the line drawn between the plane orthogonal to the direction of resolution measurement ( $\hat{\theta}$ ) and the line drawn from the object to the position of the  $i^{\text{th}}$  pinhole is  $\psi_i$ .

Equation 10.

$$R_{measured} \approx \sqrt{(R_{intrinsic})^2 + \left(\frac{(a+b)d_e}{a}\right)^2 + (k \cdot \min(\tan \psi_i))^2} \quad (10)$$

For our theoretical calculations, the relative resolution was calculated using Equation 9 and  $k = 10 \text{ mm}$ . I calculated the angle between the normal to a given object plane with the vector from that plane to each pinhole in a camera design. The pinhole with the smallest angle, and thus the best view, was termed the “best pinhole” and the tangent of this angle was proportional to the relative resolution of the camera at that position and for that orientation. The relative resolution is reported

### 3.2.4 Resolution from Simulated Disk Phantom

Noise-free forward projections and reconstructions of a 3-disk computer phantom were simulated for the rectangular arc camera. The phantom had 0.75 mm thick disks with a radius of 5.75 mm and a 1.5 mm center-to-center spacing. The phantom was shifted:

in the positive X-direction [mm]

$$(-25,0,0) \rightarrow (-15,0,0) \rightarrow (-5,0,0) \rightarrow (5,0,0) \rightarrow (10,0,0) \rightarrow (20,0,0) \rightarrow (25,0,0)$$

or in the negative Y-direction [mm]

$$(23,0,0) \rightarrow (23,-4,0) \rightarrow (23,-8,0) \rightarrow (23,-11,0) \rightarrow (23,-15,0) \rightarrow (23,-19,0)$$

to position the disks in the high and low relative resolution locations determined by results from Figure 3.4. These positions are represented with white dots in Figure 3.5.

The disks were oriented with the  $\hat{\theta} = (1,0,0)$  or  $\hat{\theta} = (0,1,0)$ . Forward projections and reconstructions were done with an idealized pinhole and no attenuation, scatter, or pinhole edge penetration. Modeled pinholes were radially 45 mm from the Z-axis and the

focal length was 132mm. The detector array was  $256 \times 256$  with  $0.84 \text{ mm} \times 0.84 \text{ mm}$  pixels and the reconstructed array was  $128 \times 128 \times 128$  with 0.375 mm-cubed voxels. Forty iterations of MLEM were used for reconstruction.

### 3.3 Results

#### 3.3.1 Mapping Pinhole Visibility

The pinhole visibility maps for the X-Y plane at  $Z = 0 \text{ mm}$  are shown in the bottom row of Figure 3.2 for the circular and rectangular arc configurations. The white dots represent the pinhole locations. The dark red voxels in the images are visible by detectors behind all of the 36 pinholes in each configuration. I refer to this dark red region as the FOV. All future calculations are limited to investigating the resolution effects in the  $Z = 0 \text{ mm}$  plane of this fully supported FOV region.

#### 3.3.2 Theoretical Calculation of Resolution in the FOV

The results of calculating the relative resolution,  $R(\vec{x}, \hat{\theta})$ , for the circular and rectangular arc configurations (Figure 3.2) are shown in Figure 3.4 where small  $R(\vec{x}, \hat{\theta})$  values are predictors of good resolution. For the circular configuration,  $R(\vec{x}, \hat{\theta})$  has the same pattern (only rotated) for all  $\theta$  with a maximum value of 0.08. Voxels directly in line with the pinholes have lower  $R(\vec{x}, \hat{\theta})$  values (better predicted resolution) compared with those between pinholes. For the rectangular arc configuration, the pattern of  $R(\vec{x}, \hat{\theta})$  is similar (maximum of 0.18) to that of the circular configuration for all orientations shown in Figure 3.4 other than where the normal to the disks is in the X-direction. This is not an abrupt change however. In fact, if images were displayed for  $\hat{\theta}$  values between  $(-1/\sqrt{2}, 1/\sqrt{2}, 0)$  and  $(1,0,0)$ , the relative resolution would gradually worsen (increase) as the orientation approached  $(1,0,0)$ . It is in this orientation,

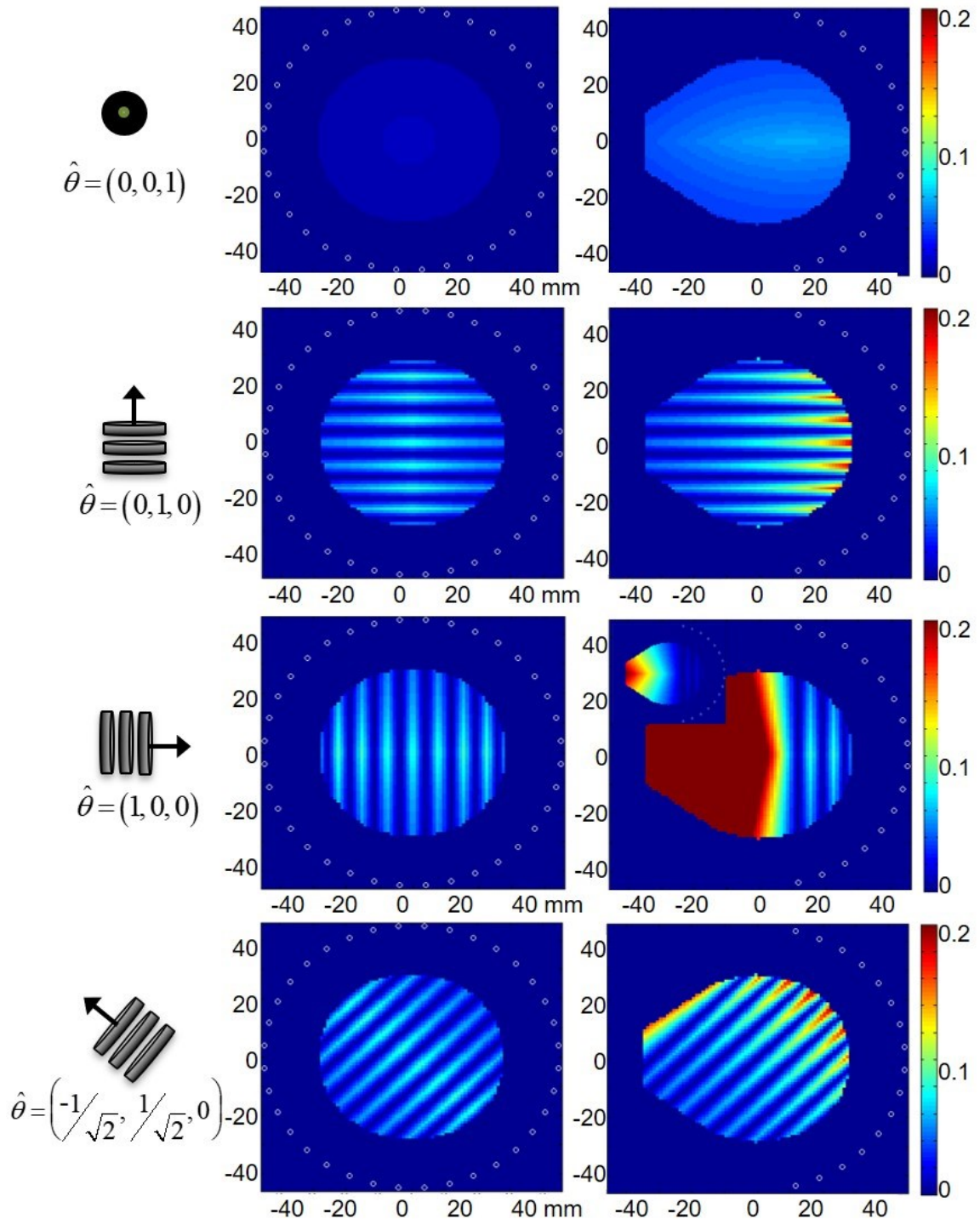
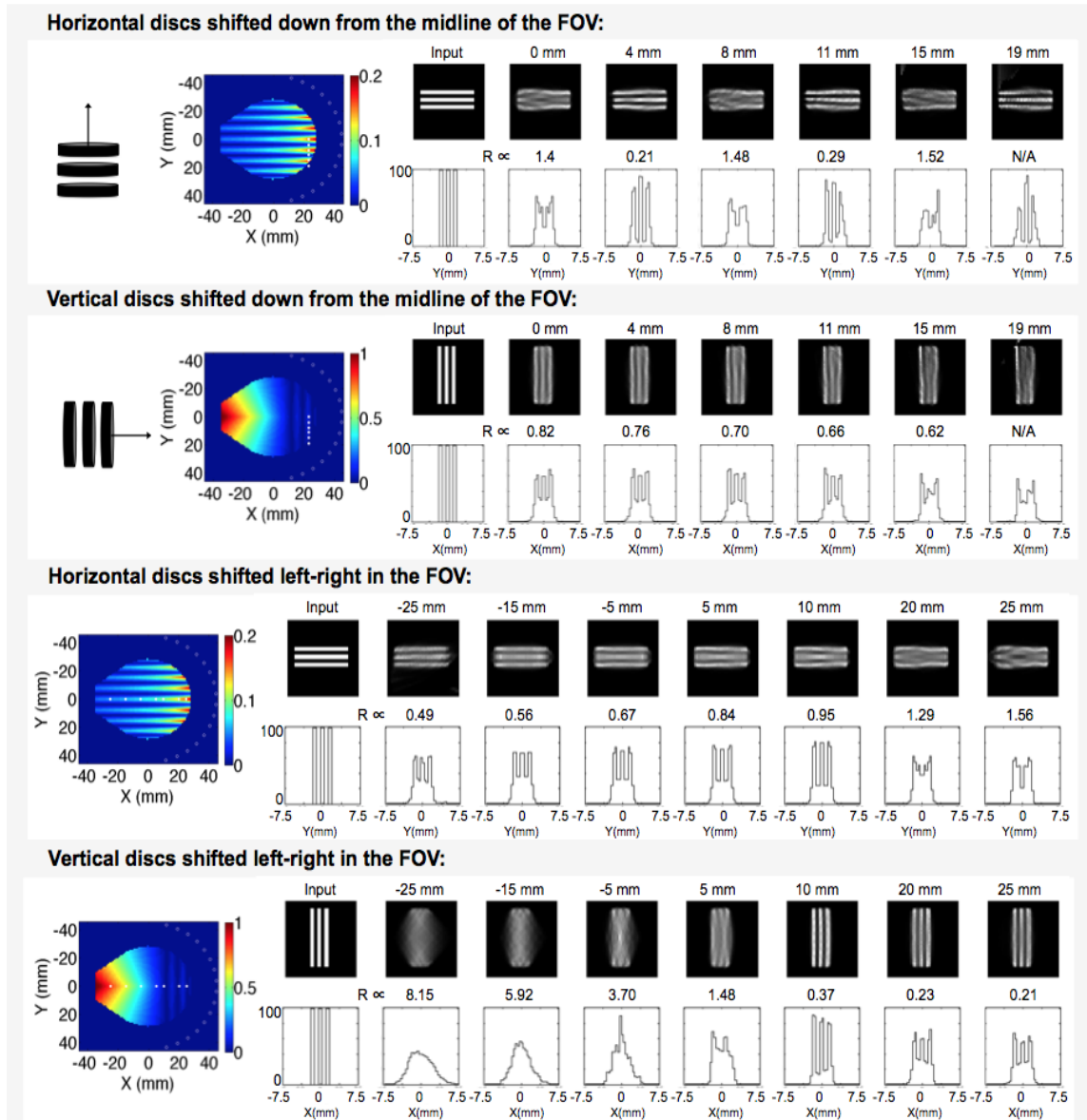


Figure 3.4 Values of theoretical relative resolution,  $R(\vec{x}, \hat{\theta})$ , calculated using Equation 9 are display for the  $Z=0$  plane for pinhole cameras with circular (left) and arc (right) configurations. The scaling factor was  $k = 1$  for all images. The value  $R(\vec{x}, \hat{\theta})$  was calculated for four different directions  $\hat{\theta}$  indicated at the left of each row. The images are comprised of resolution values calculated for each position  $\vec{x}(x, y)$  in the FOV (Figure 3.2). The colour scale for the resolution values has a range of 0 to 0.2 for all images except the inset image; the scale of this image has an extended range of 0 to 1 to show the large values outside of the arc.



**Figure 3.5** Disk phantoms were projected and reconstructed with idealized pinholes (0.75 mm thick, 1.5 mm center-to-center, 5.75 mm radius) at various positions along the x-axis (L-R) and downwards from  $x = 23$  mm in the Y-direction. The histograms are plotted from a central profile parallel to the normal vector to each set of reconstructed disks. The predicted relative resolution,  $R(\vec{x}, \hat{\theta})$ , with  $k = 10$  for each is indicated above the histograms.

$\hat{\theta} = (1,0,0)$ , that the relative resolution for positions outside of the hemisphere enclosed by the pinhole array is poor with a maximum value of  $\sim 1.0$ .

### 3.3.3 Resolution from Simulated Disk Phantom

Reconstructed 3-disk phantoms and the central profile through each are displayed in

Figure 3.5 along with the predicted relative resolution  $R(\vec{x}, \hat{\theta})$  for each when  $k = 10$  mm is assumed.

For a fixed X position of 23 mm and positional shifts in the negative Y-direction (symmetrically identical to the positive direction), it can be seen that when positioned in the spaces between pinholes, the 3-disk phantom with the normal in the Y-direction experiences much more blurring in reconstruction than when it is aligned with the pinholes. This pattern is not however observed when the phantom is oriented with the normal in the X-direction. In both cases, qualitatively, the visual resolution shown by the histograms appears to agree with the corresponding theoretically calculated  $R(\vec{x}, \hat{\theta})$  values.

For shifts of the 3-disk phantom along the X-axis (fixed  $Y = 0$  mm), disks with the normal in the Y-direction were reconstructed well in most positions. Close examination of the 20 mm and 25 mm show a slight resolution drop in the Y-direction when approaching the gap between two pinholes, as predicted by the  $R(\vec{x}, \hat{\theta})$  values from Figure 3.4. The resolution of reconstructed disks with the normal in the X-direction rapidly degraded as the disk position shifted outside of the hemisphere enclosed by the pinhole array.

### **3.4 Discussion**

I have modeled a particular scale of SPECT camera specific to small animal imaging and have found the magnitude of resolution blurring in certain directions to be on the order of the desired camera resolution ( $\sim 1$  mm). Since clinical systems such as the Discovery NM530c have fewer pinholes and a larger pinhole distance from the Z-axis than in our model, similar effects are likely to be seen clinically. Therefore, the model is

relevant for both pre-clinical and clinical imaging when rescaled. Additionally, it is expected that including real effects of intrinsic detector resolution and aperture size may influence the pattern of effects but that the position- and orientation- dependence of resolution will remain.

### **3.5 Conclusions**

Analytical calculations and MLEM reconstructions from simulated pinhole projections both demonstrated a strong dependence of resolution (in the reconstructed images) on position and orientation of an object within the FOV. The greatest resolution losses were observed for positions outside of the hemisphere enclosed by the pinhole array. However, substantial resolution losses in the gaps between pinholes within the hemisphere were also seen.

## **Chapter 4: Patient-specific estimation of spatially-variant image noise for a pinhole cardiac SPECT camera**

*This chapter develops a method for rapid estimation of a map of patient-specific image noise.*

*It has been previously published in a modified format. © 2018 Wiley.*

*Reprinted, with permission, from Cuddy-Walsh, S. G. and Wells, R. G.*

*“Patient-specific estimation of spatially-variant image noise for a pinhole cardiac SPECT camera” Medical Physics, 2018;45(5):2033-2047. In addition to minor formatting changes, some parts of the text in Sections 4.1 & 4.2 have been moved to Sections 1.1 & 2.3.*

## 4.1 Introduction

Myocardial perfusion imaging (MPI) using single photon emission computed tomography (SPECT) detects heart disease based on differences in the signal from accumulated radiotracer in different regions of the heart wall (myocardium). Impaired myocardial perfusion appears as a relative reduction in image signal intensity. The magnitude and correlation (texture) of image noise influences the detectability of disease in images [62]. In cardiac imaging, physicians employ strategies such as evaluating wall motion with electrocardiogram-gated image sequences to determine if an apparent defect is real or noise. Presently, clinical SPECT imaging software does not provide any information about the noise level or distribution in an image. With parallel-hole collimators, sensitivity does not change with source-to-collimator distance which produces a similar signal strength for a source located anywhere within the camera FOV. However, in new dedicated cardiac SPECT cameras with pinhole collimators, such as GE Healthcare's Discovery Nuclear Medicine 530c (DNM530c), the sensitivity, and thus the statistical noise in acquired images, is much more variable over the FOV.

The DNM530c has 19 detectors in a fixed arc (roughly 180-degree coverage) offering increased camera sensitivity for photons without a loss of spatial resolution [24], [33], [83]. Increased photon counting efficiency allows for shorter scan times and/or lower administered radiation doses to patients to produce images clinically equivalent to those of a conventional camera [84]. However, position-dependent attenuation [85] and sensitivity [33] are known features of these designs due to the pinhole collimation and the placement of the detectors arc on one side of the patient. Reconstruction with attenuation correction produces images with an accurate mean count distribution, but the underlying

image noise remains spatially variant.

The usual supine position of the patient relative to the DNM530c has the cardiac apex closest and cardiac base farthest from the arc of detectors. Because the camera sensitivity is highest close to pinhole detectors [33], the apex of the heart has lower image noise than the more distal base of the heart. The noise variations are compounded by the effects of attenuation which, unlike in a conventional parallel-hole collimated camera, change depending on the exact position of the patient in the camera FOV [85]. The increase of image noise from apex to base implies an increase in the difficulty of detecting perfusion defects. Because uncertainty changes throughout the myocardium, a visual representation of the change in noise may assist physicians in interpreting the images.

The objectives of this study were (1) to evaluate the spatial-dependence of noise in the FOV of a multi-pinhole SPECT camera using bootstrapping methods, and (2) to develop and validate an easy and rapid method for analytically estimating a map of the magnitude of noise in a reconstructed image using data from a single clinical acquisition.

## **4.2 Methods**

### **4.2.1 Camera**

A Discovery Nuclear Medicine 530c (DNM530c, GE Healthcare) SPECT camera [24] was used for all image acquisitions and its specifications were used for theoretical models. The DNM530c has a limited-angle pinhole design of 19 pinhole-detector pairs positioned along three parallel L-shaped arcs (5, 9, and 5 detectors per arc) and focused on the heart. Individual detector panels are comprised of an array of  $32 \times 32$  pixels of cadmium zinc telluride (CZT) with a side length of 2.46 mm. Collimators each have a single pinhole aperture with a 5- mm diameter [24]. Camera specific software, Xeleris

(GE Healthcare), reconstructs an object array of  $70 \times 70 \times 50$  voxels with voxel size of  $4 \text{ mm} \times 4 \text{ mm} \times 4 \text{ mm}$ . The supported quality FOV is roughly a 19-cm diameter sphere centred within the FOV. The stationary design of the system allows simultaneous acquisition of all 19 projections with optional list-mode data storage.

The DNM530c does not have an attached CT. For the purposes of this study, CT images used for attenuation correction were acquired with an Infinia-Hawkeye4 SPECT/CT by GE Healthcare (120 kVp, 1.0 mA, 2.0 rpm). The CT image (1.67 mm voxel side length) was manually co-registered (as shown in Appendix A) with emission data from the DNM530c using Xeleris to produce an attenuation map (4 mm voxel side length).

#### **4.2.2 Projected Voxel Noise Estimation ( $\sigma_{PV}$ ) – A new method for estimating local noise in a SPECT image**

##### **The PV method and its assumptions**

Pinhole SPECT image noise is the result of propagating noise in the acquired emission data through the chosen reconstruction algorithm. The noise in the emission data is due to the stochastic nature of photon counting and the electronic noise in the photon detectors. In this method, I assume that the input reconstructed image represents the true activity distribution in the object and that the noise in the projection data is Poisson distributed as in Liew *et al.* [86]. I incorporate variations in sensitivity over the FOV due to attenuation and collimators into our noise estimate. I propose a projected voxel (PV) noise estimation method to estimate the ensemble voxel variance of a reconstructed image voxel as proportional to the variance of a Poisson distribution with a mean equal to the number of detected photons originating from that voxel. The PV algorithm does not propagate the

noise through the reconstruction algorithm as done in iterative methods [62], [76], but instead assumes a linear relationship between the projection noise and the reconstructed noise [86] and rescales the noise using reconstruction-parameter dependent calibration. With knowledge of the camera configuration, the PV method estimates noise using the single reconstructed image for which the noise estimate is desired, and the corresponding attenuation map.

### **Implementing the uncalibrated PV method**

Reconstructed counts at each voxel position are treated as individual point sources of uniform activity and forward projected separately using code developed in-house [13], [85], [87] that includes attenuation. The forward projector uses camera specifications with ray tracing to calculate the system matrix for the camera [87]. Object voxels are subdivided into a  $5 \times 5 \times 5$  subvoxel array and detector pixels into  $11 \times 11$  subpixel array. A system matrix accounting for the geometric sensitivity of the camera,  $g_{pd,v}$ , is pre-calculated and applied to all forward projections weighting the number of counts,  $F_v$ , originating from a voxel,  $v$ , by  $\cos(\theta) \times \frac{s}{h^2}$  where  $s$  is the area of a detector subpixel,  $h$  is the distance between the source and the detector subpixel on pinhole-detector index  $pd$ , and  $\theta$  is the angle between the detector normal and the photon path [28], [88]. An attenuation term,  $a_{p,v}$ , is calculated for each voxel-detector pair. For each voxel, the number of counts detected is calculated considering the effects of camera geometry alone (Equation 10), attenuation alone (Equation 11), and both (Equation 12). The scaling factor terms corresponding to the attenuation ( $\bar{a}$ ) and geometric sensitivity ( $\bar{g}$ ) averaged over all projection pixels and object voxels are employed in Equations 10 and 11

respectively to adjust the total number of projected counts to match the number in the true projection data.

Number of photons detected with geometric sensitivity:

$$(\mu_{proj,v})_G = \bar{a} \sum_{pd=1}^{19 \times 32 \times 32} g_{pd,v} F_v \quad (10)$$

Number of photons detected with attenuation effects:

$$(\mu_{proj,v})_A = \bar{g} \sum_{pd=1}^{19 \times 32 \times 32} a_{pd,v} F_v \quad (11)$$

Number of photons detected (geometric sensitivity + attenuation effects):

$$(\mu_{proj,v})_T = \sum_{pd=1}^{19 \times 32 \times 32} a_{pd,v} g_{pd,v} F_v \quad (12)$$

The relative sensitivity image is calculated as  $\frac{(\mu_{proj,v})_\xi}{\max(\mu_{proj,v})_\xi}$  for each estimation type,

$\xi = G, A, \text{ or } T$ , where  $\max(\mu_{proj,v})_\xi$  is the maximum sensitivity inside the spherical phantom.

I include both the camera geometric sensitivity and attenuation effects in the projected voxel noise estimate. Since I am interested in the variance of individual voxels, counts detected by all detector pixels for each voxel position are summed ( $\mu_{proj,v}$ ) and recorded. To propagate the uncertainty in the total number of counts in projection space ( $\sigma_{proj,v}$ ) to uncertainty in the number of counts reconstructed in image space ( $\sigma_{image,v}$ ) I assume a scalar relationship:

Uncalibrated PV Noise:

$$\begin{aligned} \sigma_{rPV\xi} = (\sigma_{image,v})_\xi &= \left( \frac{\sigma_{proj,v}}{\mu_{proj,v}} \cdot \mu_{image,v} \right)_\xi \\ &= \left( \frac{1}{\sqrt{(\mu_{proj,v})_\xi}} \right) \cdot F_v \end{aligned} \quad (13)$$

## Calibration of the PV method

The uncalibrated or “raw” PV noise estimate ( $\sigma_{rPV}$ ) from (Equation 13) accounts for statistical variation due to Poisson counting statistics, but it assumes that counted photons can be “put back” in their voxels of origin via reconstruction. This ignores the complexities of propagating noise through iterative reconstruction and noise suppression due to unknown implementations of clinical priors in clinical reconstruction software. While others have shown that noise can be determined more accurately with either Monte Carlo techniques [64], iterative analytical methods [62], [76], or bootstrapping [1], I chose a quick and brute force approach to account for the discrepancy by calibrating the rPV noise estimate with an empirical formula.

The  $\sigma_{rPV}$  was calculated using Equations 12 and 13 and image noise was measured from bootstrapped acquisitions of a spherical Tc-99m-water phantom. Linear regression (Equation 14) of the relationship between all  $\sigma_{rPV}$  and measured noise ( $\sigma_{BSV}$ ) was performed for all voxel positions inside the reconstructed volume of the sphere (eroded by 4 voxels to minimize edge effects), and repeated for 7 different counts levels ( $\bar{F}_{object}$ ). The resulting slopes ( $M_{\bar{F}}$ ) and intercepts ( $B_{\bar{F}}$ ) were fit as a function of  $\bar{F}_{object}$  to obtain the coefficients  $m_1$ ,  $m_2$ ,  $b_1$ , and  $b_2$  used to convert  $\sigma_{rPV}$  into a calibrated PV noise estimate ( $\sigma_{PV}$ ), as indicated in Equation 16.

$$\sigma_{rPV} = M_{\bar{F}} \cdot \sigma_{BSV} + B_{\bar{F}} \quad (14)$$

$$\sigma_{BSV} = \frac{1}{M_{\bar{F}}} \cdot \sigma_{rPV} - \frac{B_{\bar{F}}}{M_{\bar{F}}} \quad (15)$$

$$\sigma_{PV}(\sigma_{rPV}, \bar{F}_{object}) = \left( m_1 \cdot (\bar{F}_{object})^{-0.5} + m_2 \right) \cdot \sigma_{rPV} + (b_1 \cdot \bar{F}_{object} \cdot e^{-b_2 \cdot \bar{F}_{object}}) \quad (16)$$

For homogeneous objects,  $\bar{F}_{object}$  is the mean number of counts inside of the object

excluding edge voxels. For cardiac imaging,  $\bar{F}_{object}$  is the mean number of counts inside of the “healthy” myocardial wall defined as having greater than 70% of the maximum number of counts in the myocardium. For this purpose, the maximum number of counts is defined as the mean of the highest 1% of voxel values in the middle 5 transverse slices of the myocardium.

#### **4.2.3 Measured Noise ( $\sigma_{BSV}$ ) – Non-parametric bootstrapping**

##### **Image Acquisition**

A 12-cm diameter spherical Tc-99m-water phantom was centered in the FOV and imaged with a 100-second acquisition ( $\sim 10^7$  projected counts) in list-mode on the DNM530c. The mean reconstructed number of counts inside the phantom was  $\bar{F}_{object} = 1.1 \times 10^6$ . The 100 s projection set was relisted using an Xeleris workstation (GE Healthcare) into projection sets containing the first  $t = 10, 20, 30, 40, 60,$  and  $80$  seconds,  $\bar{F}_{object} = (1.2, 2.3, 3.4, 4.6, 6.9,$  and  $9.2) \times 10^5$  respectively. This created images with 7 different noise levels for calibrating our PV estimate.

##### **Bootstrapping for noise analysis**

A non-parametric bootstrapped approach [1] was used to generate  $N = 392$  different noise realizations of each projection set of the Tc-99m-spherical-water-phantom data. Each projection set was relisted into 300 sub-sinograms (projection sets), each with  $\frac{t}{300}$  duration. Bootstrapping was performed off-line with in-house software, drawing 300 samples with replacement from the 300 sub-sinograms for each of the 19 projection angles. An in-house evaluation demonstrated a requirement of  $\sim 400$  bootstrapped images to converge to within 5% of the standard deviation distribution associated with repeat

measurements of the voxel values (Appendix B). This was consistent with the recommendation by Buvat *et al.* to use at least 200 bootstraps [1]. I bootstrapped 392 images for each of the 7 noise levels since vendor software allowed batches of 98 reconstructions at one time.

## **Reconstruction**

Unless otherwise indicated, each bootstrapped projection set was reconstructed with attenuation correction using 60 iterations of the vendor-supplied maximum a posteriori expectation maximum (MAP-EM) algorithm and the one-step-late Green (OSLG) prior ( $\alpha=0.7$  and  $\beta=0.5$ ). Neither scatter correction [13] nor post-reconstruction filtering were performed for the main body of this work to avoid distorting the Poisson nature of the noise I was modelling. An attenuation map was generated from a CT scan of the spherical phantom acquired on an Infinia-Hawkeye4 SPECT/CT (GE Healthcare) [89]. The attenuation map was manually co-registered with the image from the 100 second complete data set and the same registration used for all 392 x 7 projection sets. No post-reconstruction filtering was performed.

It was anticipated that the calibration coefficients would change with changes in the reconstruction parameters or algorithm since the PV method does not model the reconstruction. To explore the variation in calibration with reconstruction method, I considered three additional approaches: 60 iterations of maximum likelihood estimation maximization (MLEM) – removing the Bayesian noise regularization, 40 iterations of MAP-EM OSLG ( $\alpha=0.51$  and  $\beta=0.3$ ) – reducing the number of iterations and prior strength, and 60 iterations of MAP-EM OSLG ( $\alpha=0.7$  and  $\beta=0.5$ ) with scatter correction using a modified dual-energy window method [90].

## **Measured noise calculation**

For each voxel in the reconstructed image, I computed the mean and variance (using Welford's method [91]) of the voxel value over the 392 bootstrapped images. This was repeated for all 7 noise levels.

## **Inter-voxel Noise Correlation**

Because the PV method calculates the noise for each image voxel independently based on the mean image voxel value, noise correlations in the image are not considered. To investigate the strength and spatial variation of the noise correlation for the DN530c, I calculated an image of correlation length between each voxel and its neighbours using images obtained from bootstrapping. Specifically, I calculated the covariance over 392 noise realizations between a given voxel and all voxels up to a radial distance of 10 voxels. The distribution of covariance measurements about the central voxel was assumed to be approximately Gaussian and the correlation length was defined as the radial distance at which the covariance falls to half of the voxel's variance [64]. The correlation length was measured in the cartesian directions (x, y, z) and for a radial average. Correlation lengths were calculated for each point inside the uniform spherical phantom and for each point inside the myocardium for 27 of the clinical patients.

### **4.2.4 Application to clinical cases**

#### **Patient image acquisition and reconstruction**

To validate our PV noise estimation model, I performed a retrospective evaluation of cardiac perfusion rest scans acquired on the dedicated cardiac DNM530c following an injection of  $(342 \pm 20)$  MBq of  $^{99m}\text{Tc}$ -tetrofosmin (activity was measured and recorded

for each patient at the time of injection). Associated attenuation maps were acquired on an Infinia-Hawkeye4 SPECT/CT. Patient body mass ranged from 45-102 kg,  $81 \pm 14$  kg on average. Five minutes of list-mode data were used for analysis. 31 patient cases were selected for study. Cases were retrospectively drawn from those in our clinical database for which imaging was performed on both the Infinia and DNM530c cameras [90]. These patients were chosen with a view toward later comparisons of the noise between cameras (Chapter 5). Images were included if studies had a summed stress score of less than 4 and the heart was positioned such that the center of the myocardium was within a sphere of 7 voxel radius. A subset of 15 of these with visually normal images were used for population aggregate results.

All images were reconstructed with 60 iterations of MAP-EM OSLG ( $\alpha=0.7$ ,  $\beta=0.5$ ). A 3-dimensional Butterworth filter (order 7, frequency = 0.37) was applied to one patient case to assess changes introduced by the low-pass filtering typically used in our clinic.

### **Estimating noise with the calibrated PV model**

Noise images were estimated for each patient using the PV algorithm (Equations 10-12 and 16) with the patient-independent camera-specific geometric sensitivity map, a patient-specific attenuation map, and the calibration coefficients determined from phantom experiments (Table 4.1). The attenuation map was manually registered to the original non-bootstrapped patient emission image using the Xeleris workstation. A single reconstructed image was used as an estimate of the mean radiotracer distribution,  $F_v$ , for calculating the PV noise estimate.

## Measuring noise with bootstrapping

The initial 300 seconds of each patient's projection images at rest were bootstrapped (392 bootstraps, 300 1-second sub-sinograms) and reconstructed with the same specifications as for the spherical phantom.

## Statistical analysis

Statistical analysis was performed on the myocardial voxels. To identify myocardial voxels, a mask was created by semi-automatically segmenting an ellipsoid around the heart, excluding voxels with  $F_v < 50\%$  of the maximum, and eroding the edges of the result by one voxel. For all voxels inside the mask ( $1600 \pm 400$  voxels), the correlation ( $R^2$ ) and coefficient of variation (CV) between  $\sigma_{PV}$  and  $\sigma_{BSV}$  were compared on a voxel-by-voxel basis.

For statistical analysis and comparison, I used the relative standard deviation,  $\sigma_v[\%]$  to express the image noise relative to the 'maximum' (mean of highest 0.1% of myocardial voxels) voxel intensity in the myocardium.

Relative image noise:

$$\sigma_v[\%] = \sigma_v[\text{counts}] / \max(\text{myocardial voxel}) \times 100\% \quad (17)$$

## 4.3 Results

### 4.3.1 Sensitivity variability in the field-of-view

Maps of sensitivity in the FOV of the DNM530c show the relative fraction of photons detected by the camera in Figure 4.1. Ranges are reported for all voxels values inside of the homogenous region of the reconstructed sphere (to reduce edge effects, the outer two voxels have been eroded and the voxels corresponding to the phantom valve have been removed). The fraction of detected photons in the transverse plane ranges over 12-cm

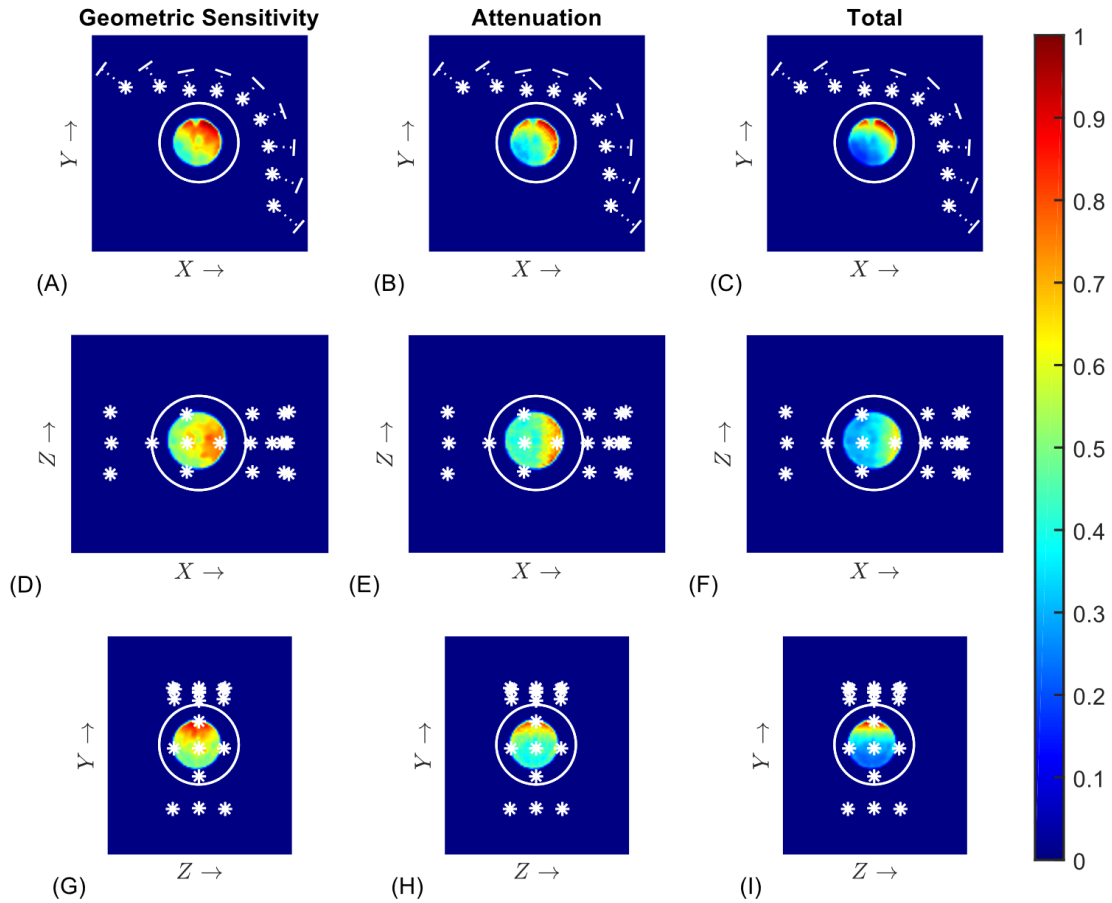


**Figure 4.1** A central slice through a spherical  $^{99m}\text{Tc}$ -water phantom relative to the positions of the 19 pinholes and detectors (represented by white stars and lines) composing the DNM530c SPECT camera (GE Healthcare). Three views are displayed: (A)-(C) the transverse plane, (D)-(F) the sagittal plane, and (G)-(I) the coronal plane. Each image demonstrates the variation of the relative fraction of detected photons from one region of the quality FOV (represented by a white circle) to another. The variation is calculated using the effects of geometric sensitivity [(A), (D), (G)], attenuation [(B), (E), (H)], and both [(C), (F), (I)]. The 12-cm diameter phantom is centered inside the supported field-of-view of the camera.

from 1 to 0.40 (2.5 $\times$ ) when only geometric sensitivity is considered, from 1 to 0.34 (2.9 $\times$ ) when only the effects of attenuation are considered, and from 1 to 0.21 (4.8 $\times$ ) when both effects are considered. In the coronal plane, the ranges are from 0.76 to 0.45 (1.7 $\times$ ), 0.70 to 0.40 (1.8 $\times$ ), and 0.67 to 0.26 (2.6 $\times$ ) respectively. In the sagittal plane, the fraction of photons ranges from 0.88 to 0.50 (1.8 $\times$ ), 0.82 to 0.43 (1.9 $\times$ ), and 0.85 to 0.22 (3.9 $\times$ ) respectively. The range of relative fractions over the entire phantom is the same as for the transverse plane. The sensitivity estimated using the effect of geometric sensitivity alone

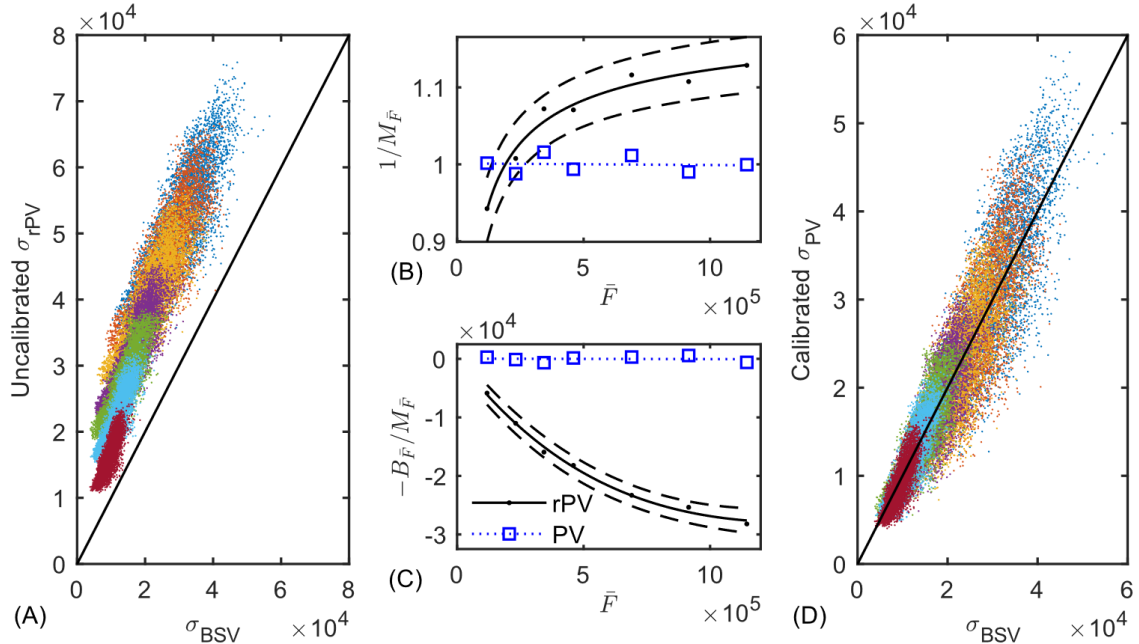


**Figure 4.2 Empirical calibration curves and results. (A)** The uncalibrated PV noise estimate ( $\sigma_{rPV}$ ) is plotted as a function of the noise determined by bootstrapping ( $\sigma_{BSV}$ ) for 7 different image count levels. **The (B) slope and (C) intercept of linear fits of each of the data sets in (A) are plotted as a function of the mean number of counts per image voxel ( $\bar{F}_{object}$ ) and fit with empirical functions (black dots and lines). The fit functions are used to correct the data in (A) and this is plotted in (D). The slope and intercepts for the calibrated PV noise ( $\sigma_{PV}$ ) are plotted in (B) and (C) with blue squares and dotted lines. All noise values  $\sigma$  and the intercepts are expressed as the percentage of the ‘maximum’ (mean of highest 0.1%) value in the reconstructed sphere. The slope is unitless and the mean counts per voxel is self-explanatory.**

has a similar gradient magnitude to previous sensitivity measurements [33]. The estimated magnitudes of the attenuation and geometric sensitivity effects are similar and so they contribute almost equally to the overall variation in local image noise.

#### 4.3.2 Speed of measurement and calculation

In addition to the time required to reconstruct the mean image, which the same image used for clinical interpretation, the PV method requires 1 minute (64 seconds) of computation time (running on a single core of a laptop with Intel® Core™ i7-6700HQ CPU @ 2.60GHz, 2.59GHz, 16 GB RAM, Windows 10). The BSV method requires approximately 5 hours to relist and bootstrap the projection data, reconstruct all 392 images, and calculate the standard deviation.

**Table 4.1 Calibration coefficients to be used with Equation 16 for the PV method of image noise estimation (Equations 12-13). Determined by fitting linear fit coefficients  $M_{\bar{F}}$  and  $B_{\bar{F}}$  from Equation 14 for 7 different count levels as shown in Figure 4.2(B) - Figure 4.2(C). The coefficient value and 95% confidence interval (CI) is provided for each. Calibration coefficients are specific to 60 iterations of MAP-EM with one-step-late Green's prior ( $\alpha = 0.7$ ,  $\beta = 0.5$ ) reconstructions.**

	Mean	CI (95%)
$m_1$	-95.4	(-114.2, -76.63)
$m_2$	1.218	(1.186, 1.251)
$b_1$	-0.05657	(-0.06149, -0.05165)
$b_2$	$7.445 \times 10^{-7}$	$(6.407, 8.482) \times 10^{-7}$

### 4.3.3 Noise in Images of a Spherical Phantom

Results for the calibration and evaluation of the PV noise estimation method using a spherical phantom are presented in Figure 4.2, Figure 4.3A, and Figure 4.4. Figure 4.2 shows the need for count level dependent calibration and the result of its application. Correlation results for one count level are depicted in Figure 4.4. The mean and range of measured and estimated image noise are displayed as boxplots in Figure 4.3A for each count level.

#### Image characteristics

Reconstructed images (Figure 4.4) of the phantom at all count levels contain local inhomogeneities that are likewise observed in the noise images. The valve of the rubber ball phantom is observed as a regional count deficit at approximately 12 o'clock on Figure 4.4A.

#### Correlation of noise between raw PV estimate and BSV measurement

The raw calculated noise estimate,  $\sigma_{rPV}$ , is approximately linearly related to, and strongly correlated with ( $R^2 = 0.71 \pm 0.03$ ), the noise determined via bootstrapping methods for the 7 noise levels ( $\bar{F}_{object}$ ) evaluated in our phantom study (Figure 4.2A).

Data at individual noise levels are heteroskedastic with a narrower distribution about the mean for low noise than high noise (Figure 4.3A). The slope and intercept of the data (Figure 4.2B - Figure 4.2C) also changes for each different noise level.

### **Calibration of PV estimated noise**

Comparisons of  $\sigma_{BSV}$  and  $\sigma_{rPV}$  in Figure 4.2A show that the  $\sigma_{rPV}$  method consistently overestimates the bootstrapped noise at all 7 count levels. This offset is highly dependent upon the count level of the evaluated phantom image. Accordingly, calibrations were formulated with dependencies of the coefficients on the mean number of reconstructed counts ( $\bar{F}_{object}$ ) inside of the eroded phantom image. Figure 4.2B and Figure 4.2C show the slope and intercepts for linear fits of  $\sigma_{rPV}$  and calibrated  $\sigma_{PV}$  noise as a function of  $\sigma_{BSV}$ . The scatterplot of the calibrated  $\sigma_{PV}$  noise estimate and  $\sigma_{BSV}$  noise (Figure 4.2D) shows noise estimates for all counts levels to follow the same trend (where  $\sigma_{rPV}$  had offsets, Figure 4.2A). Calibration coefficients for Equation 16 are listed in Table 4.1 specifically for reconstruction with MAP-EM one-step-late Green's Prior ( $\alpha=0.7$ ,  $\beta=0.5$ ).

Example images in Figure 4.4 for the  $\bar{F}_{object} = 2.3 \times 10^5$  count level compare the  $\sigma_{BSV}$  (Figure 4.4B) and calibrated  $\sigma_{PV}$  (Figure 4.4C) noise estimates. The resulting slope of a fit to a scatter plot comparing the two methods of estimating percent noise (Figure 4.4D) is close to unity (1.01), the intercept is 0.05%, and  $R^2 = 0.73$ . A Bland-Altman analysis (Figure 4.4E) gives the coefficient of variation as 16%. Statistics for all 7 count levels are plotted in Figure 4.9 for comparison with clinical results. The relationship follows the line of identity (average slope =  $1.00 \pm 0.01$  and intercept =  $0 \pm 0.1$ ), with a strong positive correlation ( $R^2 = 0.71 \pm 0.03$ ), and a coefficient of variation of  $(17 \pm 1)\%$ .

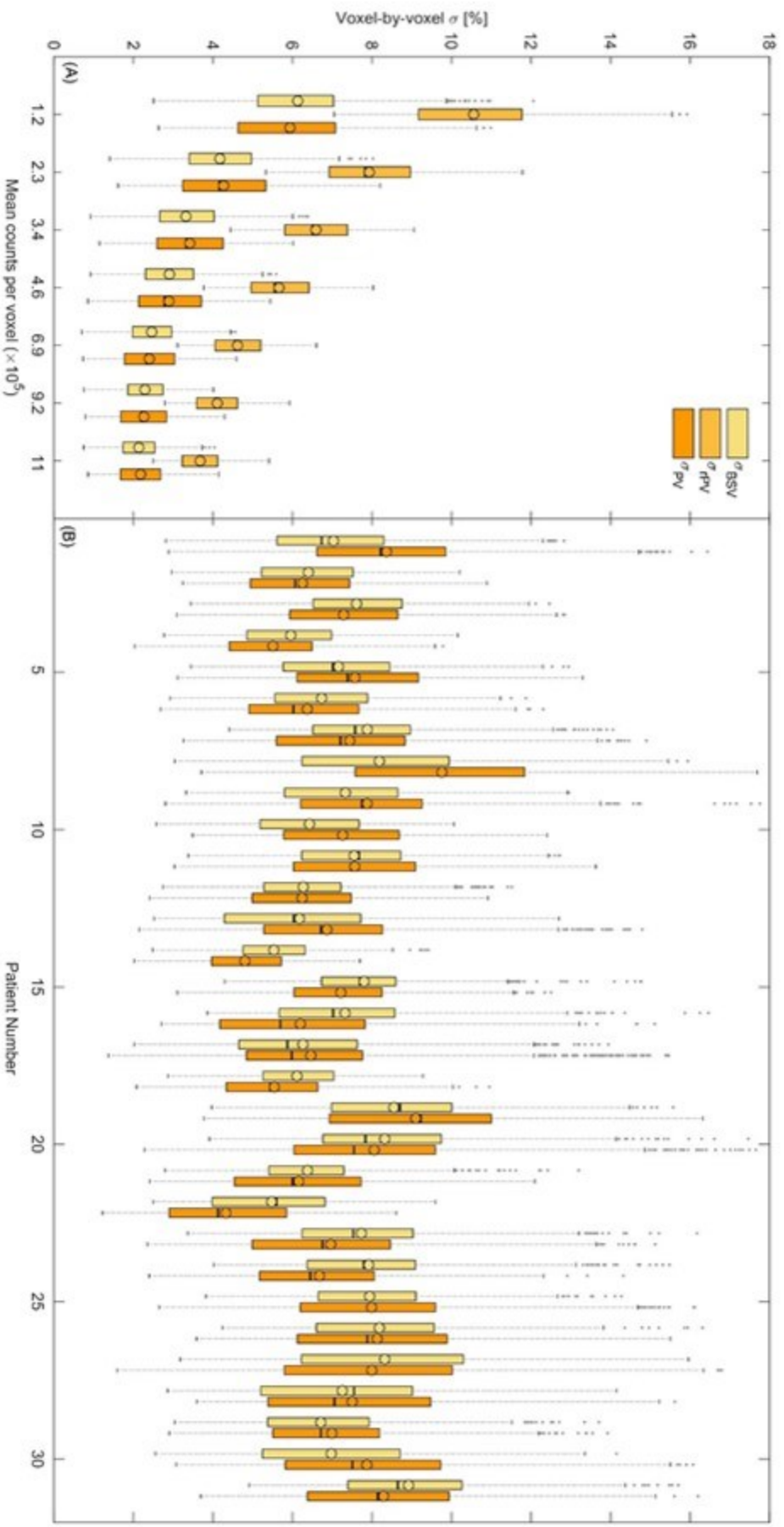


**Figure 4.3** Boxplots summarizing the image noise in all voxels of (A) the spherical phantom at 7 different count levels and (B) 31 different cardiac patients. Noise calculated with bootstrapping ( $\sigma_{BSV}$ ) and the projected voxel method ( $\sigma_{PV}$ ) for different count levels described by the mean number of counts per voxel inside the phantom ( $F_{object}$ ). The uncalibrated raw PV noise estimate ( $\sigma_{PV}$ ) is plotted in (A) only. The mean number of counts in the patient myocardium was  $(2.2 \pm 0.4) \times 10^5$ . The circles mark the mean noise value, boxes depict the range from the 1<sup>st</sup> to 3<sup>rd</sup> quantiles, and the error bars represent the total range of the variable noise excluding statistical outliers (represented by dots).

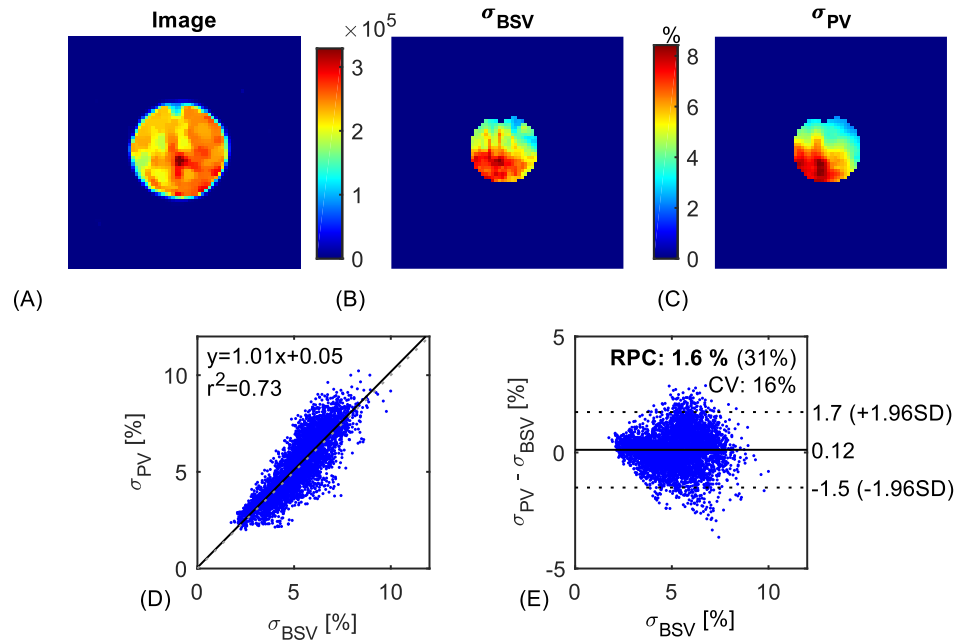


**Figure 4.4 (A) Measured image of spherical phantom at second count level (mean counts  $\sim 2.3 \times 10^5$ ). Noise for this image is determined by (B) bootstrapping ( $\sigma_{BSV}$ ) and (C) the calibrated projected voxel ( $\sigma_{PV}$ ) method. A transverse central slice for each is displayed and units are expressed as the percent of the mean of the maximum 0.1% of voxel values in the sphere. The relationship between the bootstrapping and calibrated PV methods is shown in a (D) voxel-by-voxel scatterplot and (E) a Bland-Altman plot.**

### Variable noise in the FOV

Figure 4.4 displays central transverse slices of images of a uniform spherical phantom at the second highest evaluated noise level (20s of data,  $2.3 \times 10^5$  counts in each voxel, or  $1.6 \times 10^6$  projection counts). The central slice from the single image (Figure 4.4A) has an approximately homogenous distribution with some slight internal structural variation that is assumed to be attributed to the reconstruction algorithm. The magnitude of image noise varies spatially in the phantom images Figure 4.4B - Figure 4.4C). A 3-fold change in the reconstructed voxel value is present for  $\bar{F}_{object} = 2.3 \times 10^5$ , ranging from 2.4% proximal to the detector array (top right) to 7.2% distally (bottom left).

The average noise value, measured or estimated, has an approximate power function relationship, decreasing with the increasing average number of counts per voxel in the

sphere (Figure 4.3).

Noise images for the four different sets of reconstruction parameters considered are shown in Figure 4.5A. The bootstrapped noise from the MLEM reconstruction contains a Gibbs artifact that is not evident with the MAP-EM OSLG reconstructions. The average noise is highest in the MLEM case and the variability in the noise across the FOV increased with increased strength of the one-step-late Green's prior.

### **Variable noise correlation length in the FOV**

Bootstrapped images were used to create maps of noise correlation lengths for different reconstruction parameters. The central transaxial slice through the correlation length (CL) map of the sphere phantom is shown in Figure 4.5B. Results presented were calculated using images bootstrapped with a uniform  $N = 4.2 \times 10^5$  counts per voxel in the sphere, but CL values were similar for all counts levels. When considering the CL in each cartesian direction, the value is highest farthest from the detectors that have the best resolution in that plane. Correlation lengths in the X-direction are highest on the left side of the sphere, where the detectors with their normal aligned close to the X-axis are positioned to the right. The radial average CL is seen to be highest at the lower left of the sphere which is on average farthest away from all detectors in the camera. CL values averaged over the phantom volume are reported with their standard deviation in Table 4.1.

CL is lowest for the MLEM reconstruction and increases with increasing strength of the OSLG prior (Figure 4.5B, Table 4.2). The average radial CL increases from 1.2 voxels in the top right of the sphere to 1.7 voxels at the lower left for the MLEM reconstructions. The average radial CL ranged from 1.6-1.9, 1.8-2.0, and 1.7-2.0 voxels for the three

**Table 4.2 Average image noise correlation lengths (CL) for Phantom and Cardiac Patient Studies.** Correlation length is defined as the distance in voxel units at which the correlation value in a neighbouring voxel reaches 50% of the variance for a given voxel. The average CL and its uncertainty for the phantom are the mean and standard deviation of CL values measured within the sphere; for the patient studies they are the average over 27 patients of the mean and standard deviation in the CL values within the myocardium.

	X-direction	Y-direction	Z-direction	Radial Average
<b>Phantom (12-cm diameter):</b>				
(i) 60 iterations, MLEM (No Prior)	$1.5 \pm 0.3$	$1.6 \pm 0.4$	$1.2 \pm 0.2$	$1.4 \pm 0.2$
(ii) 40 iterations MAP-EM, OSLG $\alpha=0.51$ $\beta=0.3$	$1.8 \pm 0.4$	$1.8 \pm 0.4$	$1.5 \pm 0.2$	$1.6 \pm 0.2$
(iii) 60 iterations MAP-EM, OSLG $\alpha=0.7$ $\beta=0.5$	$1.9 \pm 0.4$	$1.9 \pm 0.4$	$1.6 \pm 0.3$	$1.7 \pm 0.3$
(iv) 60 iterations MAP-EM, OSLG $\alpha=0.7$ $\beta=0.5$ , DEW	$1.7 \pm 0.3$	$1.8 \pm 0.4$	$1.5 \pm 0.3$	$1.6 \pm 0.2$
<b>Average Cardiac Study:</b>				
40 iterations MAP-EM, OSLG $\alpha=0.51$ $\beta=0.3$	$1.8 \pm 0.3$	$1.9 \pm 0.3$	$1.5 \pm 0.2$	$1.7 \pm 0.2$
60 iterations MAP-EM, OSLG $\alpha=0.7$ $\beta=0.5$	$1.9 \pm 0.4$	$2.0 \pm 0.4$	$1.7 \pm 0.4$	$1.8 \pm 0.3$

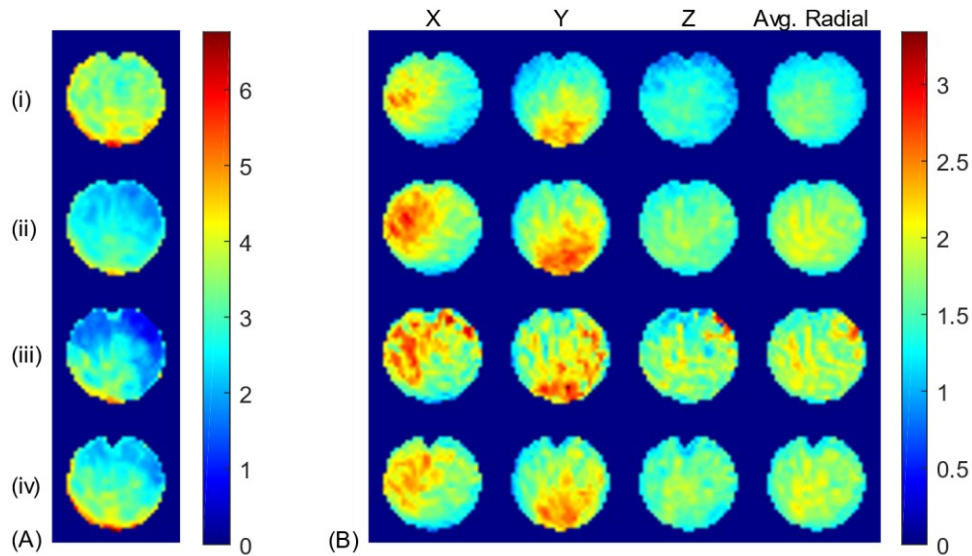


**Figure 4.5 Position and directional dependence of the (A) image noise [%] and (B) correlation length [voxels] determined via bootstrapping projection data and reconstructing using 4 different parameterizations: (i) 60 iterations of maximum likelihood estimation maximization (MLEM); (ii) 40 iterations of maximum a posteriori expectation maximum (MAP-EM) with one-step-late Green prior (OSLG) parameters  $\alpha=0.51$  and  $\beta=0.3$ ; (iii) 60 iterations MAP-EM with OSLG prior ( $\alpha=0.7$  and  $\beta=0.5$ ); and (iv) the same as (iii) with dual-energy window (DEW) scatter correction. Central transaxial slices are shown. Each slice has been cropped from  $70 \times 70$  to  $35 \times 35$  voxels. The detector arc (not shown) is positioned to the top and right of the phantom in these images.**

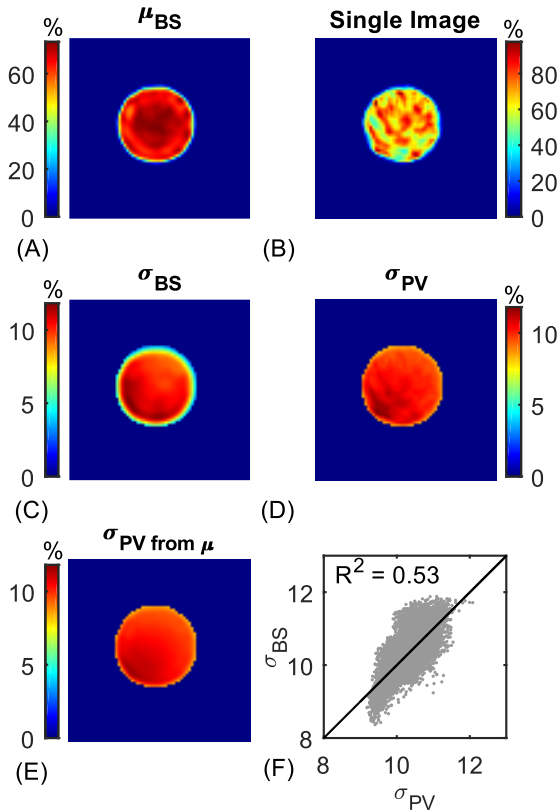


**Figure 4.6** Images determined for reconstruction with 60 iterations of MLEM of noisy projections of a uniform digital sphere (15-cm radius) and corresponding attenuation map (15-cm radius). The (A) mean  $\mu_{BSV}$  and (C) standard deviation  $\sigma_{BSV}$  of 400 bootstrapped images is shown. The  $\sigma_{BSV}$  is smoothed using a 1.6 voxel Gaussian kernel. A single image (B) is displayed along with (D) the noise image  $\sigma_{PV}$  estimated with the PV method. Image (E) shows the PV noise estimated with the mean image (A). In (F),  $\sigma_{BSV}$  values are plotted as a function of  $\sigma_{PV}$  values for all points inside the sphere (eroded by 3 voxels). Noise and image values are expressed as a percentage of the maximum voxel value in the true object.

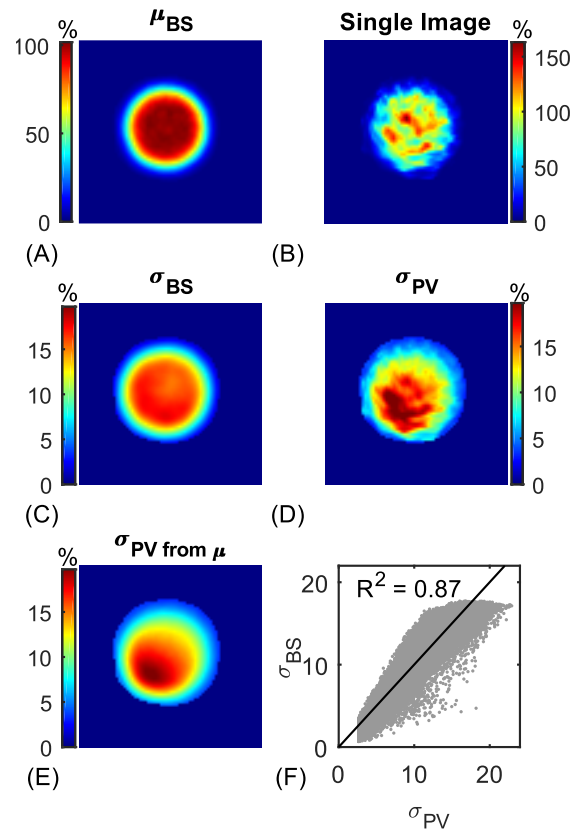


**Figure 4.7** The same images as in Figure 4.6 are shown for reconstruction with 60 MLEM iterations of noisy projections from a uniform digital sphere (15-cm radius) blurred with a 1.6 voxel Gaussian kernel and enlarged corresponding attenuation map (22-cm radius). All values are expressed as a percentage of the maximum value in the true object. The mean counts per voxel in the simulated sphere is equivalent to the 10 second sphere case ( $\bar{F}_{\text{object}} = 1.2 \times 10^5$  cnts).

MAP-EM OSLG reconstructions.

### **Priors, Gibbs artifact, and noise estimation**

Bootstrapped and PV noise images were estimated for MLEM reconstructions of a digital spherical phantom with sharp (Figure 4.6) and blurred edges (Figure 4.7). In the reconstructed image and  $\sigma_{BSV}$  image of the sharp-edged phantom Figure 4.6A and Figure 4.6C, an increase in activity is seen near the edge that is associated with a Gibbs artifact. This is not visible when the true object is blurred as in Figure 4.7. The PV method does not produce the same artifact. The Gibbs artifact reduces the correlation between the bootstrapped and PV methods from  $R^2 = 0.87$  in Figure 4.7 to  $R^2 = 0.53$  in Figure 4.6.

#### **4.3.4 Validation Evaluating Noise in Clinical Cardiac Images**

Results from empirically calibrating the PV estimated noise in 31 patients using the phantom-determined coefficients in Equation 16 are presented in Figure 4.3B, Figure 4.8, Figure 4.9, and Figure 4.10. The mean and range of measured and estimated noise for individual patients are shown in Figure 4.3B for comparison with phantom results in Figure 4.3A. Individual images and correlations are shown in Figure 4.8 for a single patient case. Figure 4.9 summarizes the correlation of the relationship between measured and PV estimated noise for all patients and phantom count levels. Visual inspection of the 31 patient images identified potential mild perfusion deficits in 16 patients; inter-patient and intra-patient population statistics for the remaining 15 patient images are presented in Figure 4.10.

The inter-voxel correlation length was calculated for a subset of the patient studies ( $N=27$ ). Average CL values (calculated for all voxels in the myocardium and all  $N$  patient studies) for MAP-EM reconstructions with two different sets of parameters are similar to

CL values from the phantom studies (Table 4.2).

## Correlation of noise estimation methods

### Voxel-by-voxel comparison

In Figure 4.8, noise estimates determined by our PV method are compared to

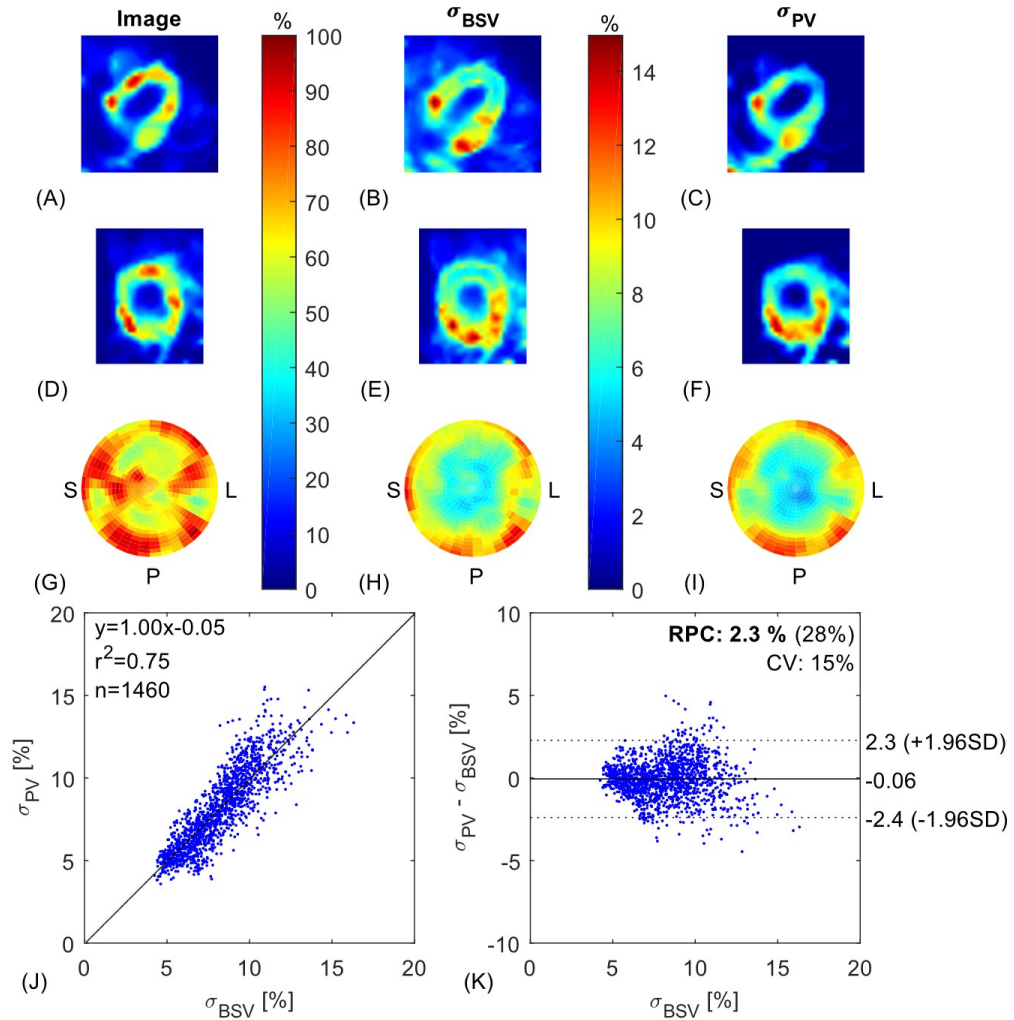


**Figure 4.1** Measured images and noise images estimated with bootstrapping ( $\sigma_{BSV}$ ) and the calibrated projected voxel method ( $\sigma_{PV}$ ) are presented for a  $^{99m}\text{Tc}$ -tetrofosmin rest cardiac study of a single patient [#27 from Figure 4.3(B)]. Images are displayed as (A)-(C) transverse and (D)-(F) sagittal slices through the center of the left ventricle in the camera's reference frame. For full visual assessment,  $18 \times 36$  segment cardiac polar maps are also shown of the image (G),  $\sigma_{BSV}$  (H) and  $\sigma_{PV}$  (I). Image and noise image values are expressed as a percentage of the maximum voxel values in the myocardium. A (J) scatterplot and (K) Bland-Altman plot show the relationship noise estimate methods. Results from this assessment for all patients are summarized in Figure 4.9.

bootstrapped noise measurements using a (J) scatterplot and (K) Bland Altman plot. The fit line in the scatterplot is very close to unity (slope = 1.0, intercept = -0.05) and data have strong positive correlation ( $R^2 = 0.75$ ). The Bland Altman analysis indicates that the PV method's systematic bias is low (-0.06%) and its coefficient of variation is 15%.

The slope, intercept, correlation, and coefficient of variation comparing the calibrated PV noise estimate and the BSV noise are summarized for all 31 patients in Figure 4.9. On average, the relationship between the calibrated PV noise estimate and the BSV noise can be described by:  $\sigma_{PV} = (1.0 \pm 0.1)\sigma_{BSV} + (0.1 \pm 1.0)$ ,  $R^2 = 0.69 \pm 0.06$ . All evaluated clinical images had count levels within the same range as the lowest three phantom count levels. The average CV was  $(17 \pm 2)\%$  and the systematic error is close to zero  $\sigma_{PV} - \sigma_{BSV}[\%] = (0.1 \pm 0.7)\%$ .

The noise range for the two methods is qualitatively visualized in Figure 4.3B. In most cases the noise range (excluding outliers) and mean noise values are very similar between methods, however the range from 1<sup>st</sup> to 3<sup>rd</sup> quartile is approximately 1.16 times larger for the PV method than for the BSV method ( $p = 10^{-7}$ ). The difference between the mean  $\sigma_{PV}$  and mean  $\sigma_{BSV}$  in Figure 4.3B is approximately normally distributed with a mean of 0.06% and standard deviation of 0.69%. Compared with phantom data in Figure 4.3A we also see that the average noise level in the patient images is slightly higher than the noise in the phantom at clinically comparable count levels ( $\bar{F}_{object} = 1.2 \times 10^5 - 3.4 \times 10^5$  counts per voxel).

### **Cardiac polar map comparison**

Converting from a voxelized three-dimensional image to a cardiac bullseye polar map representation introduces slight biases to the noise estimation. The average slope and

intercept for a linear fit between the two estimation methods increases from 1 to 1.2 and decreases from 0.1% to -1.3% respectively. This change is likely because the conversion to polar maps introduces some smoothing to the data and selects out the maximum heart activity. For the polar maps, the average relationship between estimated noise and bootstrapped noise has a higher correlation ( $R^2 = 0.83 \pm 0.04$ ), and higher precision (lower  $CV[\%] = 15 \pm 3$ ). The accuracy remains high with a low average systematic difference between percent noise determined by PV estimation and measurement of ( $0.3 \pm 0.8$ )%.

### **Variable noise in the myocardium (individual cases)**

Example images from the validation study of the noise estimation in clinical MPI images are presented in Figure 4.8. Central transverse and sagittal slices are displayed in the camera's reference frame to clearly associate the image noise variation to the position of the heart relative to the detectors. The voxel values in all images are expressed as a percentage of the maximum voxel value in the myocardium of the original reconstructed image. Two views of the reconstructed patient image in Figure 4.8A and Figure 4.8D show a heterogenous distribution of activity in the myocardium. The bootstrapped (Figure 4.8B and Figure 4.8E) and calculated noise estimates (Figure 4.8C and Figure 4.8F) show similar trends with a 2.5-fold  $\sigma_{BSV}$  (5.3 to 13.9%) and 2.5-fold  $\sigma_{PV}$  (4.0 to 10.3%) increase in noise from the apex to the base of the heart and a 1.5-fold increase (7 to 10%) for both methods from the septum to the lateral wall of the left ventricle. Similar results are seen when we compare cardiac polar maps on a segment by segment basis (Figure 4.8H and Figure 4.8I).

The noise range is different for each patient image. We see in Figure 4.3B that the

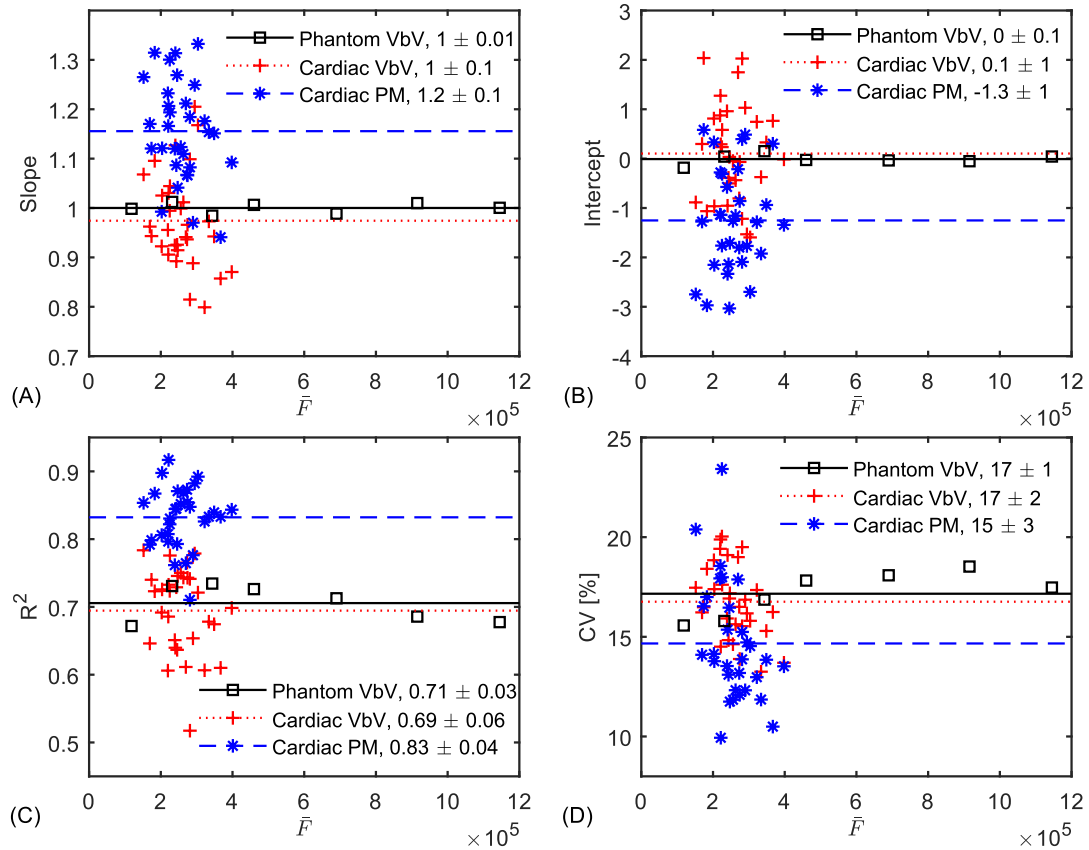


**Figure 4.9** Assessment of the variation in the relationship between bootstrapped noise and noise determined by the PV estimation method. A total of 7 phantom cases and 31 patient cases are shown. The comparison for each image is performed in two ways: (1) comparing voxel-by-voxel (VbV) for all voxels in the phantom or myocardium, and segment-by-segment of each  $18 \times 36$  segment cardiac polar map (PM). Markers represent the values for individual cases and lines represent the mean value. Four comparative metrics obtained from Bland Altman analysis (Figure 4.4(D) - Figure 4.4(E) and Figure 4.8(J) - Figure 4.8(K)) are shown as a function of the mean number of counts per phantom or myocardial voxel: (A) slope, (B) intercept, (C)  $R^2$  value, and the (D) coefficient of variation (CV) between noise estimation techniques.

noise for patient #4 ranges from 2.5 to 10% over the length of the myocardium. For patient #8, the noise ranges from 4 to 17% with the PV method or 3 to 15% with the BSV method. These two patients have larger noise ranges; the range from 3.5 to 12% for Patient #11 from Figure 4.8 is more representative of typical range of noise over the length of the heart for the entire ( $N=31$ ) patient group.

The average ( $N = 27$  patients) of the mean and standard deviation of the correlation length between voxels in the myocardium is given in Table 4.2. The correlation lengths

follow a similar spatial gradient for values within the myocardium (not shown) as for values within the spherical phantom in Figure 4.5B.

### Intra- and inter-patient noise in a normal population

Polar maps of the measured image noise (Figure 4.10A) and PV estimated noise (Figure 4.10B) were averaged for 15 healthy patient images to obtain an estimate of isolated camera noise at that position in the FOV for an approximately 340 MBq rest study. The mean local noise varies more than 2-fold over the length of the heart, approximately from 4.1% at the apex to 8.6% at the base of the heart. It is clear from the

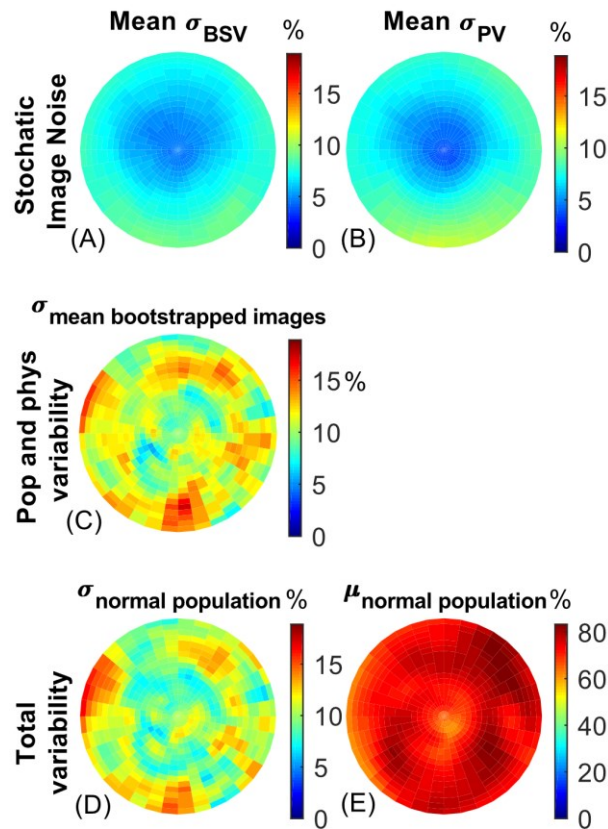


**Figure 4.10** Summary cardiac polar map data for 15 visually normal patient images ( $18 \times 36$  segments displayed). All expressed in units of % of maximum activity. The (A) bootstrapped and (B) estimated local noise images averaged over all 15 patient studies. (C) The standard deviation of the mean images from a bootstrapped distribution for each patient representative of population and physiological cardiac variability. (D) One standard deviation representing the variability between the 15-different patient polar map images. (A)-(D) are on the same color scale with a maximum of 18.9%. (E) A mean polar map image with homogenous activity distribution.

local noise images that the basal posterior wall of the heart has the most camera noise while the apex has the least.

The standard deviation of the mean bootstrapped images (392 bootstraps) of the 15 patients (Figure 4.10C) contains minimal camera noise and approximates the image uncertainty due to differences in patient anatomy and physiology (5.5 to 17.4%). Figure 4.10D shows the standard deviation of individual patient images containing contributions from both camera noise and patient physiology (5.7 to 16.5%). The average patient image (Figure 4.10E) shows an approximately homogeneous distribution in the myocardium (60 to 83%).

## **4.4 Discussion**

### **4.4.1 Sensitivity variability in the field-of-view**

Our analytically calculated geometric sensitivity map replicated the sensitivity map measured by Kennedy *et al.* [33]. The calculated map of geometric sensitivity alone (Figure 4.1) is comparable with their point source measurement assuming negligible photon attenuation in air. In all cases, the largest variation in photon detectability in the FOV is predictably observed transaxially from patient left-anterior (high detectability closest to the centre of the detectors) to patient right-posterior (low detectability farthest from all detectors). It is thus important to position the patient as close as possible to the detectors to maximize sensitivity. The similarity of the magnitude of the effects of attenuation and geometric sensitivity on photon detectability reinforce the need to consider geometric sensitivity when assessing variable noise in the DNM530c.

### **4.4.2 Rapid Noise Estimation with the Projected Voxel (PV) Method**

The uncalibrated PV method (rPV) is based on a fundamental noise metric to estimate

the magnitude of the local image noise using a single reconstructed image and corresponding attenuation map. It accounts for the design of the camera, anatomy of the patient, the efficiency of the camera detectors, and the Poisson noise inherent to emission data. It does not account for dead pixels in the cameras detectors which will have reduced noise since their assigned pixel value is interpolated from neighbouring pixels. Nor does it account for the correlation of noise between image voxels. Since image noise is dependent on reconstruction methods which are not included in our method, I use a global scaling factor to directly calibrate the PV noise estimate. The PV method is highly dependent upon the ability of the reconstruction technique to produce an image that is a reasonable representation of the true object and thus the global calibration coefficients are dependent upon the choice of reconstruction algorithm, the number of iterations, priors, and filtering.

#### **4.4.3 Effect of Reconstruction Algorithm and Prior Strength on Image Noise**

##### **MAP-EM with OSL Green Prior**

The PV noise estimation method assumes each voxel source within the object or patient is independent and that the reconstructed image is a good representation of the true source. The number of counts projected from each voxel that are counted by the 19 pinhole detectors after geometric sensitivity and attenuation reductions are simply summed and used as the mean of a Poisson distribution. Thus, the noise for each voxel does not take into account the effects of image reconstruction and the noise correlations that the process can introduce. In addition, noise-suppressing priors that are incorporated in modern reconstruction algorithms have the potential to alter image noise characteristics. The empirical calibration of the PV method [Equation 16] must be

performed for each specific reconstruction protocol to implicitly correct for some of these effects. The calibration coefficients provided in Table 4.1 are specific to noise estimation for images reconstructed with 60 iterations of MAP-EM with a one-step-late Green's prior ( $\alpha=0.7$ ,  $\beta=0.5$ ). The PV method uses a single reconstructed image to assign the signal in each voxel as an estimate of the number of counts. The partial volume effects in the image typically reduce the values in the myocardium and will thus lead to an underestimate of the original signal strength. Because the single image is used as the mean underlying tracer distribution, the noise that is present in the image will be propagated into the image noise estimates. Nevertheless, the PV noise estimate is shown in Figure 4.2 to have strong correlation with the bootstrapped data with and without application of the empirical calibration function. The activity dependent calibration function is able to rescale the calculated noise estimate to account for the effects of image reconstruction and other limitations in the model assumptions to achieve high precision ( $\geq 83\%$ ) and minimal systematic error.

### **Maximum Likelihood Expectation Maximization (MLEM)**

The majority of our evaluations were performed for images reconstructed using the MAP-EM OSLG algorithm. When an MLEM reconstruction with resolution recovery is used for our phantom studies, we observe the well-known Gibbs artifact in the reconstructed image of the sphere. The artifact is also evident in the mean of reconstructed images obtained by bootstrapping, as well as in its corresponding noise magnitude image. Since the PV method does not model the effects of reconstruction, it does not accurately reproduce the noise effects associated with the Gibbs artifact and its performance is reduced for the MLEM case. Fortunately, priors used clinically suppress

the Gibbs artifact such that the reconstructed image more closely resembles the underlying object and the PV method does provide a reasonable noise estimate in these cases.

### **Attenuation Correction and Scatter Correction**

It is important to note that the PV noise estimation method generates the noise in an attenuation-corrected image and requires that image and the corresponding attenuation map to estimate the noise. I considered applying this approach to images reconstructed without AC and using an unattenuated forward projector. The resulting PV noise estimate correlates poorly with a bootstrapped measure of noise in the no-AC image. I hypothesize that this may be caused by the mismatch between the system model used in image reconstruction (which does not include attenuation) and the real system, but further investigation is needed to verify this.

While scatter correction is not used in current clinical protocols with the DNM530c camera, it is important for quantitative SPECT imaging protocols. In Figure 4.5, I observe that applying a modified dual-energy window scatter correction prior to reconstruction leads to a moderate increase in the noise magnitude but reduced the gradient in the noise and correlation length across the FOV. Like including attenuation correction, including scatter in the PV model or using the PV method to estimate the noise in AC and scatter corrected reconstructed images is expected to further improve the correlation between the noise estimated with the PV and bootstrapping methods.

### **Noise Correlation Length**

Since detection of areas of reduced perfusion depends not only on the noise magnitude

but on its correlation as well, it can be important to assess noise correlations. The PV method estimates the noise for each voxel independently, relying on the input reconstructed image to provide the voxel source strength. Thus, the PV method does not accurately represent the noise correlations between image voxels introduced by image reconstruction. This is seen in subtle differences between the bootstrapped and PV noise estimates. Using bootstrapping I see that the correlation length is  $\leq 1.7$  voxels, which equates to 6.8 mm and is roughly the thickness of the myocardial left ventricle (5.3-9 mm) in a middle-aged adult [57]. As such, the PV noise estimate is appropriate for comparing noise over distances similar to the myocardial wall thickness but is not ideally suited to evaluating fine detail of the noise texture.

#### **4.4.4 Applications**

While this method was developed for the DNM530c camera, the theory is broadly adaptable for estimating noise in other SPECT or positron emission tomography (PET) cameras given knowledge of the camera geometry or system matrix. Since PET and some conventional SPECT cameras already have onboard CT for routine attenuation correction, the PV method could be used to estimate image noise with minimal computational (1 min) cost. In conventional parallel hole SPECT, the effects of attenuation are unbalanced, particularly for 180-degree acquisitions, and will introduce local noise variability on the same order as does attenuation with the NM530c (similar to Figure 4.1B). In 3D PET acquisition, sensitivity varies somewhat in the transverse plane but has greater variation axially, leading to axially varying image noise and the magnitude of the attenuation effects are greater than in SPECT imaging. The image noise gradients may be smaller in PET and parallel-hole SPECT images than were observed in

the DNM30c, but our results suggest that they would still contribute substantially to the overall variability in the image (Figure 4.10).

A proposed application of the PV method is to provide physicians with a patient-specific map of the uncertainty values in myocardial perfusion images to increase their confidence in identification of cardiac defects. The PV method could also potentially be used to prospectively determine patient-specific injected activity or acquisition times based on set noise tolerance limits, a CT acquisition, and an assumed tracer uptake. The PV method could also be used retrospectively for rapid quality-assurance of acquired-image noise levels. Finally, PV noise estimation may be used retrospectively to develop weight- or BMI-based injected activity models to optimize injected dose or acquisition time.

#### **4.4.5 Variable noise in the myocardium and its potential impact**

The absolute image noise and the noise gradient are both larger in the patient cases than in the phantom for the same number of counts per voxel. This is attributed to the inhomogeneous activity distribution and increased attenuation in the patient cases compared with the phantom. Additionally, the patient images contain extra-cardiac activity inside and outside of the FOV whereas in the phantom study, all activity is contained inside the sphere. The added background activity may have increased the total noise magnitude in the patient images.

The noise attributed to imaging with a conventional parallel hole collimator varies across the FOV due to attenuation effects. The gradient of the pinhole geometric sensitivity of the DNM530c contributes approximately the same magnitude of effect. The combined effects result in a larger gradient of noise in the FOV of the DNM530c than in

a traditional camera. For the DNM530c, the clinical case with the largest variation in the PV estimated noise in the myocardium ranges from 3.7 to 17.7%; the smallest ranges from 2.0 to 7.7%. On average the PV estimated noise changes 5-fold across the length of the heart. As expected, the best (lowest) noise levels in an image are always observed in the apex of the myocardium. The worst (highest) noise is present in the basal-posterior wall. Occlusions of vessels supplying blood to the myocardial tissue restrict the flow of blood downstream. As such, defects are more likely in the apical region of the heart where noise is lowest. However, detectability in all regions of the heart must still be considered. Reduced perfusion can occur in regions which do not include the apex also, either through occlusion of branch (diagonal or marginal) arteries or due to intervention such as bypass surgery. In addition, I observe moderate noise variations (1.5-fold) from the septal to lateral walls. The need for an accurate detection of disease throughout the heart suggests a potential value to patient-specific noise estimates.

Clinicians typically consider variability between normal patients in the population when interpreting SPECT studies (Figure 4.10C). The addition of spatially variant noise (Figure 4.10A) due to camera geometry and attenuation leads to a visible increase in the noise across the length of the heart (Figure 4.10D). As the position of the heart within the camera FOV may change between studies and the attenuation effects are patient-specific, these effects will vary from study to study. Implications of this spatially-varying patient-specific noise contribution with respect to image interpretation are unclear as is the degree to which presentation of the PV-calculated patient-specific noise to the reader could impact interpretation. Both warrant further investigation.

## **4.5 Conclusions**

I have shown that image noise for a dedicated cardiac pinhole camera changes more than two-fold over the length of the heart. This has potential to impact the detectability of cardiac lesions. I have developed a quick, one minute, user friendly technique for calculating patient-specific image noise magnitude estimates which have been shown to be within 17% of truth in the 31 patient studies considered.

## **Chapter 5: Patient-specific protocols to standardize image noise**

*This chapter develops an imaging protocol that can be used to prescribe weight-specific radiotracer activities and/or acquisition times to standardize the level of image noise for all patients.*

*A reformatted version of this Chapter has been submitted for publication in the Journal of Nuclear Cardiology: Cuddy-Walsh, S. G., Clackdoyle, D. C., Renaud, J. M., Wells, R. G. “Weight-based protocols to standardize image noise for patient-centered CZT and conventional cardiac SPECT imaging,” 2018. The text of Section 5.1 has been modified to avoid repetition of Section 2.3.2 and to include additional detail. This work has been presented as conference abstracts.*

*Cuddy-Walsh, SG, Wells, RG, “Weight-based dosing for consistent image noise in dedicated cardiac SPECT,” Society of Nuclear Medicine and Molecular Imaging Annual Meeting, Denver, CO, June 2017. Published in J. Nuc. Med. 58 (Supplement 1), 28 (2017).*

*Cuddy-Walsh, SG, Wells, RG, “Getting the best image with the lowest dose: weight-based dosing in cardiac nuclear imaging” University of Ottawa Heart Institute’s Annual Research Day, Ottawa, ON, May 2017.*

## 5.1 Introduction

Patient-centered imaging is rapidly evolving to improve the optimization of image quality, radiation exposure, and patient comfort [8]. In cardiac nuclear medicine, image quality depends in part on the number of photons detected by the camera which is largely affected by attenuation in body tissues and camera design. To ensure all patients receive the same standard of care, large patients require higher administered activity or longer acquisition time than small patients to record sufficient photon counts. Current guidelines for myocardial perfusion imaging (MPI) with single photon emission computed tomography (SPECT) recommend protocols tailored specifically to the patient and imaging camera [8]. Patient-specific protocols adjust the activity and acquisition time based on patient weight or body mass index [69], [70], [72], [73]. They are designed to standardize the number of detected photons originating from cardiac tissue independent of patient habitus. However, it is well known that while the number of detected photons counts influences the level noise in an image, this can be altered dependent on the reconstruction algorithm used to produce the image. Image reconstruction algorithms which include noise suppression and resolution recovery have been shown to reduce or maintain image noise levels in reduced count studies [8], [92]. When designing clinical protocols, it is thus important to ensure the level of image noise is standardized with these weight-based activity-scan time (AST) protocols and to understand how the level of noise in an image changes for different activity levels, reconstruction parameters, and camera design.

The purpose of this work is to develop a method for deriving patient-specific activity-scan time (AST) protocols which can standardize the level of noise in MPI images for

conventional and multiple-pinhole cardiac SPECT cameras. It demonstrates the relationship between patient habitus and image noise for two SPECT cameras with specific reconstruction parameters and highlights the differences in these relationships between cameras. It also aims to highlight the necessity for considering the reconstruction parameters in addition to camera sensitivity when designing these protocols.

## **5.2 Materials and Methods**

### **5.2.1 Study Design**

SPECT images were retrospectively reprocessed and evaluated for 101 patients (45 female) who were referred for MPI with a conventional parallel-hole SPECT/CT camera (Infinia Hawkeye4, GE Healthcare, Haifa, Israel) and who were also subsequently imaged with a cardiac multiple-pinhole cadmium zinc telluride (CZT)-based camera (DNM530c; Discovery NM530c, GE Healthcare, Haifa, Israel). Images were originally acquired with a dual camera imaging protocol when the DNM530c was installed at the University of Ottawa Heart Institute (UOHI) and were recorded in the UOHI cardiac imaging research database. This retrospective study was approved by the Ottawa Health Science Network Research Ethics Board and the Carleton University Research Ethics Board-B (Protocol 20170769-01H). Patient demographics and coronary artery disease risk factors are summarized in detail in Table 5.1.

### **Training Set**

From the available studies, a training set of images from 43 patients was used to develop the patient-specific protocols. It was chosen to include at least 3 patients of each gender in each of the following body weight categories: <50 kg (female only), 50-65 kg,

**Table 5.1 Patient Characteristics and Medical History for training and testing of an image noise standardization method.**

Characteristic	Training Set			Test Set		
	Both (n = 43)	Male (n = 23)	Female (n = 20)	Both (n = 58)	Male (n = 33)	Female (n = 25)
Age [years]	61 ± 10 (40 – 81)	60 ± 9 (41 – 76)	61 ± 12 (40 – 81)	62 ± 11 (37 – 84)	61 ± 11 (37 – 84)	62 ± 10 (47 – 86)
Body Weight [kg] <sup>b, d</sup>	83 ± 21 (45 – 128)	87 ± 17 (57 – 118)	79 ± 24 (45 – 128)	82 ± 14 (54 – 114)	86 ± 13 (66 – 114)	76 ± 13 (54 – 114)
Height [cm] <sup>d</sup>	167 ± 10 (147 – 185)	173 ± 7 (160 – 185)	161 ± 9 (147 – 175)	171 ± 10 (145 – 193)	177 ± 7 (160 – 193)	163 ± 7 (145 – 175)
Body Mass Index (BMI) [kg/m <sup>2</sup> ] <sup>b</sup>	30 ± 7 (17 – 52)	29 ± 5 (20 – 38)	31 ± 8 (17 – 52)	28 ± 4 (22 – 39)	28 ± 4 (22 – 35)	29 ± 4 (22 – 39)
Current Smoker [%]	7	9	5	10	12	8
Ex-Smoker [%]	40	52	25	40	41	38
Hypertension [%]	67	74	60	50	44	58
Diabetes [%]	21	26	15	10	9	12
Hyperlipidemia [%]	63	70	55	43	41	46
Family History [%]	49	39	60	38	32	46
Infarct [%] <sup>c</sup>	16	22	10	2	0	4
Previous percutaneous coronary intervention [%] <sup>c</sup>	21	30	10	0	0	0
Previous coronary artery bypass graft [%] <sup>c</sup>	12	22	0	0	0	0
Valvular Disease [%]	5	4	5	0	0	0
Normal MPI Result [%] <sup>a, c</sup>	81	65	100	100	100	100

<sup>a</sup>Normal based on clinical evaluation of rest/stress, gated/ungated myocardial perfusion imaging (MPI) studies by a board-certified cardiologist.

<sup>b</sup>The variance of the weight and BMIs of patients in the training set is significantly greater than for the test set. The average weights and BMIs are not significantly different between the two sets.

<sup>c</sup>Compared with the test data set, the training data set contains a significantly greater fraction of patients with a history of infarct, percutaneous coronary intervention, and coronary artery bypass graft as well as significantly more abnormal MPI results.

<sup>d</sup>Body weight and height are significantly greater for male patients than female patients for both the training and test sets.

66-80 kg, 81-95 kg, 95-110 kg, and >110 kg (2 females and 3 males). The average body weight of patients between 60 and 85kg was  $76 \pm 8$  kg. Patient images were preferentially selected if a board-certified cardiologist reported normal myocardial perfusion. An additional 5 male patients with abnormal results were included to meet the quota of at least 3 males in each of the five highest weight categories.

### **Test Set**

A test set of images from the remaining 58 patients was used to evaluate the efficacy of the protocols. All patients in the test set had normal MPI results. While the average patient weight and BMI was not significantly different from the training set, the range of values was significantly smaller for the test set than for the training set.

### **5.2.2 Image Acquisition**

All patients were imaged according to ASNC guidelines using a one-day full-dose rest-first rest/stress protocol except for three patients (2 training and 1 test) who were imaged according to a two-day rest/stress protocol [93]. To avoid the influence of residual activity and reduce the chance of including images with perfusion defects, this study reprocessed and analyzed only rest images (though stress images were acquired with administered activities ~3 times higher than rest). Imaging was performed following a single injection of Tc-99m Tetrofosmin with the first camera (Infinia if available) at an average time of 58 minutes with a standard deviation of 18 minutes and with the second camera at  $85 \pm 22$  minutes post-injection. Administered tracer activity for rest imaging with the one-day protocol was  $347 \pm 29$  MBq ( $9.4 \pm 0.8$  mCi) with a range of 309 – 440 MBq (8.4 – 11.9 mCi) for patient body masses ranging from 45 – 118 kg. (Activity was approximately three-times higher for three >110 kg patients imaged with the two-day

protocol.) The administered activity decayed to  $311 \pm 28$  MBq ( $8.4 \pm 0.8$  mCi) by the time of the first image acquisition. All calculations in this Chapter and in Chapter 6 are performed with the activity decay-corrected to the time of imaging.

SPECT projection data were acquired on the Infinia camera with dual-heads in L-configuration and rotated  $90^\circ$  in  $3^\circ$  steps (60 projections total) over an acquisition duration of 12.8 minutes (25.6 seconds per step). A static acquisition with the DNM530c was used to obtain 19 emission images (projections) over a duration of 8 minutes, 5 minutes of which were used clinically.

### **5.2.3 Image Reconstruction**

Vendor software (Xeleris Myovation 4.0, GE Healthcare) was used to produce attenuation maps for the Infinia Hawkeye4 SPECT/CT acquisitions. Projection data were reconstructed using our clinical parameters of 2 iterations of ordered-subset expectation maximization (OSEM) with 10 subsets for both non-attenuation corrected (NC) and attenuation corrected (AC) images. No post-filtering was applied.

DNM530c emission data were reconstructed using vendor software (Xeleris BatchRecon, GE Healthcare). NC images were reconstructed as per our clinical protocol with 40 iterations of maximum a posteriori expectation maximization (MAP-EM) and a one-step-late Green's (OSLG) prior ( $\alpha = 0.51$ ,  $\beta = 0.3$ ). An attenuation map was generated by manually aligning (see Appendix A) each patient's CT from the Infinia Hawkeye4 with their reconstructed NC DNM530c image using vendor software (Xeleris Myovation 4.0, GE Healthcare). Reconstructions with AC were performed using 60 iterations MAP-EM with an OSLG prior ( $\alpha = 0.7$ ,  $\beta = 0.5$ ) as per the default manufacturer specified protocol. No post-filtering was applied.

#### 5.2.4 Camera-dependent Photon Sensitivity

As done in AST protocols which are standardized based on the number of detected photon counts [72], [94], I calculated the attenuated sensitivity for each camera as the number of detected photon counts per megabecquerel per minute for different patient weights and assessed the relationship between attenuated sensitivity and patient weight. For each camera and patient, I normalized the measured number of photon counts in regions-of-interest around the heart  $C_{meas}$  in all projections of the original data set (19 for the DNM530c or 60 for the Infinia) using the decay corrected tracer activity  $A$  [MBq] and scan time  $T$  [min].

$$C_{norm} = \frac{C_{meas}}{A \cdot T_{scan}} [\text{counts} \cdot \text{MBq}^{-1} \cdot \text{min}^{-1}] \quad (18)$$

Assuming that the relationship between patient habitus and biological uptake of administered activity is linear,  $C_{norm}$  provides a metric for comparing habitus-dependent differences in the sensitivity for detecting photons due to differences in positioning relative to a specific camera, camera design, and tissue attenuation. Note that though  $C_{norm}$  is a relative measure, the uncertainty in this measure will depend upon the absolute number of detected photon counts and thus the AST.

#### 5.2.5 Noise Calculation

For this work, image noise was used as a quantitative index of image quality. To obtain one statistical replicate, each pixel in a projection set was resampled by assigning a value sampled from a Poisson distribution centered about the original pixel value [2]. This was repeated for all pixels in a projection set to obtain a replicate projection set. This process was repeated to obtain the desired number  $N$  of projection sets. All projection sets were then reconstructed (as specified in the previous section) to obtain  $N$

replicate images. Image noise was calculated using Equation 5 from Chapter 4 as one standard deviation over all  $N$  images. Note that approximately 400 replicates would be required for this study was selected to obtain an estimate of noise within 5% of that obtained for 1000 replicates (Appendix B). Since vendor-software allowed images to be reconstructed in batches of up to 98 images, I used  $N = 392$  replicates to simplify processing.

For each patient, the average uptake ( $\bar{F}$ ) and noise images ( $\sigma$ ) were converted to 17-segment cardiac polar maps. The values in the uptake and noise polar maps were normalized to the maximum uptake segment value. To avoid introducing errors, I included only results for segments of the cardiac polarmap which were clinically normal (with greater than 70% of the maximum uptake). Thus, the mean noise in the heart was calculated from the average over all segments with greater than 70% uptake.

## **5.2.6 Developing a Patient-Specific Tracer Activity and Scan Duration Formula**

### **Relationship between image photon counts, image noise, and body mass**

To develop a formula relating image noise to decay corrected administered activity  $A$  in  $MBq$ , scan time  $T$  in minutes, and body mass (weight)  $W$  in kilograms, I consider the elements that might influence their relationship. As the heart mass is roughly proportional to lean body mass, I assume that the percentage of administered activity taken up in the heart can be considered relatively independent of weight. Then, approximating the human body as a water-filled sphere, body weight is proportional to the volume of a sphere which increases as the sphere's radius cubed. If the heart is assumed to be at the center of the sphere, then the attenuation length is equal to the sphere's radius and the number of detected photon counts is proportional to the negative exponential of the cubic root of

weight. The noise in an image can be approximated by the square root of the number of detected counts. Thus, the noise in units of counts is related to weight by an exponential function. However, image noise is generally considered as a percentage of the detected (or reconstructed) photon counts. Dividing the exponential noise function by the exponential detected photon counts function results in another exponential function. With these assumptions, the noise is seen to change rapidly as a function of weight for weights < 30 kg, but for weights in the clinical range of 40 to 150 kg, the change in noise is much slower and is well approximated as a linear change with weight. Thus in the clinical range of weights, it is expected the percentage image noise will increase linearly with increasing patient body mass given a fixed administered activity. Then, assuming that the number of detected photon counts is proportional to the injected activity, percentage image noise will be approximately proportional to one over the square root of the variable activity and scan time such that

$$\sigma [\%] \propto \frac{W}{\sqrt{A \cdot T}}. \quad (19)$$

As such I expect fits of experimental data to be of the form

$$\sigma [\%] = k_1 \cdot \left(\frac{A \cdot T}{W^2}\right)^{-0.5} + k_2 \quad (20)$$

where  $k_1$  and  $k_2$  are camera-dependent (to account for differences in geometric sensitivity and attenuation path length) and image reconstruction parameter-dependent calibration coefficients. Note that that this relationship with weight is based on the approximation of a patient as a sphere, non-uniform body fat distribution alters the relationship between weight and noise such that the appropriate power to assign the weight term is not known. To simplify the function for ease of use clinically, I set power

on the weight term equal to 1 to yield a linear relationship between  $A \cdot T$  and  $W$ :

$$\sigma [\%] = k_1 \cdot \left(\frac{A \cdot T}{W}\right)^{-0.5} + k_2. \quad (21)$$

### **Calibration of a Patient-Specific Activity-Scan Time Formula**

To determine the correct calibration coefficients for Equation 21, I required a dataset spanning different levels of image noise and  $\frac{A \cdot T}{W}$  values. For the training set of patient images, the number of photon counts in projection data were scaled to simulate projection sets with different levels of image noise, Poisson resampled to obtain different noise replicate images, these reconstructed, and the image noise calculated. Scaling to different noise (photon count) levels assumed that the number of detected photon counts scaled linearly with the radiotracer activity and acquisition duration (activity-scan time, MBq·min). Infinia acquisitions were scaled by factors of 1, 1/2, and 1/4 and the DNM530c acquisitions were scaled by factors of 2, 1, and 1/4. A scaling factor of 1 refers to resampling the original data set; 5 min of 8 min for the DNM530c and 12.8 min for the Infinia. In the case of the DNM530c, a scaling factor of 2 oversampled the data to obtain a projection set with a number of photon counts similar to 10 min of acquisition from 8 min of real data.

The following method was used to obtain  $k_1$  and  $k_2$  for Equation 21 specific to images reconstructed with and without attenuation correction for each of the DNM530c and Infinia cameras. For each of the 43 patients and 3 simulated noise levels, the calculated image noise  $\sigma$  [%] was plotted in relation to  $A \cdot T/W$  and fits were performed using linear regression independent of gender, or with separate fits for female and male patients. While I primarily used patient weight as a measure of habitus for ease of clinical

use, patient-specific protocols were also considered using body mass index to accommodate different clinic protocols and are presented in Appendix C.

Determining coefficients for different female-, male-, and non-specific gender coefficients, different reconstruction parameters (NC and AC), and different cameras accommodate for potential differences in the noise properties and attenuation patterns arising from distinct photon detection sensitivity, detector layouts, reconstruction parameters, and patient physiology. Rearranging Equation 21, provides a single scaling factor with units of  $(MBq \cdot \text{min})/kg$  in Equation 22 for a patient-weight-specific AST associated with a fixed level of image noise  $\sigma$ .

$$A \cdot T = \left( \frac{k_1}{\sigma - k_2} \right)^2 \cdot W \quad (22)$$

### 5.2.7 Validating a Patient-Specific Tracer Activity and Scan Duration Formula

A test set of patient images was used to evaluate the accuracy of using this formula to standardize image noise. Noise images were computed using two protocols: constant (DNM530c: 330 MBq and 5 min; Infinia: 298 MBq and 12.8 min) and weight-based AST (DNM530c: 22.45 MBq·min/kg; Infinia: 50.28 MBq·min/kg for all patients, 58.43 MBq·min/kg for females, and 46.58 MBq·min/kg for males) products. These tracer activities were defined as the decay corrected activity at the time of acquisition. I applied scaling factors to achieve AST products prescribed by Equation 22 using NC combined-gender coefficients  $k_1$  and  $k_2$  to standardize noise levels to  $\sigma = 6.1\%$  and  $16.3\%$  (average  $\sigma$  for 60-85 kg patients) for the DNM530c and Infinia cameras respectively. With both fixed- and patient-specific AST approaches, re-scaled projection data was processed as specified in Section 5.2.5 to calculate image noise. The relationship between image noise and patient weight was evaluated for each case to determine the effect of patient-specific

AST protocols.

### 5.2.8 Statistical Analysis

Patient characteristics (Table 5.1) were inspected for significant differences between male and female datasets or training and test datasets using t-tests for continuous measures such as weight, height, BMI, and age. F-tests were used to compare the variances of these datasets. Chi-squared tests and Fisher Exact tests (when any value was less than 5) were used to detect differences in medical history of patients between the training and test datasets. All tests were performed at the 95% confidence level.

Linear regression was used to determine fit coefficients for Equation 21 and for the relationship between  $C_{norm}$  and patient weight at the 95% confidence level. To evaluate the developed weight-based protocols in Section 5.2.7, the relationship between image noise and patient weight was also evaluated using linear regression at the 95% confidence level ( $p < 0.05$ ). Slopes [% noise per kg] significantly different than zero indicate a weight-dependence on percent image noise. Multilinear regression was performed as secondary analysis to evaluate the relationship between image noise in units of photon counts and two variables: the maximum polarmap segment [counts] and weight [kg].

## 5.3 Results

### 5.3.1 Camera-dependent Photon Sensitivity

As expected, the  $C_{norm}$  for both cameras decreases with increasing patient weight (Figure 5.1). The average value of  $C_{norm}$  for the DNM530c is  $403 \pm 148$  photon counts per MBq·min and for the Infinia is  $118 \pm 38$  photon counts per MBq·min. A linear fit of the ratio of  $C_{norm}$  for the two cameras is given by  $\frac{C_{norm\ CZT}}{C_{norm\ INF}} = -0.002 \cdot W + 3.6$  suggesting that the AST should be  $\sim 3.6$  times higher for the Infinia to detect the same

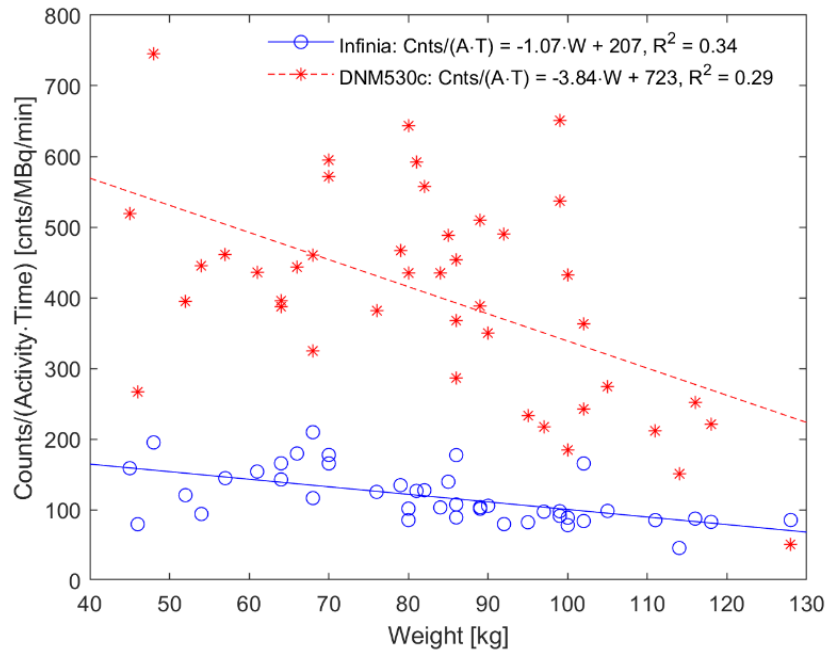


**Figure 5.1 Impact of patient weight due to attenuation on photon sensitivity (Equation 18) for two SPECT cameras. Counts were reported as the sum of all counts in regions of interest around the LV in projection space. The radiotracer activity [MBq] was decay corrected to the start of the image.**

number of cardiac photon counts.

### 5.3.2 Developing a Patient-Specific Tracer Activity and Scan Duration Formula

Weight-based activity formulas (Equation 21) fit the image-noise data with adjusted Pearson's R-squared values of 0.85 to 0.89 for the Infinia and the NC DNM530c images, and values of 0.62 to 0.64 for the AC DNM530c images (Figure 5.2). The reduced R-squared values for the AC DNM530c images may be associated with the noted increase in the noise gradient (Figure 6.5), however the exact cause is unknown and would require further investigation. Gender-specific and combined fit coefficients are summarized in Table 5.2. The noise versus weight gradient for fixed AST images is 2-3 times steeper for the DNM530c compared with the Infinia camera. This means that comparing NC protocols between the two cameras, even adjusting the scan time for the Infinia to 3.6 times longer than the DNM530c (5 min), for a decay corrected activity of 330 MBq, the noise in the Infinia image (13.4%) is 2.1 times higher than in the DNM530c image

(6.4%) of an 80 kg patient. For AC protocols, the noise is 1.8 times higher for the Infinia image (12.5%) compared with the DNM530c image (7.0%) for the same patient. Even noise in images acquired using the same camera can be altered by different reconstruction parameters. As expected, attenuation correction in standard OSEM reconstruction increases noise in the Infinia images by 1.07-fold compared with NC. The application of a heavier prior in DNM530c AC than in the DNM530c NC reconstruction leads to 0.91 times lower noise.

### **5.3.3 Validating a Patient-Specific Tracer Activity and Scan Duration Formula**

#### **Impact on the Relationship between Image Noise and Weight**

As expected, with constant AST protocols, the average image noise increases with increasing patient weight for both cameras (Figure 5.3). Indeed, for the DNM530c camera, the slopes were 0.05 ( $p = 0.00002$ ) and 0.03 ( $p = 0.0001$ ) for NC and AC images respectively; for the Infinia camera, the slopes were 0.05 ( $p = 0.01$ ) and 0.07 ( $p = 0.0001$ ). The units of all slopes were % noise per kilogram. Using a weight-based AST with Equation 22, based on the gender-independent fits shown in Figure 5.2, the slopes of the relationship between weight and noise are not significantly different from zero for the DNM530c camera (slope = 0.007,  $p = 0.56$  for NC and slope = -0.003,  $p = 0.73$  for AC) but still significantly differ from zero (slope = -0.03,  $p = 0.046$  for NC and slope = -0.03,  $p = 0.050$  for AC) for the Infinia camera. Using the gender-specific NC coefficients for the Infinia images, eliminates the patient weight dependence of the average image noise for both NC and AC images (slope = -0.002,  $p = 0.88$  for NC and slope = -0.003,  $p = 0.85$  for AC).

To support the evaluation of image noise normalized to the maximum number of

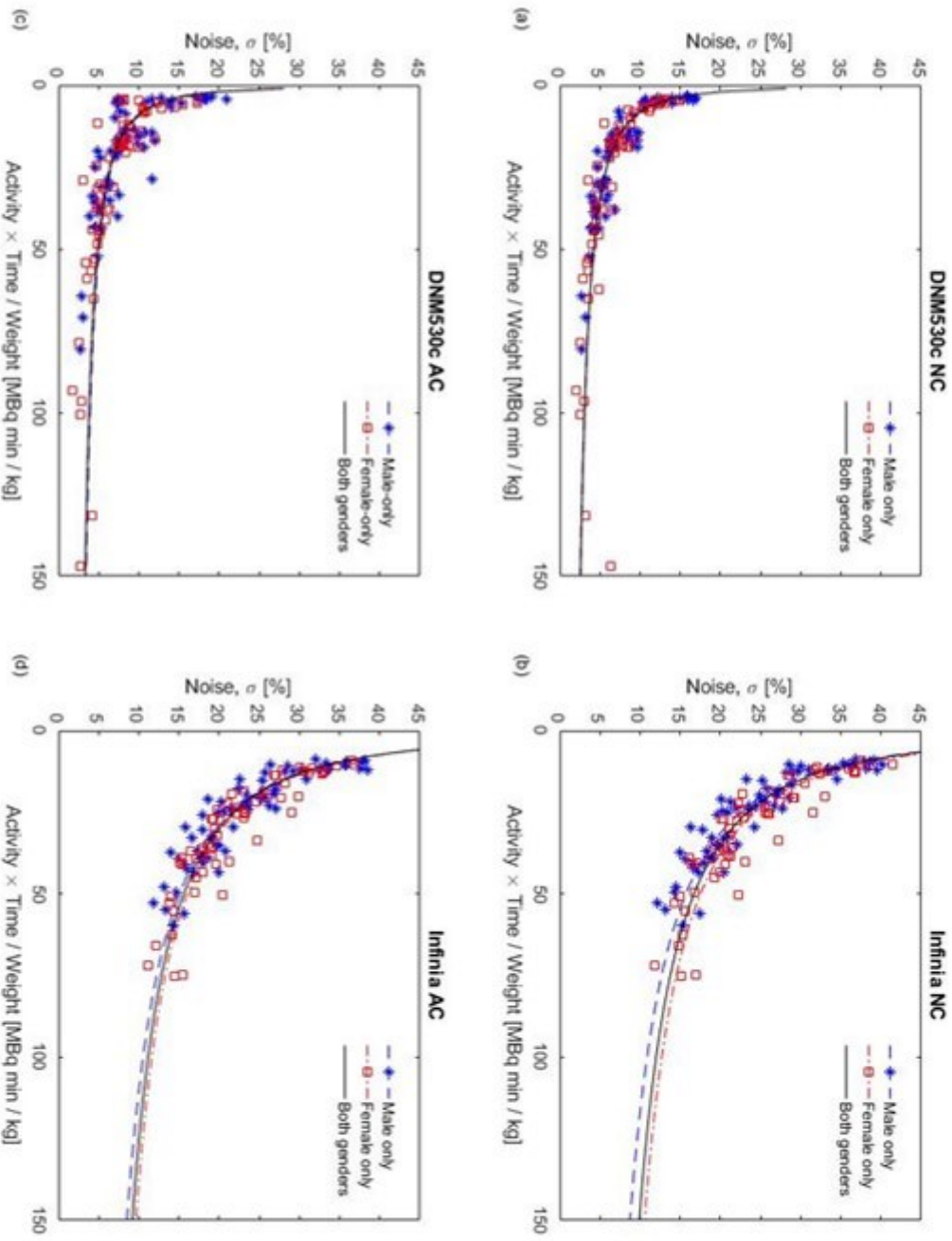


Figure 5.2 Plots to determine the relationship between average image noise and activity  $\times$  scan time (AST) per weight for two cameras (GE Discovery NM530c and GE Infinia Hawkeye) for images with (AC) and without (NC) attenuation correction. Values are plotted for 43 patients (20 female). Noise values are plotted for the DNM530c images for 2, 1, and 1/4 AST, and for the Infinia images for 1, 1/2, and 1/4 AST. Plots are fit with Equation 21 and results are reported in Table 5.2.

**Table 5.2 Weight-based administered activity and acquisition scan time formula coefficients<sup>a</sup>, confidence intervals, and Pearson's r-squared values.**

	Gender	$k_1$	$k_2$	$adj. R^2$
<u>INFINIA<sup>b</sup></u>				
NC	Both	115.2 (108.9, 121.6)	0.053 (-1.2, 1.3)	0.86
NC	Female	116.7 (104.2, 129.2)	1.033 (-1.6, 3.6)	0.85
NC	Male	116.3 (105.4, 127.1)	-0.7405 (-3.2, 1.7)	0.87
AC	Both	108.5 (102.9, 114.2)	-0.0725 (-1.2, 1.0)	0.87
AC	Female	106.7 (96, 117.5)	0.9286 (-1.3, 3.2)	0.87
AC	Male	109.7 (98.86, 120.5)	-0.4198 (-2.9, 2.0)	0.86
<u>DNM530c<sup>c</sup></u>				
NC	Both	28.25 (26.6, 29.9)	0.1379 (-0.3, 0.6)	0.87
NC	Female	27.66 (25.1, 30.2)	0.3692 (-0.3, 1.1)	0.89
NC	Male	27.95 (25.4, 30.6)	0.2689 (-0.5, 1.1)	0.87
AC	Both	26.56 (23.0, 30.1)	1.172 (0.1, 2.2)	0.64
AC	Female	25.59 (20.5, 30.7)	1.241 (-0.1, 2.6)	0.64
AC	Male	26.83 (21.6, 32.1)	1.243 (-0.4, 2.9)	0.62

<sup>a</sup>Coefficient values determined from non-linear regression in Figure 5.2 are for use in Equation 22 for calculating patient-specific activity-scan time

<sup>b</sup>INFINIA refers to the Infinia Hawkeye4 SPECT/CT, GE Healthcare, Haifa, Israel

<sup>c</sup>DNM530c refers to the Discovery Nuclear Medicine 530c SPECT camera, GE Healthcare, Haifa, Israel

photon counts (max counts) in a polarmap segment as a function of weight, multilinear regression of unnormalized (units of reconstructed photon counts) noise values as a function of patient weight and max counts was performed. In the multivariable analysis, the coefficient for max counts significantly ( $0.08, p=10^{-14}$ ) contributed to the fit as did the intercept ( $16.13, p = 10^{-7}$ ) while the coefficient for weight did not ( $-0.013, p = 0.51$ ) for images obtained using the fixed AST protocol. However there is substantial colinearity between the variables weight and max counts. Indeed, max counts can be modelled as a linear function of weight with the weight coefficient ( $-2.61$ ) having a p-value of 0.001 and with an adjusted Pearson's  $R^2 = 0.36$ . Additionally, when weight-specific AST protocols are used, the multivariable analysis showed the non-significant weight coefficient to be reduced ( $-0.006, p = 0.68$ ), the intercept to decrease to  $15.78 (p = 10^{-10})$  but the max counts coefficient to remain unchanged ( $0.08, 10^{-15}$ ). The max counts also

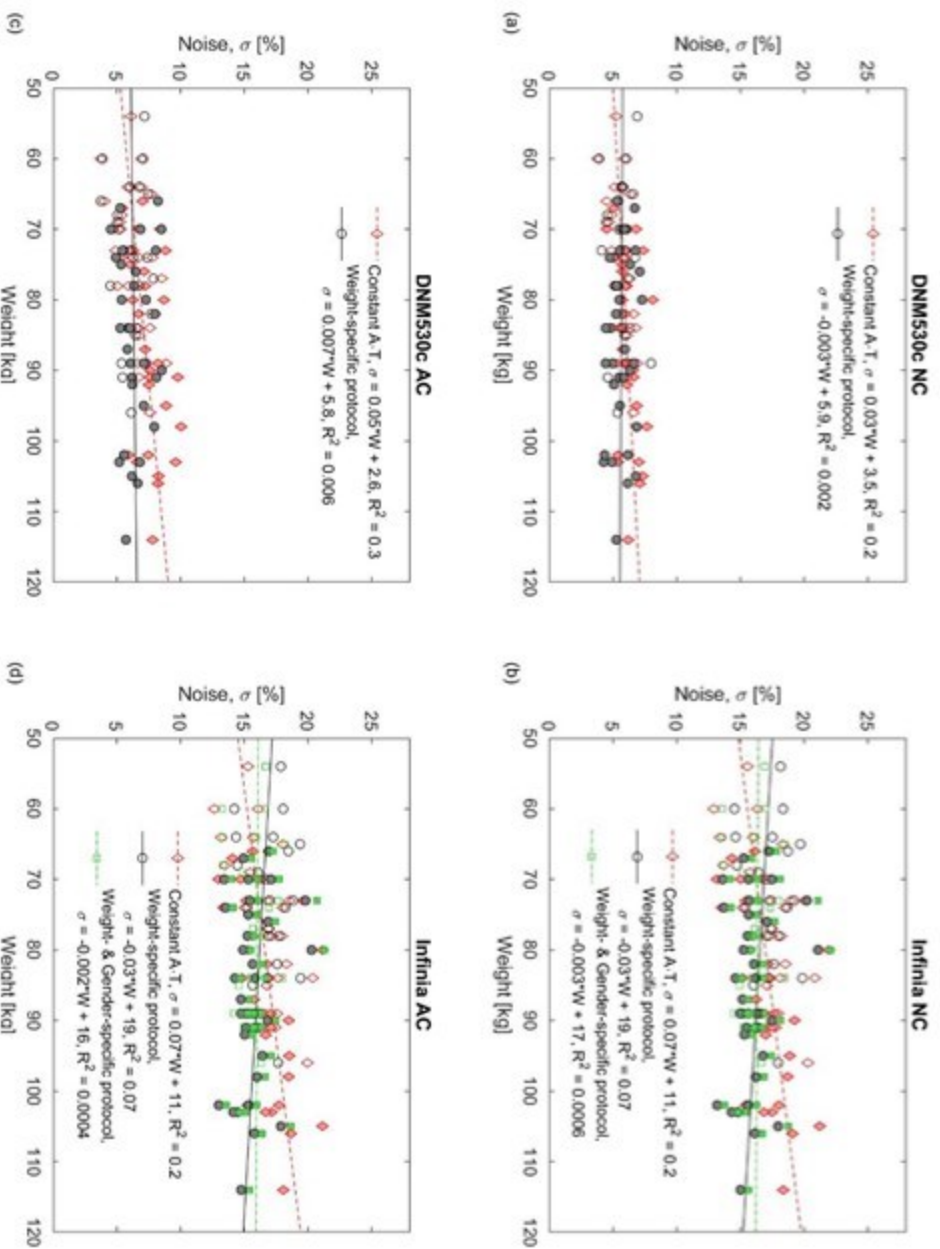
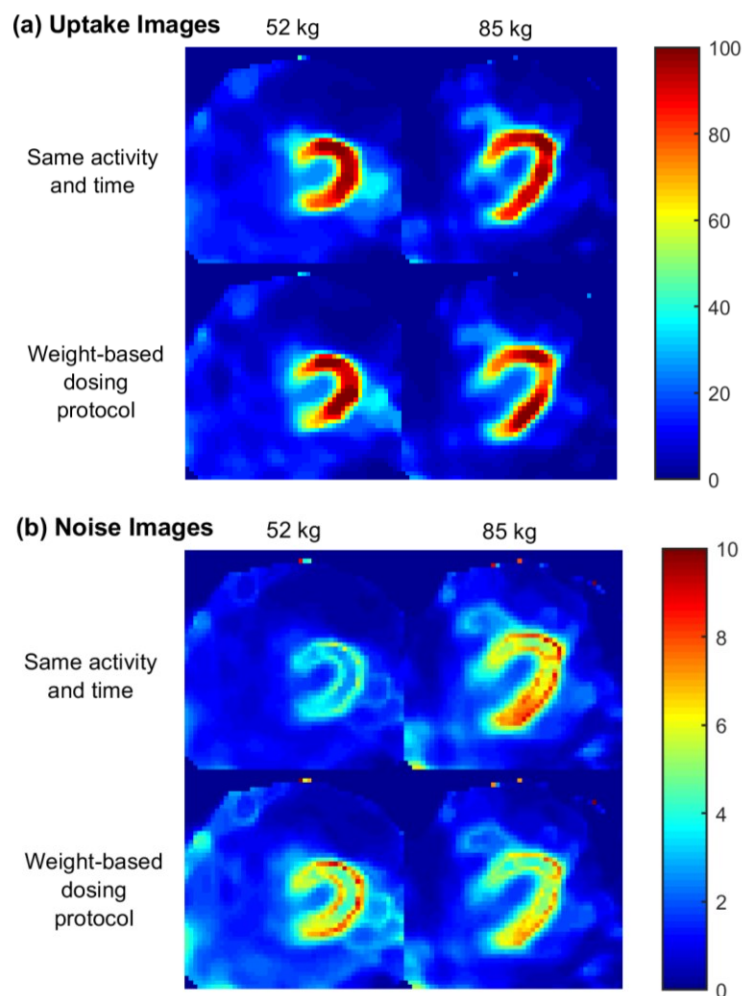


Figure 5.3 Average image noise [%] plotted as a function of patient weight [kg] without (red-diamond) and with (black-circle or green-square) weight-based patient-specific activity-scan time for the DNM530c and Infinia SPECT cameras: (red-diamond) constant activity-scan time ( $A \cdot T$ ) product for all patients, (black-circle) patient-specific  $A \cdot T$  determined using gender neutral NC coefficients in Equation 22 for a fixed image noise of  $\sigma = 6.1\%$  for the DNM530c and  $16.3\%$  for the Infinia, (green-square) patient-specific  $A \cdot T$  using male- or female-specific NC coefficients to achieve constant image noise of  $16.3\%$  for the Infinia camera. Open and filled markers represent female and male patients respectively. Linear fits of all points for each case are provided in the figure legends.

becomes constant with respect to weight (weight coefficient:  $-0.27$ ,  $p = 0.70$ ). This indicates that for a fixed AST protocol, the noise remains dependent on weight through the weight-dependence of the max counts. However, while weight is not statistically significant in the multilinear regression for fixed AST protocol, using a weight-based protocol is statistically demonstrated to remove the weight dependence for image noise and max counts.



**Figure 5.4** For the DNM530c camera, (a) one transaxial slice (cropped to  $50 \times 50$  voxels from  $70 \times 70$ ) through the left ventricle of two uptake images reconstructed without attenuation correction. The corresponding noise images are also shown in (b). Images are shown for two patients (52 and 85kg) reprocessed retrospectively to simulate (i) a fixed AST protocol, or (ii) a weight-based AST protocol designed to achieve an average cardiac image noise of 6.1%. Both colour bars are scaled as a percentage of the maximum voxel value for each image in (a). Note: the heart of the 85 kg patient extends farther to the bottom-left of the field-of-view in a region of reduced photon sensitivity.

## Visual Evaluation of Image Quality

As depicted in example uptake images and noise images in Figure 5.4, using a weight-adjusted protocol compared with a constant AST protocol improves (lowers) the image noise for the >76-kg patient and increases noise to the chosen level for the <76-kg patient to produce images of similar quality.

## 5.4 Discussion

While several previous studies have developed weight or BMI-based protocols for cardiac SPECT based on visual assessment of image quality or quantification of detected photons in projection space [69]–[72], [74], [75], [95], this work is the first quantitative assessment of reconstructed image noise to validate a weight-based activity-scan time adjustment formula. Once a noise level has been chosen, a linear relationship between the activity-scan time and weight similar to those previously developed [69], [70] can be used to standardize both the number of photon counts and image noise for patients of different weights.

Though the thrust of this work is to standardize reconstructed image noise, I first relate this to the sensitivity limitations of specific cameras with respect to patient habitus and camera design. As has been previously observed [24], the DNM530c is approximately 3.4-3.6 times more efficient requiring only 5 minutes of acquisition to detect the same number of photons as 17.1 minutes with the Infinia camera for a fixed injected activity. The small slope (-0.002 per kg) of the Infinia to DNM530c camera count sensitivity ratio suggests that raw photon counts for both cameras are affected by patient weight in a similar way.

It is well known that the level of noise and lesion detectability in a reconstructed

image depends on reconstruction methods (algorithm, number of iterations, priors, resolution recovery, and filtering) in addition to the number of photons detected [8], [66], [92], [96]. While measuring myocardial photon counts in projection space is simpler to do, our approach includes the effects of reconstruction on the noise character of patient images. Indeed, even if the number of detected photon counts from a specific patient is the same for both cameras, the noise is higher in Infinia images than in DNM530c images due to the incorporation of noise-suppressing priors and collimator modelling in the DNM530c reconstruction. This highlights the importance of reconstruction-technique selection when trying to match image quality between cameras or when moving towards lower dose protocols (and introducing heavier priors for lower count studies). Similarly, the noise characteristics changed when I used different reconstruction approaches (NC vs. AC) for the same patient and camera with and without the use of priors. Thus patient-specific activity-scan time protocols can standardize image quality for the same reconstruction algorithm but need also to be camera- and reconstruction parameter-specific.

For a specific camera and set of reconstruction parameters, it is not expected that Equation 21 will be used in regular practice. Rather a clinical operating noise level would be chosen that produces diagnostic images for average patient size and Equation 22 would be used to provide patient-specific imaging protocols and patient-specific dose justification (such as 22.45 MBq·min/kg for a noise level of 6.1% with the DNM530c or 50.28 MBq·min/kg for a noise level of 16.3% with the Infinia).

As demonstrated in Figure 5.3, fixed activity-scan time protocols with both cameras lead to images with noise levels with a significance weight-dependence. This weight

dependence is not significant for images acquired with a weight-specific protocol for the DNM530c camera, and with a gender- and weight-specific protocol for the Infinia camera. Statistically, the addition of gender specificity in imaging protocols for the Infinia camera achieves a more standardized noise level than weight-alone-based protocols however it is not known if the difference is clinically significant. The difference in results with and without gender considerations is small and thus may not warrant the 25% increase in AST prescribed with the female protocol compared with the male protocol (58.43 MBq·min/kg for females vs. 46.58 MBq·min/kg for males).

To further improve the patient-specificity of imaging protocols, future investigations could include using CT images to prospectively estimate patient attenuation. Combined with camera sensitivity maps, a patient-specific CT-based attenuation could also be used to optimize the prescribed tracer activity (if the CT scan is acquired well in advance of the SPECT) or acquisition time (for CT scans acquired immediately prior to SPECT) with greater precision than weight or BMI-based methods.

#### **5.4.1 Clinical Implications**

This work demonstrates a method that can be used to standardize the level of noise in cardiac images. The clinical decision maker needs only to calculate the level of noise for an image that they deem to have adequate quality for a specific camera, patient weight, and image reconstruction parameters. An AST protocol can then be used prospectively to obtain the same level of noise for images in different patients, imaged on different cameras, or with different reconstruction parameters. Once the noise level has been established, regular clinical workflow would include a quick calculation of the required radiotracer activity or scan time.

With a standardized (expected) noise level established and the addition of post-processing to evaluate the level of noise in each image, another clinical advantage would include the ability to identify erroneous results. For instance, a higher level of noise throughout an image might suggest balanced ischemia which may otherwise be undetected by relative perfusion imaging.

#### **5.4.2 Limitations**

This work does not provide information regarding the minimum required image noise level for adequate image quality. For a chosen noise level, the technique standardizes both the image noise and number of detected photon counts which previous observer studies [69], [70], [72] have shown to produce reconstructed images of a similar quality. This work provides a method for quantitatively comparing image noise between imaging systems and parameters. This would allow clinics to standardize image noise to their preferred level for all patients within their imaging suite.

The weight-based formulas developed in this work are specific to SPECT image rest protocols with the evaluated cameras, reconstruction parameters, and  $^{99m}\text{Tc}$ -tetrofosmin radiopharmaceutical. For stress or prone imaging protocols or for different cameras/reconstruction parameters, the weight-based formulas should be re-derived. I also note that since these formulas were developed for patient weights ranging from 45 to 118 kg (and one 128 kg), caution should be used if extrapolating for patient weights outside of this range. Finally, the precision of this study was limited by the lack of information about the residual activity in the syringe following injection. Assuming approximately 11% tracer-syringe retention [97], an administered activity of 347 MBq may have been overestimated by 38 MBq. This should be considered to avoid

overestimation of the necessary activity-scan time.

### **5.4.3 New Knowledge Gained**

This work develops the first patient-specific MPI protocols based on a quantitative measure of reconstructed image noise. It provides continuous formulae to prospectively prescribe patient-specific activity and scan time to standardize image quality for all patients.

## **5.5 Conclusions**

Solid-state multi-detector cardiac SPECT cameras offer decreased image noise compared with conventional SPECT cameras. An increase in image noise is observed for heavier patients on a given camera and thus patient-specific protocols are necessary for optimal patient care. Weight-based activity-scan time protocols for SPECT imaging have been presented that standardize the reconstructed image noise to support patient-centered imaging. This work also reinforces the need for decision makers to consider reconstructed image quality and not detected photon counts alone when designing clinical protocols.

## **Chapter 6: Intra-cardiac noise gradient in pinhole SPECT images**

*This chapter investigates the differences in image noise and perfusion uncertainty associated with pinhole and parallel-hole SPECT camera designs. Some of the work in this chapter has been previously presented as conference abstracts.*

*Cuddy-Walsh, SG, Wells, RG, “Base-to-apex noise gradient with dedicated cardiac and standard SPECT camera designs,” Society of Nuclear Medicine and Molecular Imaging Annual Meeting (SNMMI), Philadelphia, PA, June 2018. Published in J. Nuc. Med. 59 (Supplement 1), 1708 (2018).*

*Cuddy-Walsh, SG, Wells, RG, “Differences in cardiac image noise for two SPECT camera designs” University of Ottawa Heart Institute’s Annual Research Day, Ottawa, ON, April 2018.*

*Cuddy-Walsh, SG, Wells, RG, “Position-sensitive noise characteristics in multi-pinhole cardiac SPECT imaging,” Canadian Organization of Medical Physicists Annual Scientific Meeting, Banff, AB, June 2014. Published in Med. Phys. 41:8, 3-4 (2014).*

*Cuddy-Walsh, SG, Wells, RG, “Position-dependent noise in multi-pinhole SPECT,” Society of Nuclear Medicine and Molecular Imaging Conference, June 2014. Published in J. Nuc. Med. 55 (Supplement 1), 490 (2014).*

*Cuddy-Walsh, SG, Wells, RG, “Effects of position-dependent count sensitivity on the accuracy of MPI with multi-pinhole cardiac SPECT imaging” The 7th Annual Molecular Function and Imaging (MFI) Symposium, Ottawa, ON, June 2014.*

## **6.1 Introduction**

The sensitivity of dedicated cardiac multi-pinhole SPECT cameras is known to decrease with increasing distance from the collimators [33]. This means that the spatially dependant gradient in number of photons detected is predicted to be larger for a pinhole camera than for a parallel-hole camera design when they both include attenuation effects (Section 2.3.2). Such photon detection efficiency gradients will inherently lead to gradients in image noise within the FOV which has the potential to impact the efficacy of both visual image interpretation and quantitative image interpretation such as with a normal database (Section 1.8.2). If camera- and reconstruction-specific normal databases are used, the differences in image noise over the length of the heart may not present an issue however institutions that use percentile-based interpretation of normal may be impacted by position-dependent differences in the uncertainty of “normal”. While the sensitivity gradient has previously been measured for a multi-pinhole camera [33], the extent of the resulting noise gradient has not been quantified. As discussed in Chapter 4, the noise gradient cannot be directly inferred from the sensitivity gradient since noise characteristics of tomographic images are also influenced by the reconstruction algorithm. The aim of this work is to quantify the extent of the noise gradient in cardiac SPECT images and to evaluate differences between multi-pinhole and standard parallel hole SPECT cameras with respect to image noise gradients and local variability within normal databases.

## **6.2 Methods**

### **6.2.1 Study Design**

For this work, 93 SPECT studies were retrospectively reprocessed and evaluated for

patients referred for MPI with a standard parallel-hole SPECT/CT (Infinia Hawkeye4, GE Healthcare, Haifa, Israel) and subsequently imaged with a dedicated-cardiac multi-pinhole camera (DNM530c; Discovery NM530c, GE Healthcare, Haifa, Israel). The original study for which the data were collected was approved by the Ottawa Health Science Network Research Ethics Board (OHSN-REB), and this retrospective study was approved by both the OHSN-REB and the Carleton University Research Ethics Board-B (CUREB-B). From the available studies, patients (45 female, 48 male) were selected if their rest/stress ECG-gated studies were deemed normal based on clinical evaluation of myocardial perfusion images by a board-certified cardiologist. A summary of the characteristics of the study population is provided (Table 6.1).

### **6.2.2 Image Acquisition and Reconstruction**

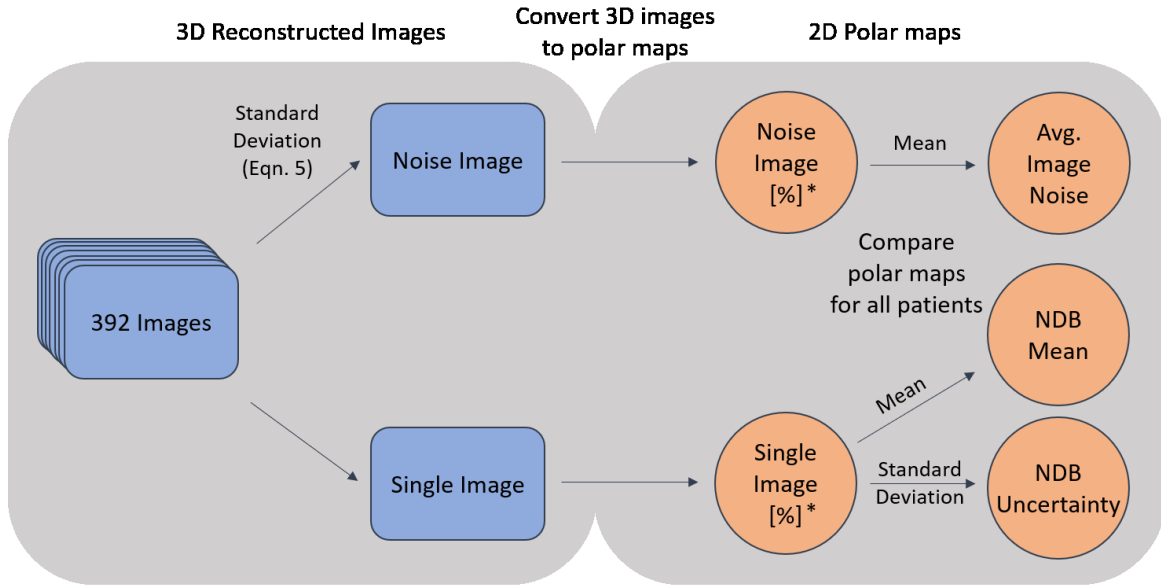
Patients were administered  $340 \pm 30$  MBq of  $^{99m}\text{Tc}$ -tetrofosmin for the rest component of a one-day rest-stress study according to our clinical protocol. Two female patients weighing  $> 110$  kg underwent two-day rest-stress studies. They were administered 1079 and 1270 MBq respectively for the rest component of their studies. Patients were imaged with both the Infinia Hawkeye4 and DNM530c. The order of scan acquisition was based on camera availability with first-acquisition preference given to the Infinia. The average time from injection to first imaging was  $63 \pm 16$  min. The second image was acquired at  $79 \pm 28$  min post-injection. Infinia acquisitions were performed for 25.6 seconds per  $3^\circ$  step with 30 steps of two detector heads for a total acquisition time of 12.8 min for a  $180^\circ$  acquisition. DNM530c acquisitions were performed for 8 minutes. An x-ray computed tomography (CT) image for attenuation correction was acquired using the Infinia's integrated Hawkeye4 CT scanner (120 kVp, 1.0 mA, 2.0 rpm).

Photon counts in projection sets were retrospectively rescaled using our camera-specific weight-based protocol (Equation 22) to standardize the average myocardial image noise for each patient to 6.1% for DNM530c and 15.5% for Infinia acquisitions. This corresponded to the mean activity injected clinically at our institution and was equal to 4.49 MBq/kg for a 5 min DNM530c study and 4.35 MBq/kg for a 12.8 min Infinia study. As described in Section 2.3.4, count rescaling was achieved using Poisson resampling [2] where the total number of counts in the projection data was reduced by the ratio of the necessary weight-based activity to the decay corrected actual administered

**Table 6.1 Characteristics of 93 patients imaged with both SPECT cameras who had normal myocardial perfusion imaging results\***

<b>Characteristic</b>	<b>Both (n = 93)</b>	<b>Male (n = 48)</b>	<b>Female (n = 45)</b>
Age [years]	61 ± 11 (37 – 86)	60 ± 11 (37 – 84)	62 ± 11 (40 – 86)
Body Weight [kg]	82 ± 17 (45 – 128)	87 ± 15 (57 – 118)	77 ± 18 (45 – 128)
Height [cm]	169 ± 10 (145 – 193)	175 ± 8 (152 – 193)	162 ± 8 (145 – 175)
Body Mass Index (BMI) [kg/m <sup>2</sup> ]	29 ± 5 (16.5 – 51.9)	28 ± 4 (19.9 – 37.9)	29 ± 6 (16.5 – 51.9)
Current Smoker [%]	8	8	7
Ex-Smoker [%]	39	44	33
Hypertension [%]	56	54	58
Diabetes [%]	14	17	11
Hyperlipidemia [%]	49	50	49
Family History [%]	44	38	51
Infarct [%]	5	4	7
Previous percutaneous coronary intervention [%]	5	6	4
Previous coronary artery bypass graft [%]	3	6	0
Valvular Disease [%]	2	2	2

\*Normal based on clinical evaluation of rest/stress, gated/ungated myocardial perfusion imaging (MPI) studies by a board-certified cardiologist



\*Normalize polar maps to maximum segment in the single polar map image

**Figure 6.1** Flow chart for calculating intra- and inter-patient image variability. **Intra-patient image variability (top row):** On the left side, the noise image is computed for each patient as one standard deviation of the 392 statistical replicate images. These are converted to polar map representation (right-circles) and a mean of all noise polar maps is taken to obtain the average image noise. This is an indicator of the average statistical variability if each patient study were repeated (intra-patient). **Inter-patient image variability (bottom row):** A single image (left-rectangle) for each patient is converted into polar map representation (right-circles). The average of these polar maps for all patients, the normal database (NDB) mean is an indicator of the average relative myocardial perfusion distribution for a given population, camera, and reconstruction method. The standard deviation over single image polar maps for all patients provides the uncertainty in the NDB. The NDB uncertainty is an indicator of the variability of perfusion due to physiological and camera positioning differences in the population in addition to statistical variability.

activity. For each patient, 392 replicates projection sets were generated and reconstructed.

Infinia projection data were reconstructed with both NC and AC using 2 iterations of an OSEM algorithm with 10 subsets. DNM530c projection data were reconstructed using a MAP-EM algorithm with an OSL Green prior in accordance with our clinical protocols. NC reconstructions were performed with 40 iterations (OSLG,  $\alpha = 0.5$ ,  $\beta = 0.3$ ) and AC with 60 iterations (OSLG,  $\alpha = 0.7$ ,  $\beta = 0.5$ ). No post-reconstruction filtering was applied for either camera. The full set of reconstructed images was comprised of 392 statistically independent replicates  $\times$  2 reconstruction options (NC/AC)  $\times$  2 cameras  $\times$  93 patients for a total of 145 824 volumes.

### **6.2.3 Noise and Normal Database Variability Calculation**

The effect of pinhole camera design on noise variability in the camera's FOV was evaluated based on normal database (NDB) variability and intra-patient image variability (image noise determined from the ensemble voxel variance of the reconstructed replicate images, Equation 5). All evaluations were performed for three gender groups (male, female, or both), two camera options (DNM530c or Infinia), and two reconstruction options (NC or AC). The methods outlined in Figure 6.1 and explained below were applied to each of these 12 scenarios.

#### **Average Intra-patient Noise**

Specifically, the intra-patient standard deviation (noise) was calculated over all 392 statistical replicates of each patient image. This was then converted to a polar map representation and normalized to the myocardial maximum in a segment in the polarmap of a single statistical replicate image. An average over all intra-patient standard deviation images in a gender group was calculated to obtain polar maps of the average image noise (Figure 6.1).

#### **Inter-patient Variability and the Normal Database**

Additionally, a single reconstructed replicate image for each patient was used to populate a normal database (NDB) for each gender group. Each image was transformed into cardiac polar maps and normalized to the myocardial maximum for standardized comparison. For each polar map segment position, the mean and standard deviation were calculated over all patients to obtain the NDB mean and NDB uncertainty polar maps (Figure 6.1).

#### **6.2.4 Statistical Analysis**

Two-tailed t-tests were used to test for differences in noise magnitude between the apical and basal segments of 17-segment cardiac polar maps (Figure 1.5). The level of significance was set to 0.05 for all analyses and modified according to Šidàk [98] corrections when multiple comparisons were performed. The primary evaluation compared the average noise in the 5 most apical segments to the average noise in the 6 basal segments for all patient images in each gender/camera/reconstruction cohort ( $\alpha=0.05$ ). Secondary testing compared the noise in (1) the basal anterior to the basal inferior segments and (2) the mean of the two basal lateral segments to the mean of the two basal septal segments. The resulting p-values were compared with Šidàk corrected  $\alpha=0.0253$  (test family size of 2) to evaluate significance. Tertiary evaluations were also performed to compare noise in the apical segment to noise in the basal-inferior segment. Since there were 16 possible comparisons (apex to each of the other 16 segments), a Šidàk corrected value of  $\alpha=0.0032$  was used.

### **6.3 Results**

#### **6.3.1 Perfusion**

Average NDB perfusion images (Figure 6.2) have camera, reconstruction, and gender cohort-dependent differences in perfusion uniformity of the myocardium. NC images have a large septal perfusion dropout which is partially corrected in AC images. Male perfusion in the NC images is reduced in the basal inferior to basal anteroseptal territories; female perfusion is reduced in the basal inferoseptal to basal anteroseptal territories. This effect is greater for images acquired with the Infinia than with the DNM530c but improved by attenuation correction leaving only mild reduction in septal

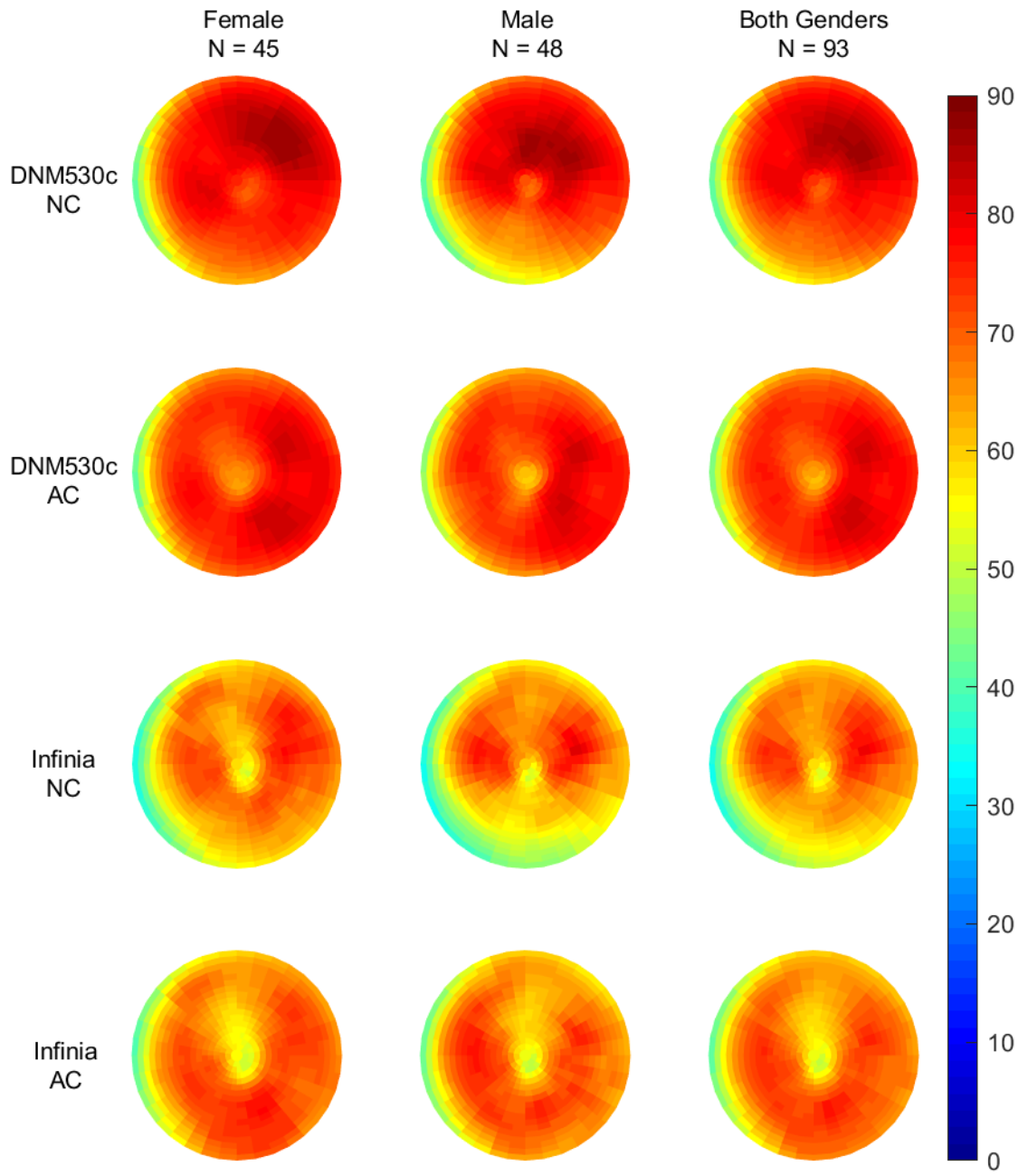


**Figure 6.2 Mean perfusion images for normal databases for specific camera, reconstruction, and gender-cohorts. Values are calculated from the average normalized perfusion for all polar map segments. Normalization is to the maximum perfusion in each patient image.**

perfusion for both cameras. The reduction of gender-dependent differences by attenuation correction is consistent with an earlier study which showed the same effect [99].

### **6.3.2 Image Noise**

#### **Apex-to-Base**

For individual patient images, the magnitude of image noise is visibly greater in basal segments than in apical segments of DNM530c attenuation corrected images but, for the Infinia camera and for the DNM530c NC images of the same patient, the differences are subtle (Figure 6.3). This is echoed when considering the average for each patient cohort (Figure 6.4, and rescaled in Figure 6.5); the average noise in the basal segments is 1.7-times greater than at the apex for AC ( $p < 0.005$ ) DNM530c images. There was a small but not statistically significant (1.1-fold,  $p > 0.051$ ) increase in noise for NC DNM530c images. For AC Infinia images, the 1.2-fold increase in noise was significant from apex-to-base for the male ( $p = 0.04$ ) and combined gender ( $p = 0.04$ ) groups; this increase was not significant for the female group ( $p = 0.052$ ). For NC Infinia images, the noise was approximately constant from apex-to-base with a non-significant reverse gradient (0.92-fold to 0.98-fold change,  $p = 0.3$ ) in keeping with a reduced mean perfusion in the septum.

#### **Basal Anterior-to-Basal Inferior**

The image noise does not significantly increase from the anterior to the inferior basal segments for NC images ( $p > 0.1$  for Šidák corrected  $\alpha=0.0253$ ). Attenuation correction removes the apparent reduction in counts seen in the inferior-lateral wall of NC perfusion images (Figure 6.2). However, there are still relatively lower counts contributing to this

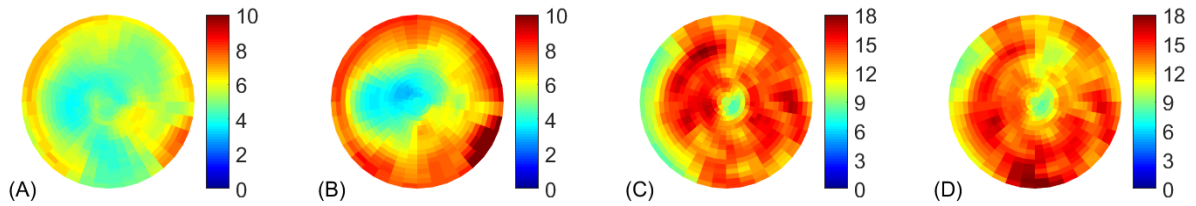


**Figure 6.3** Example noise distributions for images of one male patient acquired with the (A & B) DNM530c and (C & D) Infinia cameras and reconstructed (B & D) with and (A & C) without attenuation correction. The average noise is 7.5% in basal segments and 4.1% in apical segments in (B); it is 13.4% and 11.3% respectively in (D).

region. As a result, the image noise is amplified in the inferior-lateral wall such that it is 1.2- to 1.4-times larger than in the anterior wall in AC DNM530c images ( $p < 10^{-4}$ ) and 1.1-fold ( $p < 10^{-4}$ ) in AC Infinia images.

### Basal Lateral-to-Basal Septal

Additionally, in NC images, the noise is lower in the septum compared with the lateral wall for male patients and the combined gender group imaged with the DNM530c (0.9-fold,  $p = 0.0003$ ) and for all three gender groups imaged with the Infinia (0.8-fold,  $p < 10^{-4}$ ). The lateral-to-septal segment noise discrepancy is eliminated with attenuation correction for all imaging cohorts except for the AC DNM530c male and gender-combined images for which the noise gradient is reversed (1.1-fold,  $p < 0.01$  for Šidàk corrected  $\alpha=0.0253$ ).

### Apex-to-Basal Inferior Segment

The increase in AC image noise from the most apical segment to the basal-inferior segment is the largest of the differences between the apex and other segments; it increases 2.1-fold for AC DNM530c images ( $p < 10^{-4}$  for Šidàk corrected  $\alpha=0.0032$ ) and 1.3-fold for AC Infinia images ( $p < 10^{-4}$ ). The increase for AC DNM530c is 2.2-fold in male patient images and 2.1-fold in female patient images. There is not a significant

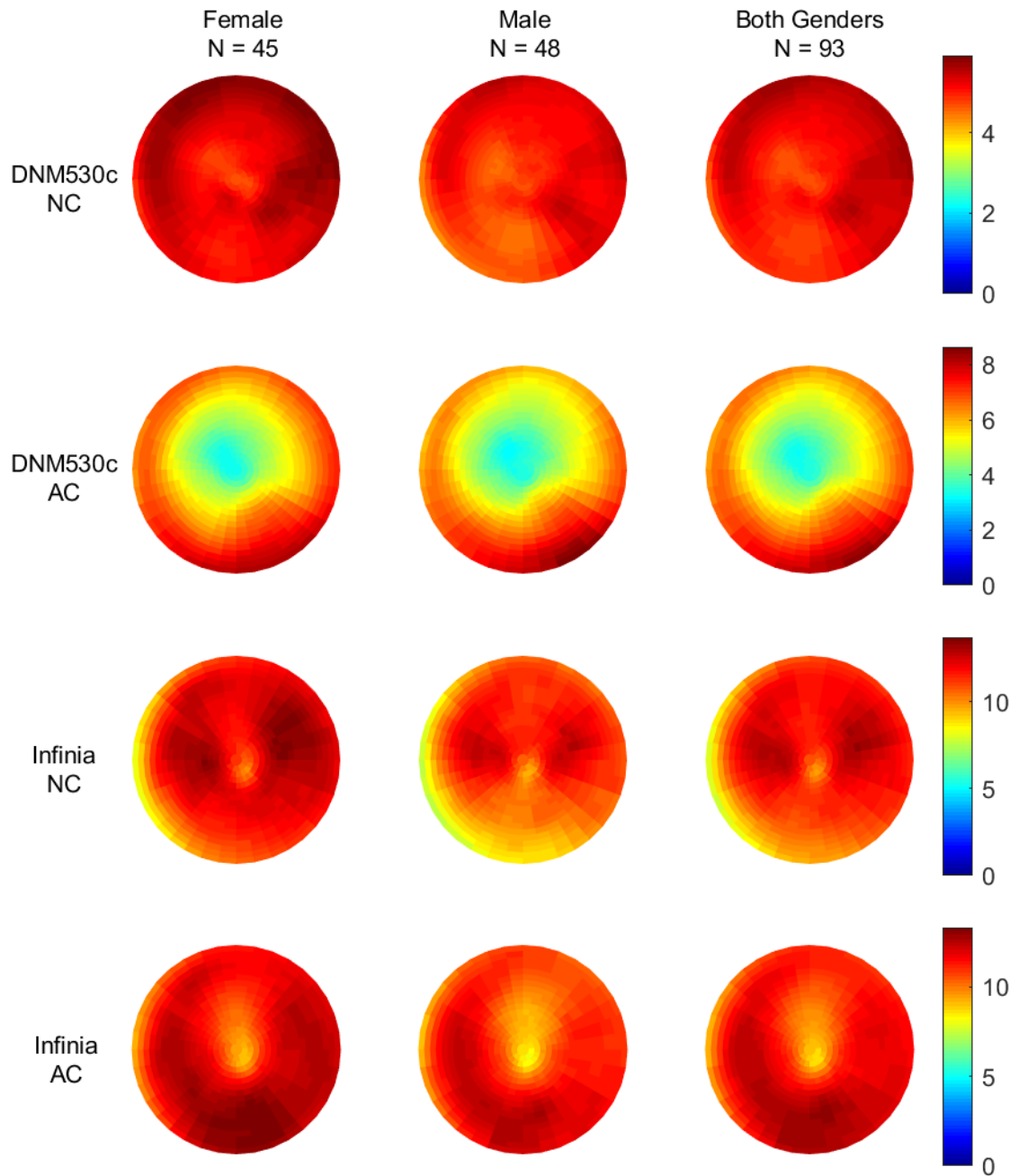


**Figure 6.4** Stochastic image noise due to camera design and attenuation dependent differences in photon counting. This contribution is calculated as the average of all individual intra-patient noise polar map segments. NC and AC perfusion images are averaged over all male and female patients imaged with the DNM530c and Infinia cameras.

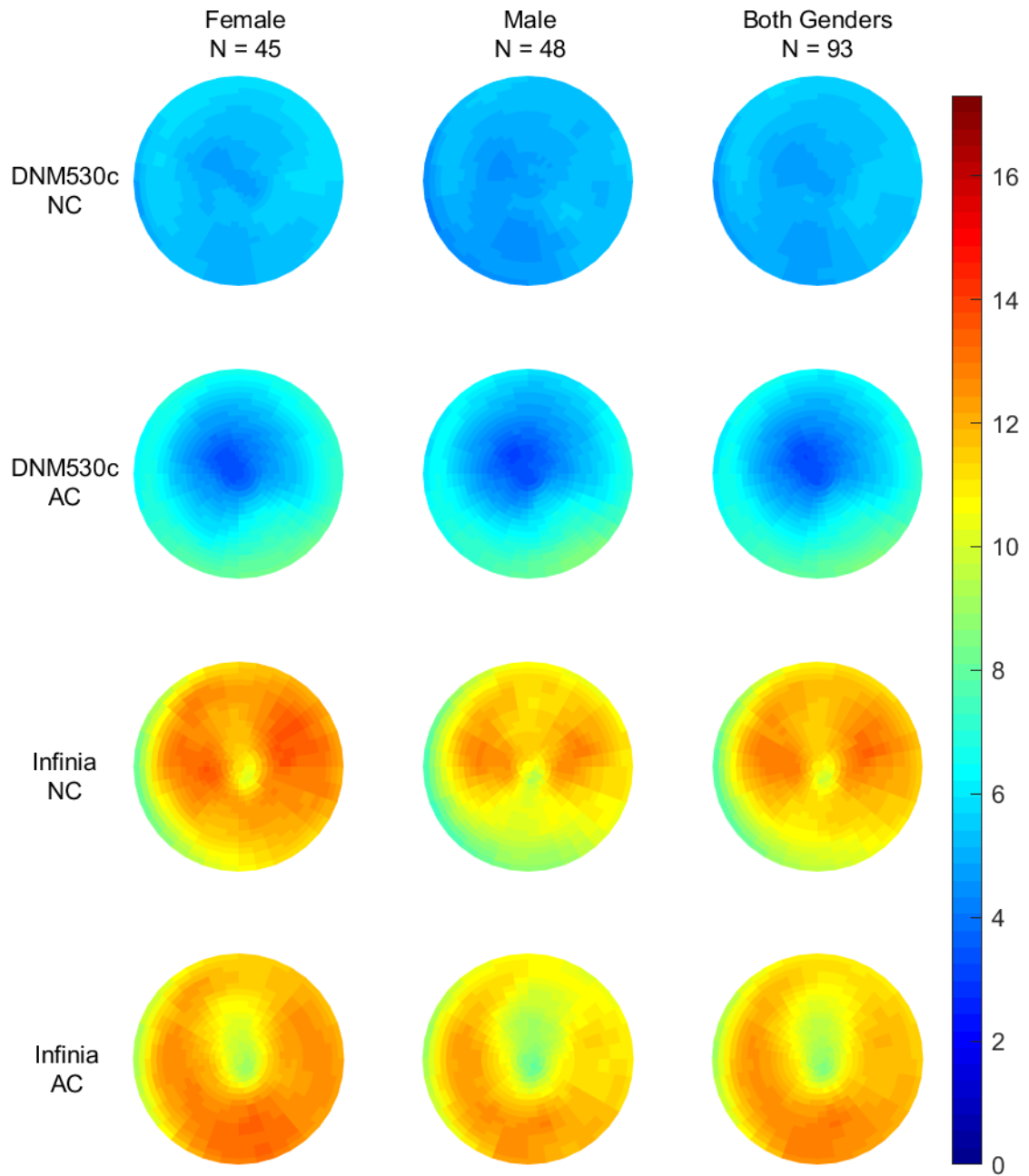


**Figure 6.5** The same camera and attenuation dependent noise images as in Figure 6.4 with the scales unified to a maximum value of 17.3 for direct comparison with the uncertainty in the normal database in Figure 6.6.

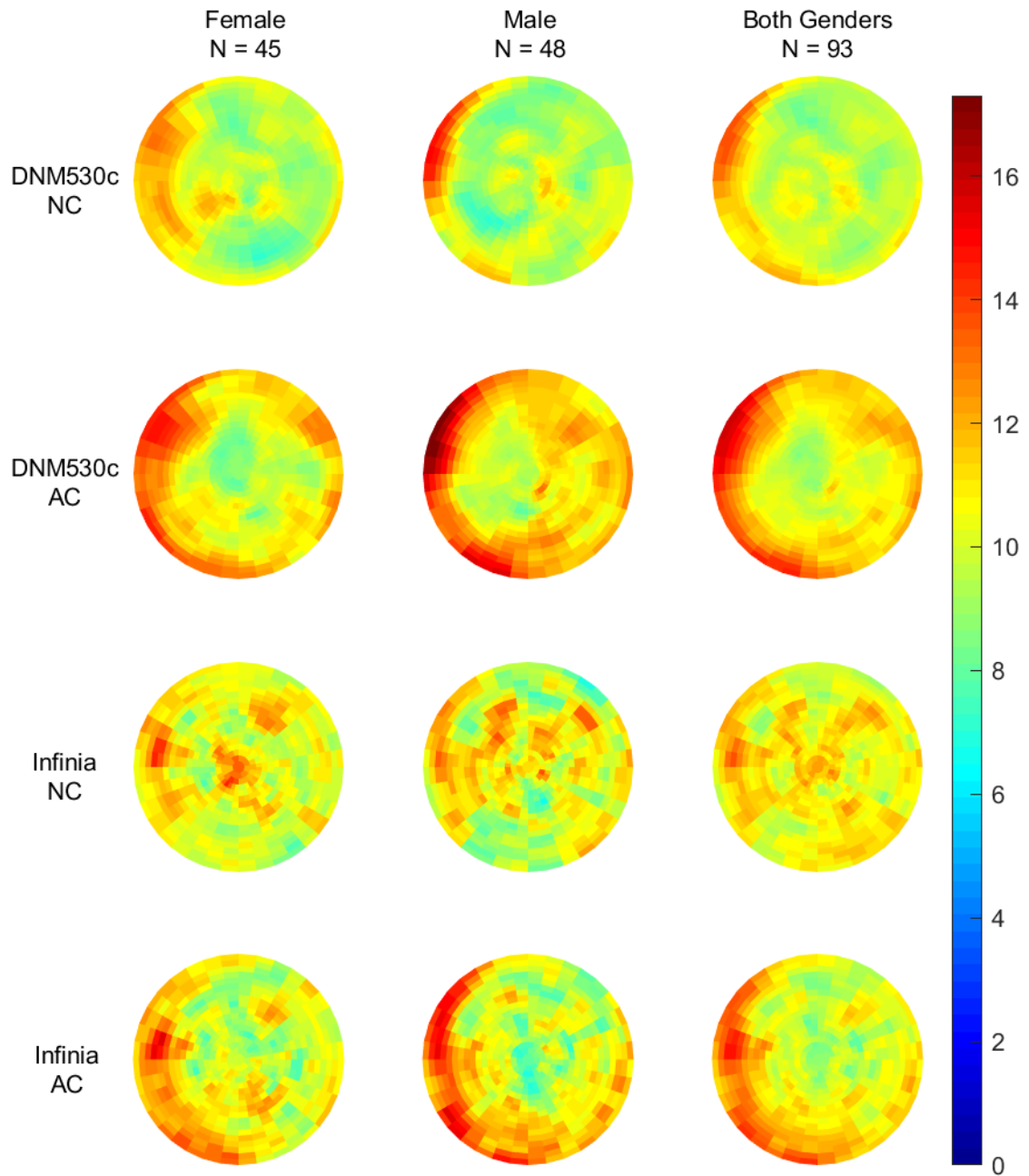


**Figure 6.6** Camera, reconstruction, and gender-specific normal database uncertainty images calculated as one standard deviation of normalized perfusion for all polar map segment values corresponding to normal MPI results. The maximum value of the scale is 17.3% of the maximum perfusion.

increase in noise from the apical to basal inferior segments in the NC images.

### **6.3.3 Normal Database Variability**

The uncertainty in relative perfusion of each segment in a normal database (Figure 6.6) incorporates the variation in patient physiology and position of the heart in the camera FOV in addition to stochastic image noise. The uncertainty was 1.3-fold higher in the basal segments of the myocardium compared with the apical segments for AC DNM530c images of the female ( $p = 0.02$  for  $\alpha=0.05$ ) and combined male-female ( $p = 0.04$ ) patient cohorts. The 1.2-fold increase observed for the male cohort was not statistically significant ( $p = 0.09$ ). The NDB uncertainty was also not significantly different for NC DNM530c ( $<1.04$ -fold,  $p > 0.4$ ) or NC (0.95-fold,  $p > 0.3$ ) and AC (1.1-fold to 1.3-fold,  $p > 0.1$ ) Infinia images.

### **6.3.4 Noise and Normal Databases**

To compare the contribution of Poisson-influenced noise to the uncertainty in a normal database Figure 6.5 and Figure 6.6 are displayed with the same scale. The level of the total uncertainty in the normal database is greater than the level of noise associated with Poisson counting statistics for the DNM530c camera. For the Infinia camera, the maximum of the NDB uncertainty is greater than the noise but overall, they are of a similar magnitude. Average uncertainty levels do not differ between patient genders but change for different cameras and reconstruction parameters. Distributions of noise and uncertainty within the left-ventricle are variable with gender.

## **6.4 Discussion**

The basal-septal wall of the left-ventricle is usually positioned deepest in a supine patient relative to the standard detector position for both cameras. Increased photon

attenuation thus results in the apparent hypoperfused septum in non-attenuation corrected images. Extra abdominal tissue characteristic of much of the male population undergoing MPI leads to an attenuation artifact extending from the basal-anteroseptal to the basal-inferior wall [38]. While this artifact is consistently present in Infinia images, its magnitude and position with DNM530c images have been noted to depend on patient positioning relative to pinhole detectors [85], [100]. It is thus less obvious in NC DNM530c perfusion images, but this variability can be seen in the corresponding NDB uncertainty images.

As is expected, attenuation correction improves perfusion uniformity but is fundamentally unable to alter the underlying counting statistics. As a result, noise is amplified by AC in the regions that contained NC image attenuation artifacts such as the basal-septum. Consequently, the closest region of the heart to the detectors, the apex, has the lowest stochastic noise in AC reconstructed images. The gradient of noise from apex-to-base is subtle for AC images and non-existent for NC images acquired with the Infinia since the photon sensitivity of parallel-hole collimators is roughly constant with distance from the collimator and changes in noise level are thus due to attenuation alone. It should also be noted however that breast and abdominal artifacts are expected to be less severe in DNM530c images compared to Infinia images because the pinhole camera is focused on the heart [101]. Since less aggressive attenuation correction is required, in DNM530c images I observe less of an increase in noise from NC to AC images than I observe with Infinia images.

The effect of depth dependent photon sensitivity for pinhole collimators leads to a larger noise gradient in the DNM530c camera compared with the Infinia. While not

statistically significant, a subtle gradient in stochastic noise can also be seen (Figure 6.4) for NC images. In this case, the reconstruction algorithm corrects for the photon sensitivity gradient, but the low number of detected photons contributing to the statistical distribution of voxel values in relatively lower sensitivity regions results in higher noise in these voxels. When attenuation effects are also corrected in the reconstruction algorithm the voxel value increases, but the statistical noise is also amplified. This gradient is steeper, and the apex-to-base difference is significant for AC DNM530c images which include effects of both the variable photon sensitivity and attenuation.

Although the clinical impact of the 1.7-fold stochastic gradient for DNM530c AC images is not directly evaluated, I show that this is propagated into a 1.2- to 1.3-fold gradient of the perfusion uncertainty in a normal database. Visual evaluation and perfusion scoring used clinically may be influenced by these differences. MPI testing will be more sensitive to differences in perfusion in the lower uncertainty regions near the apex of the left ventricle. Conversely, higher uncertainty close to the base of the heart means that differences in perfusion values must be larger (more severe disease) to detect lesions. Additionally, the average level of uncertainty in the normal database is slightly higher for Infinia images than for DNM530c images suggesting that the physiological variability between patients dominates in the DNM530c NDB but that noise dominates in the Infinia NDB. However, the larger gradient in the DNM530c AC uncertainty causes its minimum uncertainty to be lower than the Infinia. Thus, for the evaluated weight-based protocol and reconstruction parameters, the DNM530c is more sensitive than the Infinia to perfusion differences at the apex.

Since tissue in the apex of the heart is farthest from origin of the coronary arteries, any

upstream lesions may cause perfusion defects. Consequently, the apex is where hypoperfusion is often observed for mild, moderate, and severe disease. Thus, while this work demonstrates significant gradients in image noise and NDB uncertainty, it is fortunate to note that the lowest uncertainty is at the apex. Furthermore, the variable distribution of perfusion value uncertainty due to stochastic noise in the DNM530c camera emphasizes the need for normal patient databases to obtain accurate interpretations of MPI studies. I recommend that normal databases are specific to the camera and NC/AC option. Best practices would have camera, imaging protocol (related to the stochastic noise level), reconstruction parameter, and gender-specific normal databases.

## **6.5 Conclusions**

This study has demonstrated the presence of a 1.7-fold image noise gradient from apex-to-base for attenuation corrected images acquired with a dedicated cardiac pinhole SPECT camera. This leads to as much as a 1.3-fold increase in the uncertainty of normal database perfusion values over the length of the heart which has the potential to influence lesion detectability. For parallel-hole system images and pinhole camera images reconstructed without correcting for attenuation effects, image noise was not significantly spatially variable.

## **Chapter 7: Summary and Future Directions**

*From completed projects to budding ideas, this chapter provides a synopsis of research completed during this thesis and a roadmap of projects to tackle in the future.*

*The research based on the idea presented in Section 7.2.4 has been published as a conference proceedings paper.*

*Cuddy-Walsh, SG, Massalha, S, Marvin, BF, Carey, C, Ruddy, TD, Wells, RG, "Evaluating patient-specific z-score images for lesion detection in low count studies," 2018 IEEE Nuclear Science Symposium and Medical Imaging Conference Record, Sydney, AU, November 2018.*

## 7.1 Summary of Knowledge Gained

This thesis evaluated the impact of pinhole SPECT camera design on spatial resolution and image noise. It also developed novel techniques to enable personalized imaging with weight-based protocols to standardize the level of image noise and patient-specific noise maps to assist with image interpretation.

By identifying position and object-orientation dependent differences in spatial resolution within the fully supported FOV, I have expanded the understanding of the properties of pinhole SPECT camera designs. When imaging structures that are close in size to the system's stated spatial resolution, such substantial resolution changes in the FOV may have negative implications for detecting small lesions positioned farther from the detector array of a pinhole camera. Additionally, the non-uniform blurring demonstrated may cause partial volume errors closer to the base of the heart which may contribute to position-dependent differences in quantification [85], [100], [102] seen by commercially available dedicated cardiac pinhole SPECT cameras.

Dedicated cardiac pinhole cameras such as the DNM530c have been previously shown to have position-dependent sensitivity in their field-of-view [33] and were herein revealed to have corresponding image noise gradients increasing as much as 1.7-fold over the length of the heart for attenuation corrected images. The noise gradient is steeper for pinhole cameras than traditional gamma cameras such as GE Healthcare's Infinia Hawkeye4. The pattern of noise is however mathematically predictable given knowledge of the camera design and an image-specific attenuation map. Harnessing the stochastic nature of photon counting, a method was developed for directly computing the Poisson-like noise associated with a DNM530c attenuation corrected image. The new technique

uses calibration factors specific to reconstruction parameters to scale the noise to the correct magnitude thus enabling rapid computation of noise images. To further investigate the image noise characteristic of pinhole SPECT cameras, I compared the average magnitude of image noise in the myocardium to the injected activity, patient weight, and acquisition duration. This information was used to develop a patient-specific imaging protocol, based on the noise in the reconstructed image, that built upon previous knowledge [70], [73], [75] relating patient habitus to the number of counts in projection space.

## **7.2 Future Directions**

### **7.2.1 Spatially dependent image resolution**

The variable resolution demonstrated in Chapter 3 was evaluated for noise-free simulations with arbitrary pinhole-detector positions demonstrating the extent of potential variability in spatial resolution stated for pinhole SPECT cameras. To build on this foundation, simulations which include noise should be conducted and experimental evaluation using a camera with at least one rotating detector head outfitted with a pinhole collimator could be used to evaluate camera designs for arbitrary pinhole-detector positions. Moreover, direct evaluation of resolution uniformity in commercially available pinhole cameras might provide more insight into the clinical relevance of these resolution effects. Simulation studies that model the clinical camera could be used to identify approximate locations and object orientations within the quality FOV which have relatively degraded resolution. This may help in narrowing down test positions and orientations for experimental evaluation using a disk-phantom. Additionally, the methods used in Chapter 3 would be invaluable to researchers developing new pinhole camera

designs prior to building prototypes.

### **7.2.2 Patient-specific noise image display**

As identified in Chapter 6, image noise is spatially dependent within the FOV for attenuation corrected images acquired with pinhole camera designs. Different patterns of attenuation in each patient and variations in positioning of a patient's heart in the FOV of a camera with variable sensitivity mean that the pattern of noise varies greatly between patients. Thus, neither an assumption of constant noise in the FOV nor utilization of a single noise map for all patients is correct. To provide physicians with information about the noise character specific to images that they are reviewing, a patient-specific noise map should be calculated and displayed alongside perfusion images. Any of the noise calculating techniques presented in this thesis could be used to produce such maps however, from a speed perspective, the PV method (Chapter 4) and noise reconstruction method [62] would be most clinically feasible. A display of image noise should be integrated into current or new image review software to provide physicians more information about local noise to help improve the probability of detecting statistically significant lesions if they are present. I have packaged the PV noise estimation code in an executable to calculate and output a noise image in Dicom format that can be loaded into current image review software.

### **7.2.3 Patient-specific SPECT acquisition protocols**

The analysis of weight-based (Chapter 5) and BMI-based (Appendix C) acquisition protocols developed in this thesis was performed by retrospectively adjusting the total acquired counts in projection images. This assumes that the detected number of counts has a linear relationship with the injected activity or acquisition duration. Prior to regular

clinical adaptation, it is important the chosen protocol be evaluated with a prospective study.

The protocols may also be further improved and tailored directly to a specific patient immediately before imaging. The PV method developed in Chapter 4 could be used along with a CT of the patient to calculate an approximate noise map for an assumed count level in the heart. The CT image acquired prior to initial imaging could be used to generate a prospective attenuation map assuming uniform perfusion (or a population normal) within the LV. This attenuation map could be used to estimate the level of attenuation specific to a patient and determine the injected activity or acquisition duration needed to ensure that the patient image does not exceed the clinic's target level of noise. For dynamic blood flow studies, this could allow the injected activity to be supplemented or reduced prior to injection. For studies which acquire the CT after injection, the acquisition times could be lengthened to ensure diagnostic quality. For static (non-dynamic) imaging studies, a quick estimation of noise could be performed before the patient is released from the camera for patient-specific image quality control (QC). If the image noise level is too high, technicians could simply resume an acquisition to acquire additional data by increasing the total acquisition time. This would enforce similar noise levels for all images and save time in the clinical workflow by avoiding unloading and reloading patients in the camera.

#### **7.2.4 Identifying statistically significant lesions outside of the LV**

Nuclear imaging (SPECT and positron emission tomography, PET) is also used to image organs other than the heart. Normal databases aren't feasible in many of these cases since anatomy is variable in the population. Functional imaging of metabolic

activity for cancer screening or staging or of apoptotic (cell death) activity investigating atherosclerotic plaques at high risk for rupture causing stroke are two such examples. For these applications, it is sometimes difficult for clinicians to get enough activity in the patient to identify lesions while keeping the biological dose to the patient low. As a result, small cancer or high-risk plaque lesions tend to have low signal compared with background making it difficult to choose a threshold for a measure such as a ratio of lesion counts to background counts. Having information about the noise in each voxel of an image could allow for a statistical comparison between a chosen background reference signal and a suspected lesion to evaluate significance. This comparison can be done between the reference value and all other voxels in an image to highlight and direct physicians to inspect all regions with significantly different image values.

#### **7.2.5 Noise-based camera quality control**

Regular evaluation of patient-specific image noise is also valuable for camera quality assurance programs. Image noise levels could be monitored for known patient habitus and acquisition protocols over time to determine when the camera may be underperforming. Typical SPECT QC tests produce corrections of non-uniformities and identify non-functioning or poorly performing detector pixels. Digital corrections may produce accurate images however the noise character will change. If imaging times or tracer activities must be increased to achieve historic image noise levels, quality assurance software may be able to trigger a service request to restore the camera performance.

### **7.3 Final Thoughts**

Heart disease affects 8% of Canada's adult population [3]. Myocardial perfusion

imaging with SPECT helps to diagnose, monitor therapy of, and risk-stratify heart disease to help guide treatment decisions. SPECT cameras employing multiple stationary pinhole collimators offer improved overall sensitivity, resolution, and enable dynamic studies including those for myocardial blood flow. These advances come at the cost of variable photon sensitivity and resolution within the quality field-of-view of the camera [33]. To date, the influence of these effects on image noise has not been reported. The work reported in this thesis has demonstrated a significant noise gradient in the FOV of one such camera. It also provides tools for patient-specific imaging protocols and rapid estimation of image noise. This work provides important information about the pattern of noise and resolution in pinhole SPECT cameras and thereby contributes a step towards harnessing the full potential of imaging with these cameras to provide a standardized and improved level of patient care.

## **Appendices**

*Contained herein are supplementary results and documents which helped to facilitate the research in this thesis but fall outside the main scope.*

<b>Appendix A - Emission and CT registration for attenuation correction .....</b>	<b>137</b>
<b>Appendix B - Required number of bootstrapping replicates for noise calculation</b>	<b>138</b>
<b>Appendix C - BMI-based patient-specific imaging protocol for Chapter 5 .....</b>	<b>142</b>
<b>Appendix D - Permission to reproduce published material.....</b>	<b>143</b>
<b>Appendix E - Research Ethics .....</b>	<b>146</b>

## Appendix A - Emission and CT registration for attenuation correction

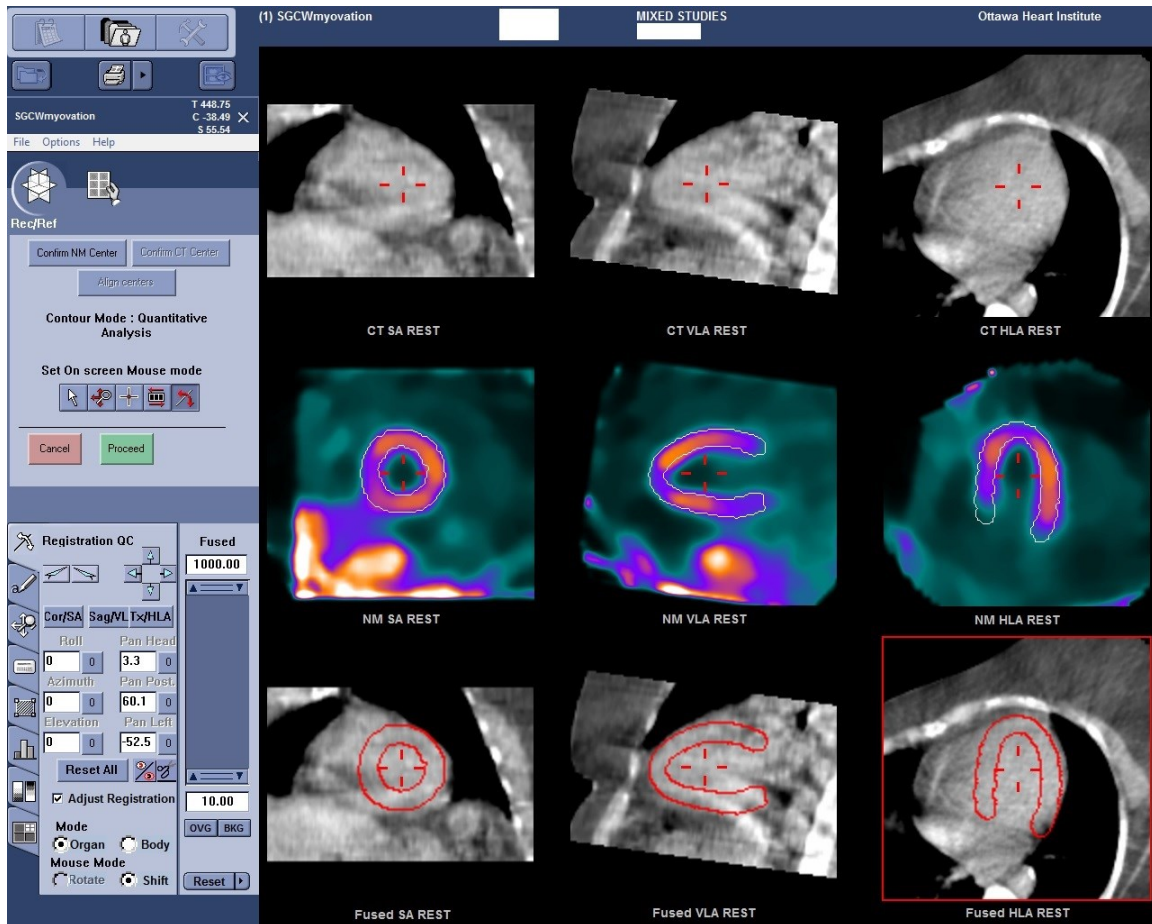


**Figure A.1** Example of alignment of non-attenuation corrected SPECT image from the DNM530c camera with CT anatomy image from the Infinia Hawkeye4 camera for the same patient. Image is a screen capture from the Myovation application with the GE Healthcare Xeleris software package used for alignment and generation of attenuation maps. The three columns correspond to from left to right, the short axis (SA), vertical long axis (VLA), and horizontal long axis (HLA) views of the left ventricle of the heart. The three rows correspond from top to bottom to the CT image, the SPECT reconstructed image, and the CT image overlaid with a contour of the left ventricle from the SPECT image. CT data is translated and rotated (if necessary) to contain the SPECT contours within the volume of the heart approximately in the location of the LV. Care is taken to ensure that LV activity does not overlap with lung or ribs on the CT image.

## Appendix B - Required number of bootstrapping replicates for noise calculation

Bootstrapping and pseudo-bootstrapping of projection data are used to simulate and calculate noise in MPI images in Chapter 4, Chapter 5, and Chapter 6. To determine the number of bootstrap replicates  $M$  required for a precise calculation of noise, the author performed an evaluation of noise for different  $M$ . Previous work by Buvat *et al.* recommends using at least 200 bootstraps [1]. I imaged a spherical phantom (as described in detail in Chapter 4) with the Discovery NM530c SPECT camera. The resulting projection set was pseudo-bootstrapped 1000 times and each of the new projection sets were reconstructed to produce  $M = 1000$  images. From these, noise images were computed using Equation 5 for subsets with  $M = 10, 25, 50, 75, 100, 250, 500, 750,$  or 1000. For a measure of true repeatability, the phantom was repeatedly imaged to acquire a total of 15 projection sets, each were subsequently reconstructed, and a “true” noise image was calculated. Noise values in all voxels in each of the  $M$  groups were compared to noise values in corresponding voxels of the true noise image using Bland Altman analysis as shown in Figure B.1A-Figure B.1H. A metric to evaluate convergence was extracted from these as one standard deviation of the difference between  $\sigma_M$  and  $\sigma_{true}$  all divided by the average value of  $\sigma_{true}$ . This value is plotted with relation to  $M$  in Figure B.1I and fit with a power function. Because 15 “true” image repeats may not be enough to compare to, the analysis was repeated for  $M = 1000$  in place of the 15 repeats (Figure B.2). Rearranging the power function in Figure B.2I, it is determined that 400 bootstraps are required to obtain image noise converged to within 5% of the standard deviation associate with  $M = 1000$  bootstrapped images.

To reconstruct a large number of bootstrapped replicates, the Lister or BatchRecon

reconstruction programs were used within the Xeleris software package (GE Healthcare, Haifa, Israel). They both call the same Alcyone technology reconstruction algorithm as Myovation but do not require user interaction thus allowing for batches of up to 98 reconstructions per run. The simplest method for managing large numbers of reconstructions for the same patient study, is to load 98 files into Xeleris at a time and reconstruct the entire group. Instead of 400 replicates, 392 ( $4 \times 98$ ) replicates were reconstructed for each study to reduce the time spent transferring files for all studies.

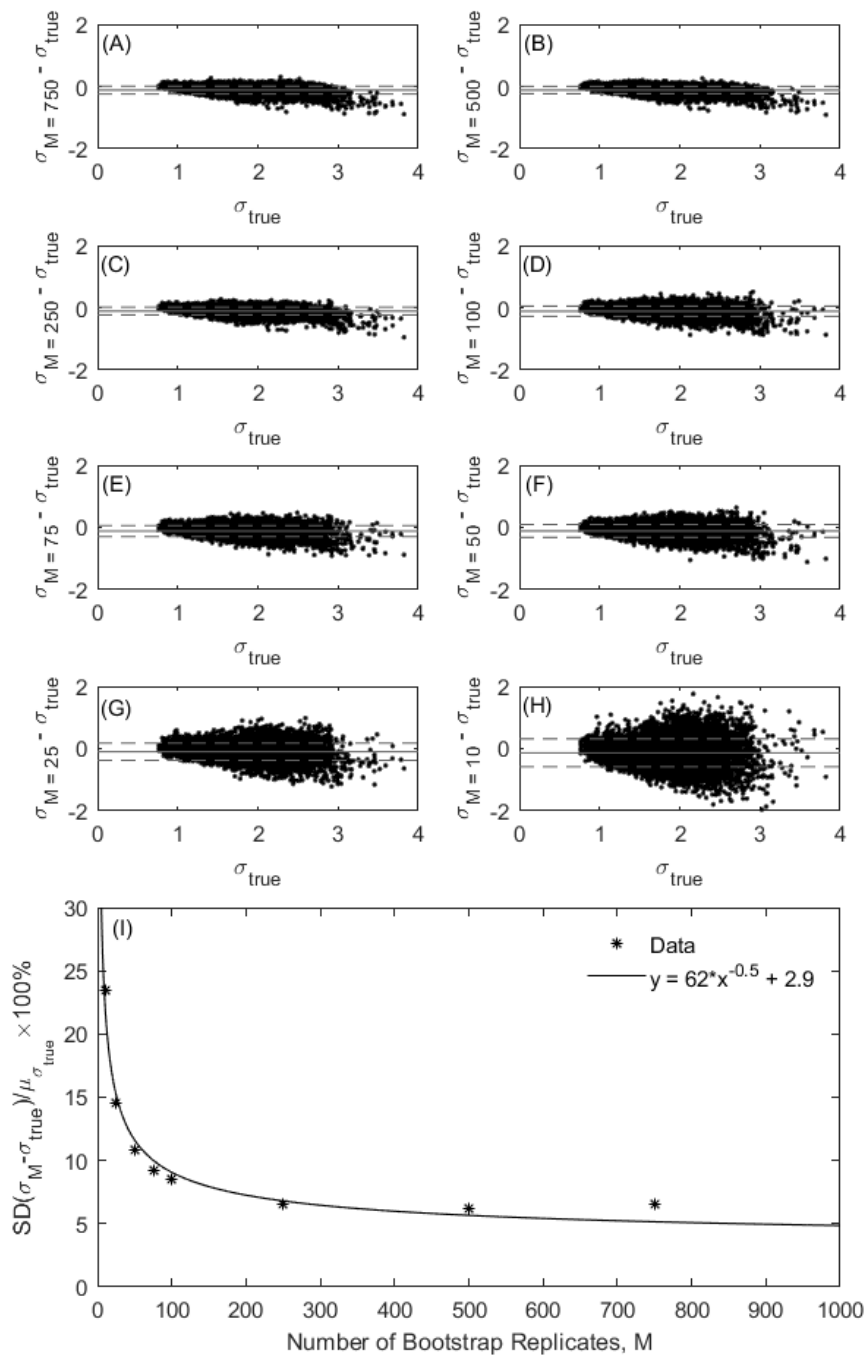


**Figure B.1** Noise for all voxels in a spherical phantom as calculated with 15 repeat acquisitions or M bootstrapped replicates. (A)-(H): Bland Altman plots displaying the difference between the two methods. The mean is shown as a solid line and on standard deviation is shown by the dashed lines. (I): One standard deviation of the difference between methods is expressed as a percentage of the average noise for 15 repeat acquisitions and related with a power function to the number of bootstrapped replicates.

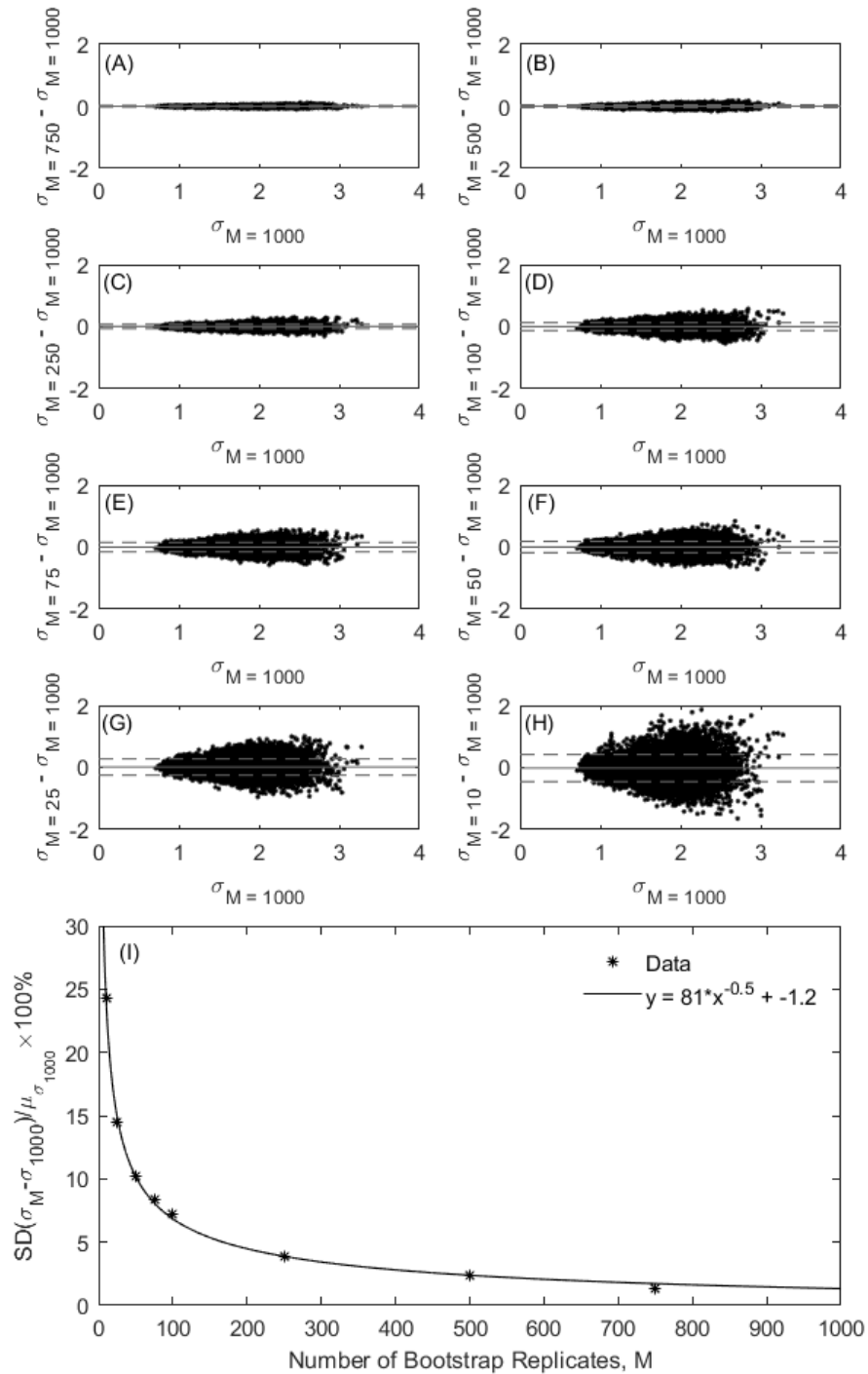


**Figure B.2** Noise for all voxels in a spherical phantom as calculated with different numbers  $M$  of bootstrapped replicates. (A)-(H): Bland Altman plots displaying the difference between the  $M$  replicates and  $M = 1000$  replicates. The mean is shown as a solid line and on standard deviation is shown by the dashed lines. (I): One standard deviation of the difference between methods is expressed as a percentage of the average noise for  $M = 1000$  and related with a power function to the number of bootstrapped replicates.

## Appendix C - BMI-based patient-specific imaging protocol for Chapter 5

**Table C.1. BMI-based administered activity ( $A$  [ $MBq$ ]) and acquisition duration ( $T$  [ $min$ ]) formula coefficients\*, 95% confidence intervals, and adjusted Pearson's r-squared for standardizing the reconstructed image noise ( $\sigma$  [%]) level.**

	Gender		$k_1$		$k_2$	$adj. R^2$
<u>INFINIA<sup>†</sup></u>						
NC <sup>§</sup>	Both	196.5	(185.5, 207.5)	-0.3343	(-1.6, 0.9)	0.85
NC	Female	186.1	(162.8, 209.4)	1.1860	(-1.8, 4.2)	0.81
NC	Male	201.0	(180.2, 221.7)	-0.6568	(-3.4, 2.1)	0.85
AC	Both	183.2	(172.7, 193.7)	-0.2336	(-1.4, 1.0)	0.85
AC	Female	169.9	(149.4, 190.4)	1.1080	(-1.6, 3.8)	0.82
AC	Male	189.2	(168.6, 209.9)	-0.2998	(-3.0, 2.4)	0.83
<u>DNM530c<sup>‡</sup></u>						
NC	Both	47.83	(44.9, 50.8)	0.06832	(-0.4, 0.5)	0.86
NC	Female	44.30	(39.7, 48.9)	0.38580	(-0.4, 1.1)	0.86
NC	Male	48.36	(43.8, 52.9)	0.28200	(-0.5, 1.1)	0.87
AC	Both	44.49	(38.2, 50.8)	1.17600	(0.09, 2.3)	0.62
AC	Female	41.28	(32.9, 49.6)	1.20800	(-0.2, 2.6)	0.63
AC	Male	46.00	(36.7, 55.3)	1.33300	(-0.3, 3.0)	0.61

\*Coefficient values for use in  $A \cdot T = \left(\frac{k_1}{\sigma - k_2}\right)^2 \cdot BMI$  for calculating activity-time

products for patients with body mass index (BMI) in the range of  $16.5 - 51.9 \frac{kg}{m^2}$ .

<sup>†</sup>INFINIA refers to the Infinia Hawkeye4 SPECT/CT, GE Healthcare, Haifa, Israel

<sup>‡</sup>DNM530c refers to the Discovery Nuclear Medicine 530c SPECT camera, GE Healthcare, Haifa, Israel

<sup>§</sup>NC and AC refer to non-attenuation corrected and attenuation corrected reconstructions

## Appendix D - Permission to reproduce published material

This appendix contains a letter of permissions to include previously published articles in this thesis.

D.1: Chapter 3:

Cuddy-Walsh SG, Clackdoyle R, Wells RG. Directional resolution of limited-angle multi-pinhole SPECT cameras. In: *2014 IEEE Nuclear Science Symposium and Medical Imaging Conference*. November 2014.

D.2: Chapter 4 and Part of Section 2.3:

Cuddy-Walsh SG, Glenn Wells R. Patient-specific estimation of spatially-variant image noise for a pinhole cardiac SPECT camera. *Med Phys*. 2018;45(5):2033-2047.

## D.1 Chapter 3



Home Create Account Help 



**IEEE**  
Requesting permission to reuse content from an IEEE publication

**Title:** Directional resolution of limited-angle multi-pinhole SPECT cameras

**Conference Proceedings:** 2014 IEEE Nuclear Science Symposium and Medical Imaging Conference (NSS/MIC)

**Author:** Sarah G. Cuddy-Walsh

**Publisher:** IEEE

**Date:** Nov. 2014

Copyright © 2014, IEEE

**LOGIN**

If you're a [copyright.com](#) user, you can login to RightsLink using your [copyright.com](#) credentials. Already a [RightsLink](#) user or want to [learn more?](#)

### Thesis / Dissertation Reuse

**The IEEE does not require individuals working on a thesis to obtain a formal reuse license, however, you may print out this statement to be used as a permission grant:**

*Requirements to be followed when using any portion (e.g., figure, graph, table, or textual material) of an IEEE copyrighted paper in a thesis:*

- 1) In the case of textual material (e.g., using short quotes or referring to the work within these papers) users must give full credit to the original source (author, paper, publication) followed by the IEEE copyright line © 2011 IEEE.
- 2) In the case of illustrations or tabular material, we require that the copyright line © [Year of original publication] IEEE appear prominently with each reprinted figure and/or table.
- 3) If a substantial portion of the original paper is to be used, and if you are not the senior author, also obtain the senior author's approval.

*Requirements to be followed when using an entire IEEE copyrighted paper in a thesis:*

- 1) The following IEEE copyright/ credit notice should be placed prominently in the references: © [year of original publication] IEEE. Reprinted, with permission, from [author names, paper title, IEEE publication title, and month/year of publication]
- 2) Only the accepted version of an IEEE copyrighted paper can be used when posting the paper or your thesis on-line.
- 3) In placing the thesis on the author's university website, please display the following message in a prominent place on the website: In reference to IEEE copyrighted material which is used with permission in this thesis, the IEEE does not endorse any of [university/educational entity's name goes here]'s products or services. Internal or personal use of this material is permitted. If interested in reprinting/republishing IEEE copyrighted material for advertising or promotional purposes or for creating new collective works for resale or redistribution, please go to [http://www.ieee.org/publications\\_standards/publications/rights/rights\\_link.html](http://www.ieee.org/publications_standards/publications/rights/rights_link.html) to learn how to obtain a License from RightsLink.

If applicable, University Microfilms and/or ProQuest Library, or the Archives of Canada may supply single copies of the dissertation.

BACK

CLOSE WINDOW

Copyright © 2018 Copyright Clearance Center, Inc. All Rights Reserved. [Privacy statement](#). [Terms and Conditions](#).  
Comments? We would like to hear from you. E-mail us at [customercare@copyright.com](mailto:customercare@copyright.com)

## D.2 Chapter 4 and Part of Section 2.3



Angela E. Kayser  
Executive Director  
akayser@aapm.org  
671.298.1266

**DATE OF REQUEST:** August 10, 2018

**FROM:**

Sarah Cuddy-Walsh, University of Ottawa Heart Institute,  
H2258 - 40 Ruskin Street, Ottawa, ON, K1Y 4W7, Canada

**EMAIL ADDRESS:** swalsh@ottawaheart.ca

**1. Permission is granted to:**

Sarah G. Cuddy-Walsh / Carleton University

**2. Permission is requested to use the following material:**

author: Cuddy-Walsh SG, Glenn Wells R.  
article: Patient-specific estimation of spatially-variant image noise for a pinhole cardiac SPECT camera.  
journal: Medical Physics  
volume: 45  
pages: 2033-2047  
year: 2018

Entire article is to be used.

**3. For what purpose:**

The reformatted article is to be included as a chapter in the first author's PhD thesis.

Authors seeking permission must also notify the first author of the article from which permission is being sought.

Permission is hereby granted: \_\_\_\_\_  
Signature Date

The Association's Journals are Medical Physics and Journal of Applied Medical Physics  
Member Society of the American Institute of Physics and the International Organization of Medical Physics

1631 Prince Street | Alexandria, VA 22314-2818 | phone 571.298.1300 | fax 571.298.1301 | www.aapm.org

## **Appendix E - Research Ethics**

This appendix contains correspondence with the Ottawa Health Science Network Research Ethics Board (OHSN-REB) that was necessary to gain access to and responsibly use the clinical imaging data used in this thesis. It also contains a secondary letter of approval from the Carleton University Research Ethics Board B (CUREB-B). It consists of 2 sub-appendices containing letters of approval from OHSN-REB and CUREB-B and the corresponding OHSN-REB ethics protocol for research contributing to different thesis chapters.

## E.1 REB approval for research contributing to Chapter 4 and Chapter 6

### OHSN-REB Letter of Approval

---



**Ottawa Health Science Network Research Ethics Board/ Conseil d'éthique de la recherche du  
Réseau de science de la santé d'Ottawa**

Case Box 414 725 Parkdale Avenue, Ottawa, Ontario K1Y 4E9 613-790-5535 ext. 14022 Fax: 613-761-4311  
<http://www.ohsn.ca/ethics>

June 26, 2016

Dr. Glenn Wells  
Division of Cardiac Imaging,  
University of Ottawa Heart Institute  
40 Ruskin Street H1C 2G3  
Ottawa, ON K1Y 4W7

Dear Dr. Wells:

**Re: Protocol # 20160476-01H The Impact of position dependent sensitivity changes inherent to a new QZT-based dedicated cardiac camera on noise in patient images.**

**Protocol approval valid until: June 27, 2017**

I am pleased to inform you that this protocol underwent expedited review by the Ottawa Health Science Network Research Ethics Board (OHSN-REB) and is approved. No changes, amendments or addenda may be made to the protocol without the OHSN-REB's review and approval.

Protocol Version 4.0 dated June 1, 2016 is approved.

If the study is to continue beyond the expiry date noted above, a Renewal Form should be submitted to the REB approximately six weeks prior to the current expiry date. If the study has been completed by this date a Termination Report should be submitted.

OHSN-REB complies with the membership requirements and operates in compliance with the Tri-Council Priority Statement: Ethical Conduct for Research Involving Humans; the International Conference on Harmonization - Good Clinical Practice: Consolidated Guideline; the provisions of the Personal Health Information Protection Act 2004.

Yours sincerely,

Jim Robblee M.D.  
Vice-Chairperson  
Ottawa Health Science Network Research Ethics Board

JR/dw

# OHSN-REB Renewal Report



**Ottawa Health Science Network Research Ethics Board / Conseil d'éthique de la recherche du Réseau de science de la santé d'Ottawa**

Case Box 411 795 Parkdale Avenue, Ottawa, Ontario K1Y 4E9 (613-768-5555 ext. 1400) Fax: 613-761-4311  
http://www.ohsn.ca/ohsnreb

June 23, 2017

Dr. Glenn Wells  
Division of Cardiac Imaging  
University of Ottawa Heart Institute  
40 Ruskin Street H 1233  
Ottawa, ON K1Y 4W7

Dear Dr. Wells:

**RE: Protocol# - 20160478-01H The impact of position dependent sensitivity changes inherent to a new CZT-based dedicated cardiac camera on noise in patient images.**

**Renewal Expiry Date - June 27, 2018**

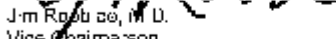
I am pleased to inform you that your Annual Renewal Request was reviewed by the Ottawa Health Science Network Research Ethics Board (OHSN-REB) and is approved. No changes, amendments or addenda may be made in the protocol or the consent form without the OHSN-REB's review and approval.

Renewal is valid for a period of one year. Approximately one month prior to that time a single renewal form should be sent to the RFB office.

OHSN-REB complies with the membership requirements and operates in compliance with the Tri-Council Policy Statement: Ethical Conduct for Research Involving Humans; the International Conference on Harmonization - Good Clinical Practice Consolidated Guideline; the provisions of the Personal Health Information Protection Act 2004.

The Tri-Council Policy Statement requires a greater involvement of the OHSN-REB in studies over the course of their execution. As well, you must inform the Board of adverse events encountered during the study, here or elsewhere, or of significant new information which becomes available after the Board review, either of which may impinge on the ethics of continuing the study. The OHSN-REB will review the new information to determine if the protocol should be modified, discontinued, or should continue as originally approved.

Sincerely,

  
Jim Roche, M.D.  
Vice Chairperson  
Ottawa Health Science Network Research Ethics Board

rdw

## CUREB-B Letter of Approval

---



Research Compliance Office  
511 Tory | 1125 Colonel By Drive  
| Ottawa, Ontario K1S 5B6  
613-520-2600 Ext: 4085  
[ethics@carleton.ca](mailto:ethics@carleton.ca)

### CERTIFICATION OF INSTITUTIONAL ETHICS CLEARANCE

Ethics clearance for the following research has been **cleared** by the Carleton University Research Ethics Board (CUREB-B) at Carleton University. CUREB-B is constituted and operates in compliance with the *Tri-Council Policy Statement: Ethical Conduct for Research Involving Humans* (TCPS2).

Ethics Protocol Clearance ID: Project # 105536  
Principal Investigator: Glenn Wells, Ottawa Heart Institute  
Research Team (and roles) (If applicable): Sarah Cuddy-Walsh (Student Research: Ph.D. Student)  
Study Title: The impact of position dependent sensitivity changes inherent to a new CZT-based dedicated cardiac camera on noise in patient images.  
Funding Source (If applicable):

Effective: **October 12, 2016**

Expires: **October 30, 2017.**

### **Restrictions:**

This certification is subject to the following conditions:

1. Clearance is granted only for the research and purposes described in the application.
2. Any modification to the approved research must be submitted to CUREB-B. All changes must be approved prior to the continuance of the research.
3. An Annual Application for the renewal of ethics clearance must be submitted and cleared by the above date. Failure to submit the Annual Status Report will result in the closure of the file. If funding is associated, funds will be frozen.

4. A closure request must be sent to CUREB-B when the research is complete or terminated.

5. Should any participant suffer adversely from their participation in the project you are required to report the matter to CUREB-B.

6. Failure to conduct the research in accordance with the principles of the *Tri-Council Policy Statement: Ethical Conduct for Research Involving Humans 2nd edition* and the *Carleton University Policies and Procedures for the Ethical Conduct of Research* may result in the suspension or termination of the research project.

Please email the Ethics Coordinators at [ethics@carleton.ca](mailto:ethics@carleton.ca) if you have any questions. If a researcher requires a certificate with a signature, they may contact [ethics@carleton.ca](mailto:ethics@carleton.ca) to have one generated.

**CLEARED BY:**

**Date:**

Andy Adler, PhD, Chair, CUREB-B

**October 12, 2016**

Shelley Brown, PhD, Vice-Chair, CUREB-B

## Ethics protocol

---

**PROTOCOL: The impact of position dependent sensitivity changes inherent to a new CZT-based dedicated cardiac camera on noise in patient images.**

**Version 4.0**

**June 1, 2016**

### Investigators

Principle Investigator: R. Glenn Wells<sup>1</sup>

Co-Investigator: Sarah Walsh<sup>1,2</sup>

<sup>1</sup>Division of Cardiac Imaging, University of Ottawa Heart Institute, Ottawa, ON, Canada

<sup>2</sup>Department of Physics, Carleton University, Ottawa, ON, Canada

### Introduction

Heart disease continues to be a leading cause of death and disability in Canada. Myocardial perfusion imaging (MPI) is a powerful tool for the diagnosis and management of heart disease; it provides valuable information about how much blood is getting to cardiac muscle tissue (myocardium). Single photon emission computed tomography (SPECT) is commonly used for MPI to image the accumulated cardiac distribution of an injected radiopharmaceutical tracer. Some SPECT cameras (GE Discovery NM530c) have been introduced in the last few years that are specially designed to acquire cardiac specific images quickly and with lower doses to the patient than with traditional cameras (such as GE Infinia Hawkeye). To achieve this, these cameras use a limited-angle pinhole design combined with a great number of individual detectors in fixed positions around the patient rather than the traditional approach which was to use two detectors that rotated around the patient during imaging [92].

When imaging the distribution of the radiopharmaceutical tracer, the SPECT camera detects and ‘counts’ the gamma photons emitted through the decay of the isotope attached to the tracer. The number of photons recorded by each detector is governed by Poisson “counting” statistics. This means that the variation of the number of photons counted,  $N$ , is equal to  $N$  (i.e.  $\sigma^2 = N$ ). The noise in this measurement can be thought of as the standard deviation,  $\sigma$ . Image quality depends upon the ratio of the noise contribution ( $\sigma$ ) to the size of the signal,  $N$ , such that the larger  $N$  is, the smaller the effect of noise on the image quality:

$$\frac{\sigma}{N} = \frac{\sqrt{N}}{N} = \frac{1}{\sqrt{N}}, \text{ such that } \uparrow N \rightarrow \uparrow \text{Image Quality}$$

Our GE Discovery NM530c dedicated cardiac SPECT camera employs 19 gamma photon detectors in fixed positions in an arc covering  $\sim 180^\circ$ . The arc extends from the

right-anterior-oblique position to the left-posterior-oblique position. With the detectors stationary and on one side of the patient only, the basal wall of the left ventricle is physically further from the detectors than is the apex. Since photons are attenuated (absorbed and scattered) and the geometric sensitivity (detection efficiency) of the pinholes decreases with distance, fewer photons originating from the base of the heart are expected to be detected (a lower value of N) than from the apex. As such we expect to see a larger noise contribution in the basal region of the heart in an image than the apex.

## **Objective**

Our objective is to evaluate the magnitude of the noise variation within each patient's images in a normal patient population (intra-patient variation) and compare it with the variation between patients' images in a normal database (inter-patient variation) for both the GE Infinia Hawkeye4 (traditional) and the GE Discovery NM530c (CZT) camera designs.

We hypothesize that the noise in images from the GE Discovery NM530c camera will vary spatially but will overall be less than or equal to the noise in images from the GE Infinia Hawkeye camera.

## **Methods**

### Image Acquisition

Images acquired between 01 April 2009 and 30 April 2013 will be retrospectively reanalyzed from patients that underwent rest/stress cardiac perfusion scans with  $^{99m}\text{Tc}$ -tetrofosmin on both the Infinia-Hawkeye4 SPECT/CT (GE Healthcare) and the dedicated cardiac Discovery NM530c SPECT camera (GE Healthcare) using a standard protocol, on the same day. Patient data were collected as part of our approved nuclear cardiology registry (HI-protocol #2004959-01H). Patient consent was obtained for inclusion in the registry database, the details of which are shown in the "Nuclear Cardiology Registry Consent Form" (uploaded in Additional documents). We wish to access this data in order to perform a retrospective analysis.

### Inclusion Criteria

Patients who:

- 1) completed rest/stress Tc-99m-tetrofosmin cardiac perfusion studies on both the Infinia-Hawkeye4 SPECT/CT (GE Healthcare) and the Discovery NM530c SPECT camera (GE Healthcare);
- 2) had studies performed between 01 April 2009 and 30 April 2013;
- 3) had at least 1 CT acquisition included in their study;
- 4) are 18 years of age or older.

### Exclusion Criteria

Patients who:

- 1) are less than 18 years of age;

- 2) have reconstructed images that are of poor quality due to substantial artifacts, incomplete coverage of the heart, or low counting statistics (insufficient data);
- 3) are missing (not acquired) the list file data for their images
- 4) have technically poor quality CT scans due to metal artifacts, incomplete scan coverage, or large patient motion.

### Image Processing and Reconstruction

Once obtained from the database, emission and CT data from the CZT and Infinia SPECT/CT will be paired and de-identified with an alpha-numeric code; a password protected master-list will be maintained on the UOHI server to link the alpha-numeric codes with patient PHI and PII. For each projection data set, CZT camera's list file will be re-binned from 0 to 300s into 300 segments, 1 second each. These will be exported offline where custom in-house software will use a random number generator to select 300 of these segments with replacement to generate a new 300s projection data set; this will be called a "bootstrapped projection data set" [1]. Approximately 400 bootstrapped projection data sets will be generated from each patient study (rest/stress, Infinia Hawkeye4/Discovery NM530c). Bootstrapped projection data sets will be imported back onto the Vendor supplied system for reconstruction.

Vendor supplied software will be used for attenuation correction and image reconstruction of each bootstrapped dataset. The original CT dataset for each patient will be used to create the attenuation map.

### Image Analysis

The previously de-identified images will all be exported offline for analysis. Custom in-house software will perform statistical analysis to produce average images and images of the standard deviation (noise) comparing all 400 bootstrapped images for each patient study (intra-patient statistics). These resulting images will be assigned to 17-segment polar maps of the heart. A paired t-test will be used to compare the standard deviations (intra-patient statistics) for all patient images from one cardiac polar map segment (at the apex) to another segment (at the base).

### Primary Outcome

The primary outcome will be to measure the intra-patient differences in the standard deviation polar map values in the base of the heart compared to at the apex for images acquired with the GE Discovery NM530c SPECT camera and to evaluate the magnitude of the differences relative to the inter-patient standard deviation in a normal database (comparing all normal patient images).

### Secondary Outcome

Comparing the standard deviation polar maps for images acquired with the GE Discovery NM530c SPECT camera to those acquired with the GE Infinia-Hawkeye4 SPECT/CT.

### Sample-Size

It is expected that the mean standard deviation of voxel values in an image will range

from 2%-4% at the apex to 4%-8% at the base of the heart. The apex and basal segments of the heart are assumed to be weakly correlated ( $r=0.25$ ) with standard deviations of 1% and 2% respectively. In order to detect a minimum difference of 1%, with  $\alpha=0.05$  and power=95%, using a two-tailed paired t-test requires a sample size of 54 patients. Attenuation effects and the distribution of uncertainties are different between male and female patients. To obtain adequate statistics for both genders, we will recruit both male and female patients in equal numbers, 54 each for a total of 108 patients. This is in line with other studies in nuclear medicine which use gender-specific normal databases containing 40 individuals each [103].

## **Privacy and Data Security**

We are requesting access to information recorded as part of the Nuclear Cardiology Registry. For reference, we have attached the corresponding Data Request Form.

- MRN, Patient name and study dates are requested to confirm identification of matched image sets.
- A summary of patient demographics will be recorded for the purpose of describing the patient population used in the study. Demographics will be recorded in aggregate form and will include: age, gender, body mass index (BMI), pre-test likelihood, cardiac history and risk factors (previous CABG, previous PTCA/PCI, family history of cardiac disease, current smoker, ex-smoker, hypertension and hyperlipidemia).
- We also request information on the scan (as detailed on the attached Data Request Form): test information, imaging information, stress protocol and final interpretation.
- Only aggregate form of scan data and demographic statistics will be reported/published from this work; individual data will not be reported.

Upon electronic retrieval of the MPI studies from the database, an alpha-numeric code will be assigned and study datasets will be de-identified. A master list linking the alpha-numeric codes to patient personal health information (PHI) and personal identifying information (PII) will be maintained securely (password protected) on the institution UOHI server. This file will be the only possible method to track the data back to the patient MRN. The data analysis computer is password protected and kept in a locked office.

## **Secondary use of data**

The requested access to the nuclear cardiology registry is for secondary use of data: ‘observational studies’ in the “Nuclear Cardiology Registry Consent Form” (uploaded in Additional documents). The following specific conditions are met by this study: the research involves no more than minimal risk to the participants and the research does not involve a therapeutic intervention, or other clinical or diagnostic interventions.

## **Dissemination**

Results from this study will be published in a peer-reviewed nuclear medicine/medical imaging journal.

### **Contact Information**

Principle Investigator:

Dr. R. Glenn Wells  
Division of Cardiac Imaging,  
Room H1233  
University of Ottawa Heart Institute  
40 Ruskin Street  
Ottawa, ON K1Y 4W7

Co-Investigator:

Sarah Walsh, PhD Candidate  
Division of Cardiac Imaging  
Room H2258  
University of Ottawa Heart Institute  
40 Ruskin Street  
Ottawa, ON, K1Y 4W7

## E.2 REB approval for research contributing to Chapter 5

### OHSN-REB Letter of Approval

---



**Ottawa Health Science Network Research Ethics Board/ Conseil d'éthique de la recherche du Réseau de science de la santé d'Ottawa**  
Civic Box 411 725 Paradise Avenue, Ottawa, Ontario K1Y 4P9 (613) 793-5035 ext. 14902 Fax: 613-761-6211  
<http://www.ohsn.ca/ohsn-reb>

October 13, 2017

Dr. Glenn Wells  
Division of Cardiac Imaging,  
University of Ottawa Heart Institute  
40 Ruskin Street H 1233  
Ottawa, ON K1Y 4W7

Dear Dr. Wells:

**Re: Protocol # 20170769-01H The effect of patient body mass on SPECT image noise: A push for using a weight-based dosing protocol.**

**Protocol approval valid until - October 12, 2018**

I am pleased to inform you that this protocol underwent expedited review by the Ottawa Health Science Network Research Ethics Board (OHSN-REB) and is approved. No changes, amendments or additions may be made to the protocol or the consent form without the OHSN-REB's review and approval.

Protocol Version 1.1 dated August 18, 2017 is approved

If the study is to continue beyond the expiry date noted above, a Renewal Form should be submitted to the RFB approximately six weeks prior to the current expiry date. If the study has been completed by this date, a Termination Report should be submitted.

OHSN-REB complies with the membership requirements and operates in compliance with the Tri-Council Policy Statement: Ethical Conduct for Research Involving Humans; the International Conference of Harmonization - Good Clinical Practice, Consolidated Guideline; the provisions of the Personal Health Information Protection Act 2004.

Yours sincerely,

Jim Robitson, M.D.  
Vice Chairperson  
Ottawa Health Science Network Research Ethics Board

JRW/dw

## CUREB-B Letter of Approval

---



Office of Research Ethics  
5110 Human Computer Interaction Bldg |  
1125 Colonel By Drive  
| Ottawa, Ontario K1S 5B6  
613-520-2600 Ext: 4085  
ethics@carleton.ca

### **CERTIFICATION OF INSTITUTIONAL ETHICS CLEARANCE**

This document is an administrative clearance corresponding to approved protocol # **20170769-01H** from the **OHSN** Research Ethics Board. The Carleton University Research Ethics Board-B (CUREB-B) has granted administrative clearance for the research project described below and research may now proceed. CUREB-B is constituted and operates in compliance with the *Tri-Council Policy Statement: Ethical Conduct for Research Involving Humans* (TCPS2).

**Ethics Protocol Clearance ID:** Project # 108948

**Research Team:** **Glenn Wells (Primary Investigator)**

Sarah Cuddy-Walsh (Co-Investigator)

**Project Title:** The effect of patient body mass of SPECT image noise: A push for using a weight-based dosing protocol

**Funding Source** (If applicable):

Effective: **May 11, 2018**

Expires: **May 31, 2019.**

**Restrictions:**

This certification is subject to the following conditions:

1. Clearance is granted only for the research and purposes described in the application.
2. Any modification to the approved research must be submitted to CUREB-B via a Change to Protocol Form. All changes must be cleared prior to the continuance of the research.
3. An Annual Status Report for the renewal of ethics clearance must be submitted and cleared by the renewal date listed above. Failure to submit the Annual Status Report will result in the closure of the file. If funding is associated, funds will be frozen.
4. A closure request must be sent to CUREB-B when the research is complete or terminated.
5. Should any participant suffer adversely from their participation in the project you are required to report the matter to CUREB-B.

Failure to conduct the research in accordance with the principles of the *Tri-Council Policy*

*Statement: Ethical Conduct for Research Involving Humans 2nd edition* and the *Carleton University Policies and Procedures for the Ethical Conduct of Research* may result in the suspension or termination of the research project.

Upon reasonable request, it is the policy of CUREB, for cleared protocols, to release the name of the PI, the title of the project, and the date of clearance and any renewal(s).

Please contact the Research Compliance Coordinators, at [ethics@carleton.ca](mailto:ethics@carleton.ca), if you have any questions or require a clearance certificate with a signature.

**CLEARED BY:**

**Date: May 11, 2018**

Andy Adler, PhD, Chair, CUREB-B

Bernadette Campbell, PhD, Vice-Chair, CUREB-B

## **Ethics protocol**

---

### **PROTOCOL: The effect of patient body mass on SPECT image noise: A push for using a weight-based dosing protocol.**

#### **Version 1.1**

**August 18, 2017**

#### **Investigators**

Principle Investigator: R. Glenn Wells<sup>1</sup>

Co-Investigator: Sarah Walsh<sup>1,2</sup>

<sup>1</sup>Division of Cardiac Imaging, University of Ottawa Heart Institute, Ottawa, ON, Canada

<sup>2</sup>Department of Physics, Carleton University, Ottawa, ON, Canada

#### **Introduction**

Heart disease continues to be a leading cause of death and disability in Canada. Myocardial perfusion imaging (MPI) is a powerful tool for the diagnosis and management of heart disease; it provides valuable information about how much blood is getting to cardiac muscle tissue (myocardium). Single photon emission computed tomography (SPECT) is commonly used for MPI to image the accumulated cardiac distribution of an injected radiopharmaceutical tracer.

Traditional protocols for MPI with SPECT use a fixed administered patient dose. A constant dose leads to lower image quality in heavier patients due to increased photon attenuation. As such, ASNC guidelines state that “an effort to tailor the administered activity to the patient’s habitus and imaging equipment should be made” [93]. The nuclear cardiology division at the University of Ottawa Heart Institute currently administers 300-349 MBq for females with BMI<25 and males with BMI<30. Larger patients receive 350-400 MBq for a full-dose SPECT perfusion myoview study. Even with this adjustment, we observed in another study an approximately 2-fold change in noise between patients. The image noise in the heart of a 100kg patient was 7.2% as compared to noise of 3.4% in a 45kg patient. Furthermore, while we have recently adapted low (half) dose studies as standard, the administered dose is still only adjusted discretely based on the same two categories. We propose using a weight-based or BMI-based adjustment of administered patient dose to minimize noise variation between patients. This will ensure the same image quality and thus normalize the level of care that each patient receives.

We have previously developed a technique to estimate image noise from a single patient acquisition and the corresponding attenuation map. We use this technique to determine a weight/BMI-based dose function which would provide the adjusted dose needed to produce a constant level of image noise.

## Objective

Our objective is to develop a protocol for weight-based dose calculation which could normalize the image quality for all patient studies for both the GE Infinia Hawkeye4 (traditional) and the GE Discovery NM530c (CZT) camera designs.

## Methods

### Image Acquisition

Images acquired between 01 April 2009 and 30 April 2013 will be retrospectively reanalyzed from patients that underwent rest/stress cardiac perfusion scans with <sup>99m</sup>Tc-tetrofosmin on both the Infinia-Hawkeye4 SPECT/CT (GE Healthcare) and the dedicated cardiac Discovery NM530c SPECT camera (GE Healthcare) using a standard protocol, on the same day. Patient data were collected as part of our approved nuclear cardiology registry (HI-protocol #2004959-01H). Patient consent was obtained for inclusion in the registry database, the details of which are shown in the “Nuclear Cardiology Registry Consent Form” (uploaded in Additional documents). We wish to access this data in order to perform a retrospective analysis.

### Inclusion Criteria

Patients who:

- 5) completed rest/stress Tc-99m-tetrofosmin cardiac perfusion studies on both the Infinia-Hawkeye4 SPECT/CT (GE Healthcare) and the Discovery NM530c SPECT camera (GE Healthcare);
- 6) had studies performed between 01 April 2009 and 30 April 2013;
- 7) had at least 1 CT acquisition included in their study;
- 8) are 18 years of age or older.

### Exclusion Criteria

Patients who:

- 5) are less than 18 years of age;
- 6) have reconstructed images that are of poor quality due to substantial artifacts, incomplete coverage of the heart, or low counting statistics (insufficient data);
- 7) have technically poor-quality CT scans due to metal artifacts, incomplete scan coverage, or large patient motion.

### Image Processing and Reconstruction

Once obtained from the database, emission and CT data from the CZT and Infinia SPECT/CT will be paired and de-identified with an alpha-numeric code; a password protected master-list will be maintained on the UOHI server to link the alpha-numeric codes with patient PHI and PII.

Both vendor-supplied and in-house software will be used for attenuation correction and image reconstruction of all projection datasets. The original CT dataset for each patient

will be used to create the attenuation map.

### Image Quality Evaluation

For this study, we will use image noise measured in the heart as a quantitative metric for evaluating image quality. We will evaluate the average image noise for each patient at different simulated administered doses (acquisition durations, T). Two methods for calculating image noise will be used: a projected voxel (PV) method developed in-house and non-parametric bootstrapping technique [1].

**PV method:** For each reconstructed patient image, a map of image noise is estimated directly using that single image and its corresponding attenuation map. This method is based on Poisson counting statistics and provides an estimate of the true noise in the image.

**Bootstrapping method:** For each projection data set, the corresponding list file will be re-binned from 0 to 480s into 480 segments, 1 second each. The CZT camera records data in list file format. For the Infinia-Hawkeye camera, a pseudo-list-file will be generated [104]. Data will be processed offline with custom in-house software which will use a random number generator to select T of these segments with replacement to generate a new T second projection data set; this will be called a “bootstrapped projection data set” [1]. Approximately 400 bootstrapped projection data sets will be generated from each patient study (rest/stress, Infinia Hawkeye4/Discovery NM530c). Since administered dose and camera acquisition time are directly related, the bootstrapped image acquisition duration, T, will be varied to simulate different administered dose levels. Bootstrapped projection data sets will each be reconstructed using standard methods. Offline custom in-house software will perform statistical analysis to produce average images and images of the standard deviation (noise) comparing all 400 bootstrapped images for each patient study (intra-patient statistics).

Since it requires only 1 minute of computation, the PV method will be primarily used to determine the relationship between administered dose (or acquisition time) and patient weight or BMI. The bootstrapping technique (requires ~5 hours per noise estimation) will be used for quality assurance spot checks of the PV method.

The noise values corresponding to all voxels in the myocardium of the left ventricle will be averaged to obtain a single value of image noise for each patient and dose/time level.

### Finding an Administered Dose Formula

We will plot the average image noise as a function of the administered activity dose (D), acquisition duration (T), and patient habitus metric: weight (W) or BMI. The resulting fit will provide us with a formula to determine the required dose to normalize image noise with respect to patient weight/BMI.

### Primary Outcome

The primary outcome will be a single formula which will normalize image noise for all

patients imaged with the GE Discovery NM530c SPECT and GE Infinia Hawkeye4 cameras.

### Secondary Outcome

The secondary outcome will be identifying or excluding a significant difference between formulas for different patient sexes (male/female).

### Analyses of the Results

Image noise will be calculated for de-identified patient images with and without application of the administered dose formula. The resulting mean image noise will be plotted as a function of patient weight (or BMI) to obtain a slope from a linear fit of the data. The 95% confidence interval will be evaluated to determine if it contains a slope of zero to indicate that the patient weight does not significantly affect mean image noise. We will also use a z-test to determine if the slope determined for images acquisitions employing our administered dose formula differs significantly from the slope for the current dose-adjustment method.

### Sample-Size

We are powering our study to detect a change of 20% in the image noise for a weight increase of 50 kg (from 70 to 120 kg), corresponding to a slope in the noise-weight curve of 0.02 /kg. The standard deviation of the residuals from our linear regression is estimated to be 0.91. A sample size of 100 patients is required to obtain a power of 90% for detecting a slope of 0.02 /kg with an  $\alpha=0.05$  [105], assuming the standard deviation in the patient weights is 13.5kg.

Radiotracer uptake and attenuation effects due to body shape are different between male and female patients. Therefore, we will recruit both male and female patients in equal numbers, approximately 50 of each gender for a total of 100 patients. This is in line with other studies in nuclear medicine which use gender-specific normal databases containing 40 individuals each [103].

### **Privacy and Data Security**

We are requesting access to information recorded as part of the Nuclear Cardiology Registry. For reference, we have attached the corresponding Data Request Form.

- MRN, Patient name and study dates are requested to confirm identification of matched image sets.
- A summary of patient demographics will be recorded for the purpose of describing the patient population used in the study. Demographics will be recorded in aggregate form and will include: age, gender, body mass index (BMI), pre-test likelihood, cardiac history and risk factors (previous CABG, previous PTCA/PCI, family history of cardiac disease, current smoker, ex-smoker, hypertension and hyperlipidemia).
- We also request information on the scan (as detailed on the attached Data Request Form): test information, imaging information, stress protocol and final interpretation.
- Only aggregate form of scan data and demographic statistics will be

reported/published from this work; individual data will not be reported.

Upon electronic retrieval of the MPI studies from the database, an alpha-numeric code will be assigned and study datasets will be de-identified. A master list linking the alpha-numeric codes to patient personal health information (PHI) and personal identifying information (PII) will be maintained securely (password protected) on the institution UOHI server. This file will be the only possible method to track the data back to the patient MRN. The data analysis computer is password protected and kept in a locked office.

### **Secondary use of data**

The requested access to the nuclear cardiology registry is for secondary use of data: ‘observational studies’ in the “Nuclear Cardiology Registry Consent Form” (uploaded in Additional documents). The following specific conditions are met by this study: the research involves no more than minimal risk to the participants and the research does not involve a therapeutic intervention, or other clinical or diagnostic interventions.

### **Dissemination**

Results from this study will be published in a peer-reviewed nuclear medicine/medical imaging journal.

### **Contact Information**

#### Principle Investigator:

Dr. R. Glenn Wells  
Division of Cardiac Imaging,  
Room H1233  
University of Ottawa Heart Institute  
40 Ruskin Street  
Ottawa, ON K1Y 4W7

#### Co-Investigator:

Sarah Walsh, PhD Candidate  
Division of Cardiac Imaging  
Room H2258  
University of Ottawa Heart Institute  
40 Ruskin Street  
Ottawa, ON, K1Y 4W7

## References

- [1] I. Buvat, “A non-parametric bootstrap approach for analysing the statistical properties of SPECT and PET images,” *Phys. Med. Biol.*, vol. 47, no. 10, pp. 1761–75, May 2002.
- [2] J. A. White and R. S. Lawson, “A Poisson resampling method for simulating reduced counts in nuclear medicine images,” *Phys. Med. Biol.*, vol. 60, no. 9, pp. N167–N176, 2015.
- [3] Public Health Agency of Canada, “Heart Disease in Canada.”
- [4] *National Health Expenditure Trends, 1975 to 2017*. Ottawa, ON, 2017.
- [5] S. R. Cherry, J. Sorenson, M. E. Phelps, and B. M. Methé, *Physics in Nuclear Medicine*. 2004.
- [6] S. A. Hoedl and W. D. Updegraff, “The Production of Medical Isotopes without Nuclear Reactors or Uranium Enrichment,” *Sci. Glob. Secur.*, vol. 23, no. 2, pp. 121–153, 2015.
- [7] D. L. L. Bailey, J. L. Humm, A. Todd-Pokropek, and A. van Aswegen, Eds., *Nuclear medicine physics: A handbook for teachers and students*. International Atomic Energy Agency, 2014.
- [8] S. Dorbala *et al.*, “Single Photon Emission Computed Tomography (SPECT) Myocardial Perfusion Imaging Guidelines: Instrumentation, Acquisition, Processing, and Interpretation,” *J. Nucl. Cardiol.*, vol. 25, p. 1784, 2018.
- [9] CNSC-CCSN, “Fact Sheet: Natural Background Radiation,” 2013.
- [10] D. Miller and D. Schauer, “The ALARA principle in medical imaging,” *AAPM Newsl.*, vol. 40, no. 1, pp. 38–40, 2015.
- [11] M. N. Wernick and J. N. Aarsvold, *Emission tomography: the fundamentals of PET and SPECT*. Elsevier Academic Press, 2004.
- [12] K. F. Koral, F. M. Swailem, S. Buchbinder, N. H. Clinthorne, W. L. Rogers, and B. M. Tsui, “SPECT dual-energy-window Compton correction: scatter multiplier required for quantification,” *J. Nucl. Med.*, vol. 31, no. 1, pp. 90–98, 1990.
- [13] A. Pourmoghaddas and R. G. Wells, “Analytically based photon scatter modeling for a multipinhole cardiac SPECT camera,” *Med. Phys.*, vol. 43, no. 11, p. 6098, 2016.
- [14] R. G. Wells, K. Soueidan, R. Timmins, and T. D. Ruddy, “Comparison of attenuation, dual-energy-window, and model-based scatter correction of low-count SPECT to <sup>82</sup>Rb PET/CT quantified myocardial perfusion scores,” *J. Nucl. Cardiol.*, vol. 20, no. 5, pp. 785–796, 2013.
- [15] F. J. Beekman, C. Kamphuis, and E. C. Frey, “Scatter compensation methods in 3D iterative SPECT reconstruction: a simulation study,” *Phys. Med. Biol.*, vol. 42,

- no. 8, pp. 1619–1632, 1997.
- [16] R. J. Jaszczak, K. L. Greer, C. E. Floyd, C. Harris, and R. E. Coleman, “Estimating SPECT Count Densities, Scatter Fractions, and Statistical Noise,” *IEEE Trans. Nucl. Sci.*, vol. 32, no. 1, pp. 762–768, 1985.
- [17] K. Ogawa and N. Nishizaki, “Accurate scatter compensation using neural networks in radionuclide imaging,” *IEEE Trans. Nucl. Sci.*, vol. 40, no. 4, pp. 1020–1025, 1993.
- [18] B. F. Hutton, I. Buvat, F. J. Beekman, I. Ene Buvat, and F. J. Beekman, “Review and current status of SPECT scatter correction,” *Phys. Med. Biol. Phys. Med. Biol.*, vol. 56, no. 56, pp. 85–112, 2011.
- [19] L.-T. Chang, “A method for attenuation correction in radionuclide computed tomography,” *IEEE Trans. Nucl. Sci.*, vol. 25, no. 1, pp. 638–643, 1978.
- [20] S. C. Moore, “Attenuation compensation,” in *Computed Emission Tomography*, P. J. Ell and B. L. (Bruce L. Holman, Eds. Oxford University Press, 1982, pp. 339–360.
- [21] D. L. Bailey and K. P. Willowson, “An Evidence-Based Review of Quantitative SPECT Imaging and Potential Clinical Applications,” *J. Nucl. Med.*, vol. 54, no. 1, pp. 83–89, 2013.
- [22] “Infinia Hawkeye 4, Product Datasheet,” 2006.
- [23] E. G. DePuey, “Advances in SPECT camera software and hardware: Currently available and new on the horizon,” *J. Nucl. Cardiol.*, vol. 19, no. 3, pp. 551–581, 2012.
- [24] M. Bocher, I. M. Blevis, L. Tsukerman, Y. Shrem, G. Kovalski, and L. Volokh, “A fast cardiac gamma camera with dynamic SPECT capabilities: Design, system validation and future potential,” *Eur. J. Nucl. Med. Mol. Imaging*, vol. 37, no. 10, pp. 1887–1902, Oct. 2010.
- [25] J. N. Aarsvold, J. R. Galt, J. A. Nye, F. D. Grammens, and Z. A. Glass, “The quality field of view of a discovery 530c,” in *2012 IEEE Nuclear Science Symposium and Medical Imaging Conference Record (NSS/MIC)*, 2012, pp. 3551–3555.
- [26] J. R. Mallard and M. J. Myers, “The Performance of a Gamma Camera for the Visualization of Radioactive Isotopes in vivo,” *Phys. Med. Biol.*, vol. 8, no. 2, pp. 165–182, Jun. 1963.
- [27] H. O. Anger, “Radioisotope cameras,” Berkeley, CA, 1965.
- [28] R. Accorsi and S. D. Metzler, “Analytic determination of the resolution-equivalent effective diameter of a pinhole collimator,” *IEEE Trans. Med. Imaging*, vol. 23, no. 6, pp. 750–763, 2004.
- [29] K. Van Audenhaege, R. Van Holen, S. Vandenberghe, C. Vanhove, S. D. Metzler, and S. C. Moore, “Review of SPECT collimator selection, optimization, and

- fabrication for clinical and preclinical imaging,” *Med. Phys.*, vol. 42, no. 8, pp. 4796–4813, Jul. 2015.
- [30] E. V Garcia, “Physical attributes, limitations, and future potential for PET and SPECT,” *J. Nucl. Cardiol.*, vol. 19 Suppl 1, no. Figure 1, pp. S19-29, Mar. 2012.
- [31] R. G. Wells *et al.*, “Dynamic SPECT Measurement of Absolute Myocardial Blood Flow in a Porcine Model,” *J. Nucl. Med.*, vol. 55, no. 10, pp. 1685–1691, 2014.
- [32] R. G. Wells, B. Marvin, M. Poirier, J. M. Renaud, R. A. DeKemp, and T. D. Ruddy, “Optimization of SPECT Measurement of Myocardial Blood Flow with Corrections for Attenuation, Motion, and Blood-Binding Compared to PET,” *J. Nucl. Med.*, vol. 58, no. 12, pp. 2013–2019, Jun. 2017.
- [33] J. A. Kennedy, O. Israel, and A. Frenkel, “3D iteratively reconstructed spatial resolution map and sensitivity characterization of a dedicated cardiac SPECT camera,” *J. Nucl. Cardiol.*, vol. 21, no. 3, pp. 443–452, 2014.
- [34] B. L. Zaret and G. A. Beller, *Clinical Nuclear Cardiology: State of the art and future directions*, 4th ed. Philadelphia, PA: Mosby/Elsevier, 2005.
- [35] Ramesh Chandra and Arman Rahmim, *Nuclear Medicine Physics: The Basics*, 8th ed. Wolters Kluwer Health, 2017.
- [36] P. J. J. Green, “Bayesian reconstructions from emission tomography data using a modified EM algorithm,” *IEEE Trans. Med. Imaging*, vol. 9, no. 1, pp. 84–93, Mar. 1990.
- [37] G. Germano *et al.*, “Automatic reorientation of three-dimensional, transaxial myocardial perfusion SPECT images,” *J. Nucl. Med.*, vol. 36, no. 6, pp. 1107–1114, 1995.
- [38] R. A. Dvorak, R. K. J. Brown, and J. R. Corbett, “Interpretation of SPECT/CT Myocardial Perfusion Images: Common Artifacts and Quality Control Techniques,” *Radiographics*, vol. 31, no. 7, pp. 2041–2057, Nov. 2011.
- [39] A. K. Paul and H. Nabi, “Gated myocardial perfusion SPECT: basic principles, technical aspects, and clinical applications,” *J. Nucl. Med. Technol.*, vol. 32, no. 4, pp. 179–87, Dec. 2004.
- [40] T. Sharir *et al.*, “Prognostic value of poststress left ventricular volume and ejection fraction by gated myocardial perfusion SPECT in women and men: Gender-related differences in normal limits and outcomes,” *J. Nucl. Cardiol.*, vol. 13, no. 4, pp. 495–506, 2006.
- [41] M. Rubeaux, Y. Xu, G. Germano, D. S. Berman, and P. J. Slomka, “Normal Databases for the Relative Quantification of Myocardial Perfusion,” *Curr. Cardiovasc. Imaging Rep.*, vol. 9, no. 8, p. 22, Aug. 2016.
- [42] M. D. Cerqueira *et al.*, “Standardized myocardial segmentation and nomenclature for tomographic imaging of the heart: A statement for healthcare professionals from the Cardiac Imaging Committee of the Council on Clinical Cardiology of the

- American Heart Association,” *J. Nucl. Cardiol.*, vol. 9, no. 2, pp. 240–245, Jan. 2002.
- [43] F. L. Datz, F. V Gabor, P. E. Christian, G. T. Gullberg, C. E. Menzel, and K. A. Morton, “The use of computer-assisted diagnosis in cardiac perfusion nuclear medicine studies: A review (Part 2),” *J. Digit. Imaging*, vol. 6, no. 1, pp. 1–15, 1993.
- [44] R. A. Dekemp *et al.*, “Multisoftware reproducibility study of stress and rest myocardial blood flow assessed with 3D dynamic PET/CT and a 1-tissue-compartment model of  $^{82}\text{Rb}$  kinetics,” *J. Nucl. Med.*, vol. 54, no. 4, pp. 571–7, Apr. 2013.
- [45] R. Klein *et al.*, “Intra- and inter-operator repeatability of myocardial blood flow and myocardial flow reserve measurements using rubidium-82 pet and a highly automated analysis program,” *J. Nucl. Cardiol.*, vol. 17, no. 4, pp. 600–616, 2010.
- [46] P. Barde and M. Barde, “What to use to express the variability of data: Standard deviation or standard error of mean?,” *Perspect. Clin. Res.*, vol. 3, no. 3, p. 113, Jul. 2012.
- [47] E. P. Ficaro, B. C. Lee, J. N. Kritzman, and J. R. Corbett, “Corridor4DM: The Michigan method for quantitative nuclear cardiology,” *J. Nucl. Cardiol.*, vol. 14, no. 4, pp. 455–465, Jul. 2007.
- [48] R. Hachamovitch and D. S. Berman, “The use of nuclear cardiology in clinical decision making,” *Semin. Nucl. Med.*, vol. 35, no. 1, pp. 62–72, 2005.
- [49] A. L. Kesner, G. Abourbeh, E. Mishani, R. Chisin, S. Tshori, and N. Freedman, “Gating, enhanced gating, and beyond: Information utilization strategies for motion management, applied to preclinical PET,” *EJNMMI Res.*, vol. 3, no. 1, pp. 1–15, 2013.
- [50] J. A. Kennedy and H. William Strauss, “Motion detection and amelioration in a dedicated cardiac solid-state CZT SPECT device,” *Med. Biol. Eng. Comput.*, pp. 1–9, 2016.
- [51] X. Niu, Y. Yang, M. Jin, M. N. Wernick, and M. a King, “Effects of motion, attenuation, and scatter corrections on gated cardiac SPECT reconstruction,” *Med. Phys.*, vol. 38, no. 12, pp. 6571–84, 2011.
- [52] A. Pourmoghaddas, R. Klein, R. a DeKemp, and R. G. Wells, “Respiratory phase alignment improves blood-flow quantification in  $\text{Rb}^{82}$  PET myocardial perfusion imaging,” *Med. Phys.*, vol. 40, no. 2, p. 022503, 2013.
- [53] P. J. Slomka, J. A. Patton, D. S. Berman, and G. Germano, “Advances in technical aspects of myocardial perfusion SPECT imaging,” *J. Nucl. Cardiol.*, vol. 16, no. 2, pp. 255–276, 2009.
- [54] N. B. Smith and A. Webb, *Introduction to Medical Imaging : Physics, Engineering and Clinical Applications*. Cambridge University Press, 2010.

- [55] R. J. Jaszczyk, J. Li, H. Wang, M. R. Zalutsky, and R. E. Coleman, “Pinhole collimation for ultra-high-resolution, small-field-of-view SPECT,” *Phys. Med. Biol.*, vol. 39, pp. 4–37, 1994.
- [56] P. H. Pretorius and M. A. King, “Diminishing the impact of the partial volume effect in cardiac SPECT perfusion imaging,” *Med. Phys.*, vol. 36, no. 1, pp. 105–115, 2009.
- [57] N. Kawel *et al.*, “Normal left ventricular myocardial thickness for middle-aged and older subjects with steady-state free precession cardiac magnetic resonance: the multi-ethnic study of atherosclerosis,” *Circ. Cardiovasc. Imaging*, vol. 5, no. 4, pp. 500–8, Jul. 2012.
- [58] V. Bettinardi, I. Castiglioni, E. De Bernardi, and M. C. Gilardi, “PET quantification: Strategies for partial volume correction,” *Clin. Transl. Imaging*, vol. 2, no. 3, pp. 199–218, 2014.
- [59] S. Orlov, “Theory of three dimensional reconstruction - 1. Conditions for a complete set of Projections,” *Sov. Phys. Crystallogr.*, vol. 20, no. 3, pp. 312–314, 1975.
- [60] S. D. D. Metzler, J. E. E. Bowsher, and R. J. J. Jaszczyk, “Geometrical similarities of the Orlov and Tuy sampling criteria and a numerical algorithm for assessing sampling completeness,” *IEEE Trans. Nucl. Sci.*, vol. 50, no. 5, pp. 1550–1555, Oct. 2003.
- [61] H. K. Tuy, “An Inversion Formula for Cone-Beam Reconstruction,” *Source SIAM J. Appl. Math.*, vol. 43, no. 3, pp. 546–552, 1983.
- [62] H. H. Barrett, D. W. Wilson, and B. M. Tsui, “Noise properties of the EM algorithm: I. Theory,” *Phys. Med. Biol.*, vol. 39, no. 5, pp. 833–846, 1994.
- [63] A. Rahmim and J. Tang, “Noise propagation in resolution modeled PET imaging and its impact on detectability,” *Phys. Med. Biol.*, vol. 58, no. 19, pp. 6945–6968, 2013.
- [64] D. W. Wilson, B. M. W. Tsui, and H. H. Barrett, “Noise properties of the EM algorithm. II. Monte Carlo simulations,” *Phys. Med. Biol.*, vol. 39, no. 5, pp. 847–871, 1994.
- [65] “Quantitative Nuclear Medicine Imaging: Concepts, Requirements and Methods,” *IAEA Hum. Heal. Reports*, vol. 9, p. 59, 2014.
- [66] S. G. Cuddy-Walsh and R. G. Wells, “Patient-specific estimation of spatially variant image noise for a pinhole cardiac SPECT camera,” *Med. Phys.*, vol. 45, no. 5, pp. 2033–2047, Apr. 2018.
- [67] R. A. DeKemp, R. G. Wells, and R. S. Beanlands, “Women Image Wisely the 3 mSv Challenge for Nuclear Cardiology,” *JACC Cardiovasc. Imaging*, vol. 9, no. 4, pp. 385–387, 2016.
- [68] W. W. Mayo-Smith and R. L. Morin, “Image Wisely: The Beginning, Current

- Status, and Future Opportunities,” *J. Am. Coll. Radiol.*, vol. 14, no. 3, pp. 442–443, 2017.
- [69] J. D. van Dijk *et al.*, “Minimizing patient-specific tracer dose in myocardial perfusion imaging using CZT SPECT,” *J. Nucl. Med. Technol.*, vol. 43, no. 1, pp. 36–40, Mar. 2015.
- [70] J. D. van Dijk *et al.*, “Development and validation of a patient-tailored dose regime in myocardial perfusion imaging using CZT-SPECT,” *J. Nucl. Cardiol.*, vol. 21, no. 6, pp. 1158–1167, 2014.
- [71] J. D. van Dijk, P. L. Jager, J. P. Ottervanger, C. H. Slump, S. Knollema, and J. A. van Dalen, “Patient-specific tracer activity in MPI SPECT: A hands-on approach,” *J. Nucl. Cardiol.*, vol. 23, no. 1, pp. 145–8, Feb. 2016.
- [72] J. D. van Dijk *et al.*, “Development and validation of a patient-tailored dose regime in myocardial perfusion imaging using conventional SPECT,” *J. Nucl. Cardiol.*, vol. 23, no. 1, pp. 134–42, Feb. 2016.
- [73] J. Oddstig *et al.*, “The radiation dose to overweighted patients undergoing myocardial perfusion SPECT can be significantly reduced: validation of a linear weight-adjusted activity administration protocol,” *J. Nucl. Cardiol.*, vol. 24, no. 6, pp. 1912–1921, Dec. 2017.
- [74] J. Oddstig, F. Hedeer, J. Jögi, M. Carlsson, C. Hindorf, and H. Engblom, “Reduced administered activity, reduced acquisition time, and preserved image quality for the new CZT camera,” *J. Nucl. Cardiol.*, vol. 20, no. 1, pp. 38–44, Feb. 2013.
- [75] M. K. O’Connor, E. Bothun, and R. J. Gibbons, “Influence of patient height and weight and type of stress on myocardial count density during SPECT imaging with thallium-201 and technetium 99m-sestamibi,” *J. Nucl. Cardiol.*, vol. 5, no. 3, pp. 304–312, Jun. 1998.
- [76] J. Qi, “A unified noise analysis for iterative image estimation,” *Phys. Med. Biol.*, vol. 48, no. 21, pp. 3505–3519, Nov. 2003.
- [77] W. Wang and G. Gindi, “Noise analysis of MAP-EM algorithms for emission tomography,” *Phys. Med. Biol.*, vol. 42, no. 11, pp. 2215–2232, 1997.
- [78] S. D. Metzler, K. L. Greer, and R. J. Jaszczak, “Helical pinhole spect for small-animal imaging: a method for addressing sampling completeness,” *IEEE Trans. Nucl. Sci.*, vol. 50, no. 5, pp. 1575–1583, Oct. 2003.
- [79] F. Noo and R. Clackdoyle, “Sampling strategies and resolution in limited data cone-beam tomography,” *Acoust. Speech, Signal Process. 2001 (ICASSP 2001)*, vol. 3, pp. 2025–2028, 2001.
- [80] R. Clackdoyle and F. Noo, “Cone-beam tomography from limited vertex sets: theory and an algorithm,” *Proc. 2001 Int. Conf. Sampl. Theory Appl. (SAMPTA 2001)*, pp. 205–212, 2001.
- [81] R. Clackdoyle and F. Noo, “Cone-beam tomography from 12 pinhole vertices,” in

- 2001 *IEEE Nuclear Science Symposium Conference Record*, 2001, vol. 4, pp. 1874–1876.
- [82] G. L. Zeng and G. T. Gullberg, “SPECT region of interest reconstruction with truncated transmission and emission data,” *Med. Phys.*, vol. 37, no. 9, p. 4627, 2010.
- [83] L. Imbert *et al.*, “Compared performance of high-sensitivity cameras dedicated to myocardial perfusion SPECT: A comprehensive analysis of phantom and human images,” *J. Nucl. Med.*, vol. 53, no. 12, pp. 1897–1903, Dec. 2012.
- [84] F. P. Esteves *et al.*, “Novel solid-state-detector dedicated cardiac camera for fast myocardial perfusion imaging: multicenter comparison with standard dual detector cameras,” *J. Nucl. Cardiol.*, vol. 16, no. 6, pp. 927–34, 2009.
- [85] R. Timmins, T. D. Ruddy, and R. G. Wells, “Patient position alters attenuation effects in multipinhole cardiac SPECT,” *Med. Phys.*, vol. 42, no. 3, p. 1233, 2015.
- [86] S. C. Liew, B. H. Hasegawa, J. K. Brown, and T. F. Lang, “Noise propagation in SPECT images reconstructed using an iterative maximum-likelihood algorithm,” *Phys. Med. Biol.*, vol. 38, no. 12, pp. 1713–1726, Dec. 1993.
- [87] A. Pourmoghaddas and R. G. Wells, “Quantitatively accurate activity measurements with a dedicated cardiac SPECT camera: Physical phantom experiments,” *Med. Phys.*, vol. 43, no. 1, pp. 44–51, 2016.
- [88] H. Jacobowitz and S. D. Metzler, “Geometric Sensitivity of a Pinhole Collimator,” *Int. J. Math. Math. Sci.*, p. 18, 2010.
- [89] B. A. Herzog *et al.*, “Validation of CT Attenuation Correction for High-Speed Myocardial Perfusion Imaging Using a Novel Cadmium- Zinc-Telluride Detector Technique,” *J. Nucl. Med.*, vol. 51, no. 10, pp. 1539–1544, 2010.
- [90] A. Pourmoghaddas, K. Vanderwerf, T. D. Ruddy, R. Glenn Wells, and R. G. Wells, “Scatter correction improves concordance in SPECT MPI with a dedicated cardiac SPECT solid-state camera,” *J. Nucl. Cardiol.*, vol. 22, no. 2, pp. 334–343, 2015.
- [91] D. H. D. West, “Updating Mean and Variance Estimates: An Improved Method,” *Commun. ACM*, vol. 22, no. 9, pp. 532–535, 1979.
- [92] E. V Garcia, T. L. Faber, and F. P. Esteves, “Cardiac dedicated ultrafast SPECT cameras: New designs and clinical implications,” *J. Nucl. Med.*, vol. 52, no. 2, pp. 210–7, Mar. 2011.
- [93] M. J. Henzlova, W. L. Duvall, A. J. Einstein, M. I. Travin, and H. J. Verberne, “ASNC imaging guidelines for SPECT nuclear cardiology procedures: Stress, protocols, and tracers,” *J. Nucl. Cardiol.*, vol. 23, no. 3, pp. 606–639, Jun. 2016.
- [94] J. D. van Dijk, P. L. Jager, J. P. Ottawavanger, C. H. Slump, S. Knollema, and J. A. van Dalen, “Patient-specific activity or scan-time in SPECT myocardial perfusion imaging: A hands-on approach,” *J. Nucl. Cardiol.*, vol. 23, no. 1, pp.

145–148, 2015.

- [95] A. Notghi, N. Williams, N. Smith, S. Goyle, and L. K. Harding, “Relationship between myocardial counts and patient weight: adjusting the injected activity in myocardial perfusion scans,” *Nucl. Med. Commun.*, vol. 24, no. 1, pp. 55–59, Jan. 2003.
- [96] A. Juan Ramon *et al.*, “Investigation of dose reduction in cardiac perfusion SPECT via optimization and choice of the image reconstruction strategy,” *Journal of Nuclear Cardiology*, pp. 1–12, 2017.
- [97] T. Spyridonidis, T. Skouras, and D. J. Apostolopoulos, “Adherence of Tc-99m agents to plastic syringes,” *J. Nucl. Cardiol.*, vol. 23, no. 6, pp. 1526–1526, Dec. 2016.
- [98] H. Abdi, “The Bonferonni and Šidák Corrections for Multiple Comparisons,” in *Encyclopedia of measurement and statistics*, Neil Salkind, Ed. Thousand Oaks, 2007.
- [99] G. B. Grossman *et al.*, “Quantitative Tc-99m sestamibi attenuation-corrected SPECT: Development and multicenter trial validation of myocardial perfusion stress gender-independent normal database in an obese population,” *J. Nucl. Cardiol.*, vol. 11, no. 3, pp. 263–272, May 2004.
- [100] C. Hindorf, J. Oddstig, F. Hedeer, M. J. Hansson, J. Jögi, and H. Engblom, “Importance of correct patient positioning in myocardial perfusion SPECT when using a CZT camera,” *J. Nucl. Cardiol.*, vol. 21, no. 4, pp. 695–702, Aug. 2014.
- [101] A. Gimelli, M. Bottai, A. Quaranta, A. Giorgetti, D. Genovesi, and P. Marzullo, “Gender differences in the evaluation of coronary artery disease with a cadmium-zinc telluride camera,” *Eur. J. Nucl. Med. Mol. Imaging*, vol. 40, pp. 1542–1548, 2013.
- [102] M. Fiechter *et al.*, “Cadmium-zinc-telluride myocardial perfusion imaging in obese patients,” *J. Nucl. Med.*, vol. 53, no. 9, pp. 1401–6, Sep. 2012.
- [103] P. J. Slomka *et al.*, “Automated quantification of myocardial perfusion SPECT using simplified normal limits,” *J. Nucl. Cardiol.*, vol. 12, no. 1, pp. 66–77, Feb. 2005.
- [104] M. Dahlbom, “Estimation of image noise in PET using the bootstrap method,” *IEEE Trans. Nucl. Sci.*, vol. 49, no. 5, pp. 2062–2066, 2002.
- [105] F. Faul, E. Erdfelder, A. Buchner, and A.-G. Lang, “Statistical power analyses using G\*Power 3.1: Tests for correlation and regression analyses,” *Behav. Res. Methods*, vol. 41, no. 4, pp. 1149–1160, Nov. 2009.